University of California
Santa Barbara

Calibration Systems of the KATRIN Experiment and Systematics Inherent in the Search for Sterile Neutrinos at the keV Scale

A dissertation submitted in partial satisfaction
of the requirements for the degree

Doctor of Philosophy
in
Physics

by

Matthew A Bahr

Committee in charge:

Professor Benjamin Monreal, Chair
Professor Harry Nelson
Professor David Berenstein

September 2015

The Dissertation of Matthew A Bahr is approved.

Professor Harry Nelson

Professor David Berenstein

Professor Benjamin Monreal, Committee Chair

September 2015

Calibration Systems of the KATRIN Experiment and Systematics Inherent in the Search for Sterile Neutrinos at the keV Scale

by

Matthew A Bahr

Curriculum Vitæ

Matthew A Bahr

Education

Bachelor of Arts, Physics, University of California, Berkeley, May 2008

Doctor of Philosophy, Physics, University of California, Santa Barbara, September 2015 (expected)

Professional Employment

May, 2008 - December, 2008: Laboratory Technician, Department of Nuclear Engineering, University of California, Berkeley

August, 2009 - December, 2009: Teaching Assistant, Department of Physics, University of California, Santa Barbara

January 2010 - September, 2015: Research Assistant, Department of Physics, University of California, Santa Barbara

Publications

"Project8: Precision Electron Specroscopy to Measure the Mass of the Neutrino," Project 8 Collaboration (P.J. Doe et al.). Sept. 2013. arXiv:1309.7093

"Monitoring of the operating parameters of the KATRIN Windowless Gaseous Tritium Source," M. Babutzka, M. Bahr, J. Bonn, B. Bornschein, A. Dieter, G. Drexlin, K. Eitel, S. Fischer et al.. *New Journal of Physics*, 14(10):103046, October 2012

Fields

Major Field: Experimental Particle Physics

Experimental research into measuring the neutrino mass with Professor Benjamin Monreal and the KATRIN collaboration

Abstract

Calibration Systems of the KATRIN Experiment and Systematics Inherent in the Search for Sterile Neutrinos at the keV Scale

by

Matthew A Bahr

The presence of non-zero neutrino mass is one of the most important discoveries of physics beyond the standard model. Experiments in neutrino oscillation have established the mass splittings and mixing parameters of the (as of now) three known mass states, but the absolute scale of neutrino masses remains a mystery. In addition, evidence has mounted suggesting that the current picture of the three neutrino species may not be complete.

The KATRIN (Karlsruhe Tritium Neutrino) experiment aims to measure the neutrino mass to 0.2 eV, representing an order of magnitude improvement in any direct measurement of the absolute scale. KATRIN will accomplish this task by measuring the endpoint spectrum of beta decay electrons from molecular tritium. The high precision beta spectroscopy will be performed via magnetic collimation electrostatic (MAC-E) filter spectroscopy. This measurement technique presents several sources of systematic error. In particular, it is of utmost importance that the activity and column density is of tritium is known to high precision. The presence of backscattered electrons also have the potential to alter the shape of the tritium endpoint. This document contains discussion of these systematic uncertainties, along with the design and construction of calibration systems that aim to reduce those systematics.

The question of electron backscattering, and how it applies to the KATRIN mea-

surement has also been explored experimentally for the first time. A measurement has been performed using a scanning electron microscope and custom-designed electrostatic spectrometer to measure the energy spectrum of backscattered electrons close to the tritium endpoint energy. An analysis has also been performed to explore the possible systematics originating from backscattered electrons on a possible keV-scale sterile neutrino search.

The electron backscattering experiment has measured Auger electrons from gold in the energy range 6-11 keV produced at a rate of 10^{-4} Auger electrons per incident electron. An investigation of proposed keV sterile neutrino search analysis methods show that this rate of Auger electron production is problematic, and work needs to be done to reduce this source of background if a keV-scale sterile neutrino search is to be successful.

Contents

List of Figures

Chapter 1

The Modern Theory of Neutrinos

The existence of the neutrino was first postulated in an effort to preserve momentum conservation in observed weak decays. As an example, the electron kinetic energy spectrum (seen in figure 1.1) resulting from tritium beta decay indicates that there is an additional unseen decay product. Without the neutrino, momentum conservation would dictate the observation of a mono-energetic electron source, which is obviously not the case.

The neutrino is electrically neutral, with no discernible charge distribution, and thusly only interacts weakly and (as assumed) gravitationally. The neutrino, as originally postulated, was assumed massless, but we now know that is not the case. Knowledge of the neutrino's mass is very important and vital to our future understanding of particle physics and cosmology.

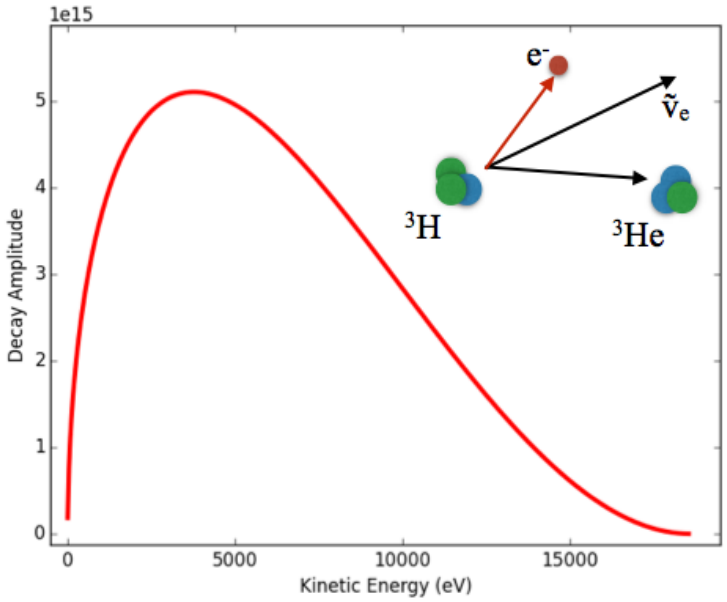

Figure 1.1: The electron kinetic energy spectrum from tritium beta decay. The continuous spectrum confirms the existence of an additional unseen decay product.

1.1 Oscillations

First observed in the 1960s in experiments observing solar neutrinos, neutrino oscillation is one of the first effects identified that is not explained through the standard model. Furthermore, the effect confirms that the neutrino must have non-zero mass. The phenomenon of neutrino oscillation is observed when neutrinos are created in some flavor state, and after propagation through free space, are observed as a neutrino of another flavor. The explanation for neutrino oscillations supposes that the flavor eigenstates (corresponding to electron, muon, and tau) are mixtures of distinct mass eigenstates. Mathematically:

$$\mid \nu_l \rangle = \sum_j U_{lj}^* \mid \nu_j \rangle, \qquad l = e, \mu, \tau \tag{1.1}$$

Where U_{lj} is a unitary matrix and can be parametrised,

$$U_{lj} = \begin{pmatrix} 1 & & \\ & c_{23} & s_{23} \\ & -s_{23} & c_{23} \end{pmatrix} \begin{pmatrix} c_{13} & & s_{13}e^{-i\delta} \\ & 1 & \\ -s_{13}e^{i\delta} & & c_{13} \end{pmatrix} \begin{pmatrix} c_{12} & s_{12} & \\ -s_{12} & c_{12} & \\ & & 1 \end{pmatrix} \begin{pmatrix} e^{i\alpha_1/2} & & \\ & e^{i\alpha_2/2} & \\ & & 1 \end{pmatrix} \tag{1.2}$$

Here, s_{ij} and c_{ij} denote $\sin\theta_{ij}$ and $\cos\theta_{ij}$, where θ_{ij} is the relevant mixing angle. The phases, δ, μ_1, and μ_2 are called the *CP violating phases*, because they give rise to CP violating effects in neutrino mixing. The phase, δ is called the *Dirac* phase, while the other two are the *Majorana* phases, and cannot be measured through neutrino oscillation observations. The Majorana phases are only nonzero in the case that the neutrino is a Majorana particle (more on Majorana neutrinos is included below).

Interference between the different mass states as neutrinos propagate through space has an oscillatory effect, causing neutrinos produced as one flavor to behave as another with time-dependent probability. For the simplified two-flavor model, the probability of flavor switching can be shown to be:

$$P(\nu_e \to \nu_\mu) = \sin^2 2\theta \sin^2\left(\frac{L\Delta m^2}{4E_\nu}\right) \tag{1.3}$$

Neutrino oscillation experiments are thusly sensitive to the difference in mass squared of the different neutrino species, but not the absolute values of the neutrino mass. The best we can hope for is a lower limit on one or more (or, equivalently, the sum of all) neutrino species. Current best fit values on neutrino mass parameters, compiled from all types of experiments, are shown below. Results are compiled and

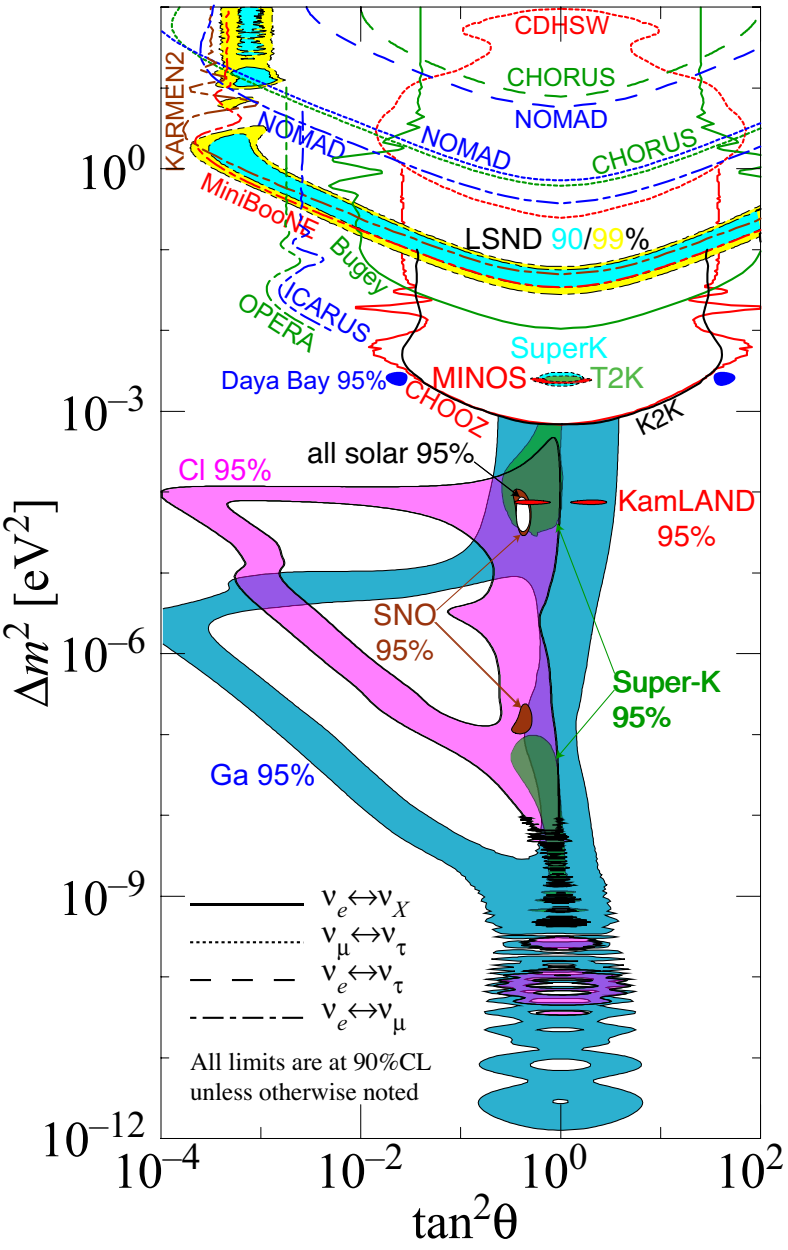

Figure 1.2: The favored and excluded parameter spaces from several oscillation experiments. Tremendous agreement is found in regions corresponding to the atmospheric and solar mixing regions. Of particular note is the LSND anomalous result at $0.1 - 1\ eV^2$. Figure from the *Review of Particle Physics*[1].

conveniently displayed in the *Review of Particle Physics*[1].

$$\begin{aligned}
\Delta m^2_{21} &= 7.54^{+0.26}_{-0.22} \times 10^{-5} eV^2 \\
\mid \Delta m^2_{31} \mid \approx \mid \Delta m^2_{32} \mid &= 2.43^{+0.06}_{-0.10} \times 10^{-3} eV^2 \\
\sin^2\theta_{12} &= 0.307^{+.018}_{-.016} \\
\sin^2\theta_{23} &= 0.386^{+.024}_{-.021} \\
\sin^2\theta_{13} &= 0.0241 \pm 0.0025 \\
\delta/\pi &= 1.39^{+0.38}_{-0.27}\ (2\sigma)
\end{aligned} \tag{1.4}$$

The results shown above are derived from several experiments using a variety of neutrino sources. Uncertainties indicate 1σ bounds except where indicated. The smaller mass splitting, Δm^2_{12}, sometimes called the *solar* mass splitting, is derived from experiments in neutrino oscillations of solar neutrinos (first observed in radiochemical experiments like the Homestake experiment[9], and more recently in the SNO experiment[10, 11]) as well as nuclear reactor experiments like KamLAND[12].

The Δm^2_{23} mass splitting term is sometimes called the *atmospheric* mass splitting, due to its observation in atmospheric neutrinos (produced by collisions with high energy cosmic rays) in experiments like Super-Kamiokande[13, 14]. Further confirmation of this mass splitting is found in accelerator experiments like K2K[15], T2K[16] and MINOS[17], which produce neutrinos by aiming high energy particles into a high-density target. Most recently, the θ_{13} mixing angle has been observed in reactor experiments Double Chooz[18], Daya Bay[19], and RENO[20].

It is of note that the sign of Δm^2_{12} has been established from oscillation effects from propagation through matter, while that of Δm^2_{23} is still a mystery. The sign of that

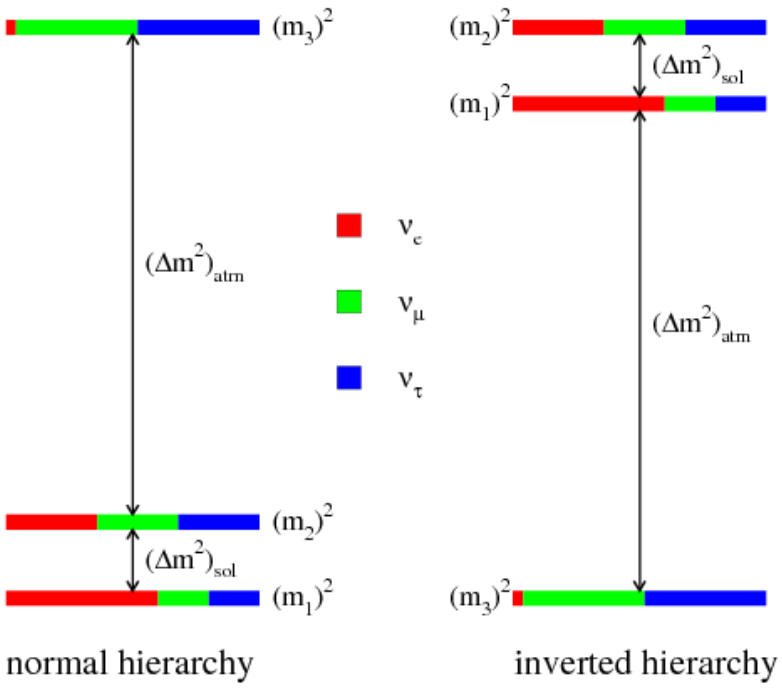

Figure 1.3: The normal and inverted mass hierarchies. Figure from *Hewett, et al.*[2]

mass splitting determines the *hierarchy* of neutrino masses, as shown in figure 1.3. This ambiguity concerning the hierarchy of neutrino masses has implications in our understanding going forward.

Of note is the fact that these mass splittings are smaller than the target sensitivity of Katrin. Thus, a non-zero value for the neutrino mass, as measured by Katrin, would show that the three neutrino species have nearly-degenerate masses.

1.1.1 Sterile Neutrinos

An increasing number of anomalous results have brought into question the completeness of our understanding of neutrinos and neutrino oscillations. In particular, these results have supported the possibility of additional neutrino species that we re-

fer to as "sterile," indicating that they do not interact via the weak force, and yet can still be observed through oscillation effects. There are two different types of sterile neutrinos that are being investigated. The first is an eV-scale neutrino that is suggested from the results of several oscillation experiments. The second is a keV-scale neutrino that has astronomical and cosmological implications.

Sterile neutrinos in the eV scale have been hypothesized as an explanation for results in oscillation experiments. These results include the consistent lower-than-expected neutrino flux seen in various reactor neutrino experiments, and the famous LSND accelerator result. One or two sterile neutrinos is enough to bring these results in line with the rest of our understanding of neutrino oscillations.

Unidentified 3.5 keV lines in regions of dark matter concentration have given rise to the possibility of additional sterile neutrinos, this time of mass around 7 keV. Sterile neutrinos are thusly among the forefront of possible dark matter candidates, and confirmation of a sterile neutrino in this mass range would have exciting implications in the fields of cosmology and astrophysics.

Sterile neutrinos at the eV scale

Several oscillation experiments have suggested the existence of sterile neutrinos. These results have followed from the short-baseline experiments summarized here:

- The LSND short-baseline accelerator experiment has observed a $\overline{\nu_\mu}$ disappearance signal that is incompatible with later long-baseline experiments[21]. Another short-baseline experiment, MiniBooNE, was built to confirm this outcome, and has shown mostly consistent results[22].

- The reactor neutrino anomaly is the observation of smaller-than-expected $\overline{\nu_e}$

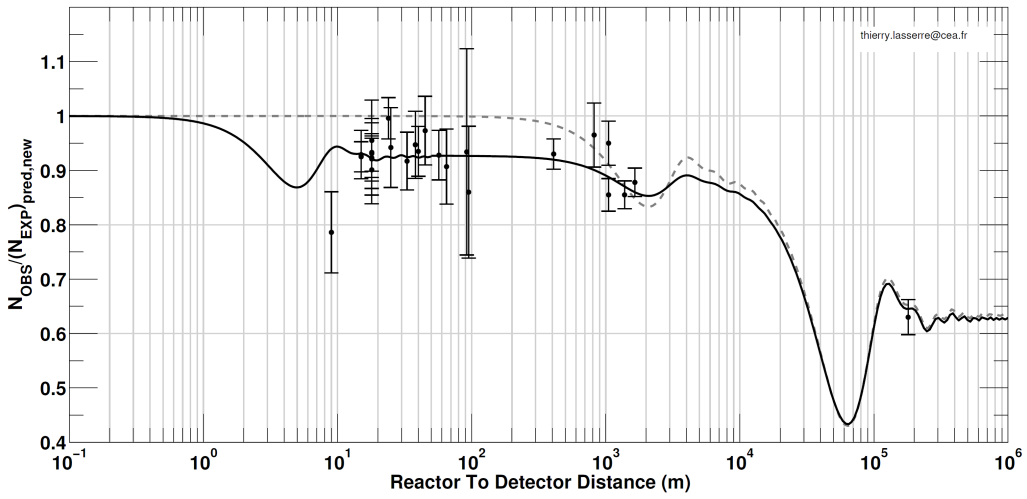

Figure 1.4: Neutrino detection rates from several short-baseline reactor neutrino experiments. The dotted line indicates the expected results based on reactor models and the basic three neutrino mixing parameters. The solid line indicates the one sterile neutrino best fit. Figure from *Gando, et al* [3].

rate near the vicinity of nuclear reactors[23, 24, 25].

- The gallium neutrino anomaly is the disappearance of ν_e that is observed in short-baseline calibration runs of the solar neutrino experiments GALLEX[26] and SAGE[27, 28].

Statistical analysis of all of these results have indicated that these results can all simultaneously be reconciled by the addition of one or two new mass states[29, 30, 31, 32]. The KATRIN experiment will be able to probe a portion of the possible parameter space of these proposed mass states, though will not reach the best fit region of $\sim 1eV$ at 90% confidence level[4].

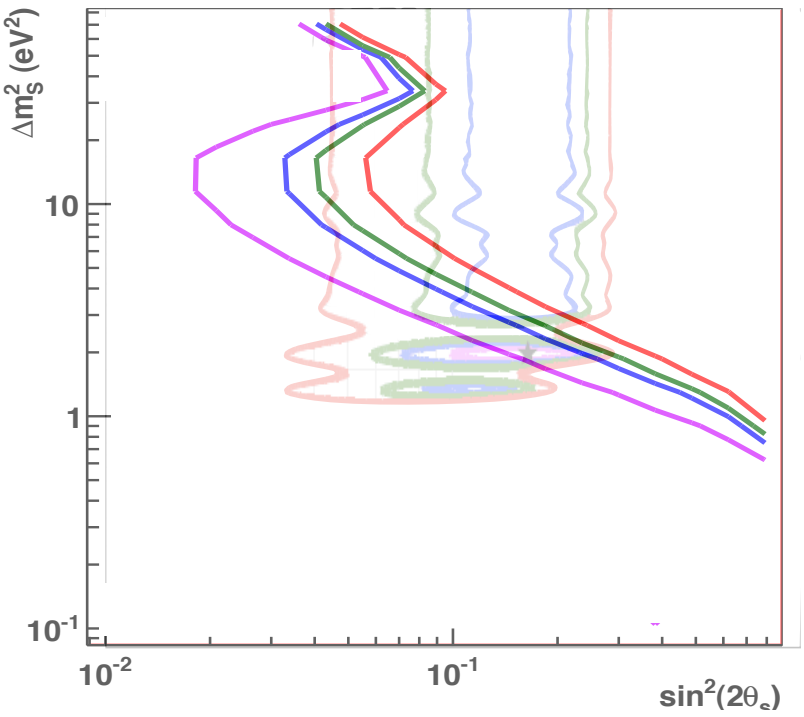

Figure 1.5: The KATRIN sensitivity space to sterile neutrinos, on top of the best fit parameters from oscillation experiments. The contours indicate confidence levels of 68%, 90%, 95%, and 99%. Figure from Barrett and Formaggio[4].

Sterile neutrinos at the keV-scale

Measurements of X-ray spectra in the center of galaxy clusters have recently found an unidentified line at the energy of about 3.5 keV[33]. One exciting possibility is that this line is the result of $\sim$ 7 keV sterile neutrino decay. A sterile neutrino is this energy range has emerged as a new dark matter candidate, and calculations have shown that it can explain the entirety of the observed dark matter[34, 35].

Plans are underway to use the KATRIN tritium source to probe the existence of a neutrino mass state in this energy range. This measurement, however, cannot be done concurrently with the endpoint measurement, so planning has started to modify the experiment and perform this new measurement following KATRIN's conclusion. Initial statistical analysis has shown that, due to the high rate of the KATRIN tritium source, such an experiment could find evidence for a keV-scale sterile neutrino with mixing angle as low as $\sin^2\theta \sim 10^{-7}$[36, 37]. The systematics involved in this sort of measurement are still under investigation, with some aspects presented later in this work.

1.2 Neutrinoless Double Beta Decay

Most of our treatment of neutrinos supposes that the neutrino is distinct from its antiparticle. Because the neutrino is a neutral particle, it is possible that neutrinos and antineutrinos are the same particle- in other words, that the neutrino is a *Majorana* particle. If such an assumption were true, $0\nu\beta\beta$ would be an allowed decay process for several nuclear isotopes. Figure 1.6 illustrates the $0\nu\beta\beta$ process.

If the neutrino is Majorana, $0\nu\beta\beta$ decay also serves as a measure of the neutrino mass. The decay rate depends on the neutrino mass because of the helicity flip that

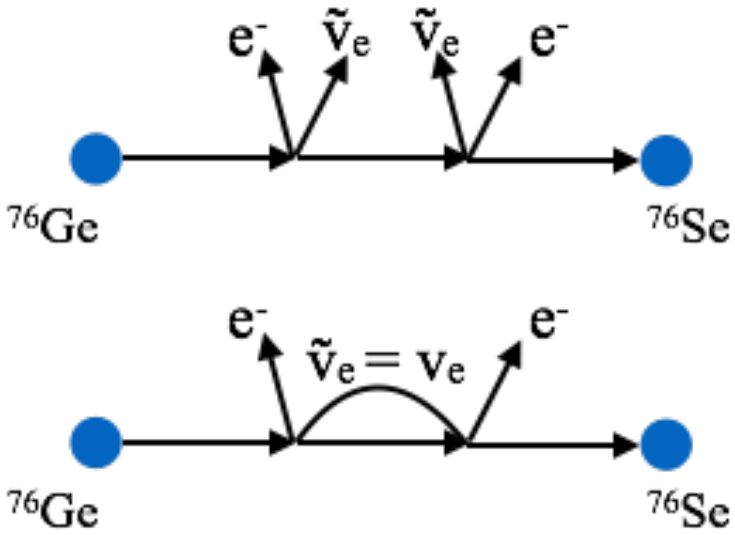

Figure 1.6: Illustration of the $2\nu\beta\beta$ and $0\nu\beta\beta$ decays. In the neutrinoless case, the first antineutrino is absorbed as a neutrino, which is only allowed if the neutrino is a Majorana particle.

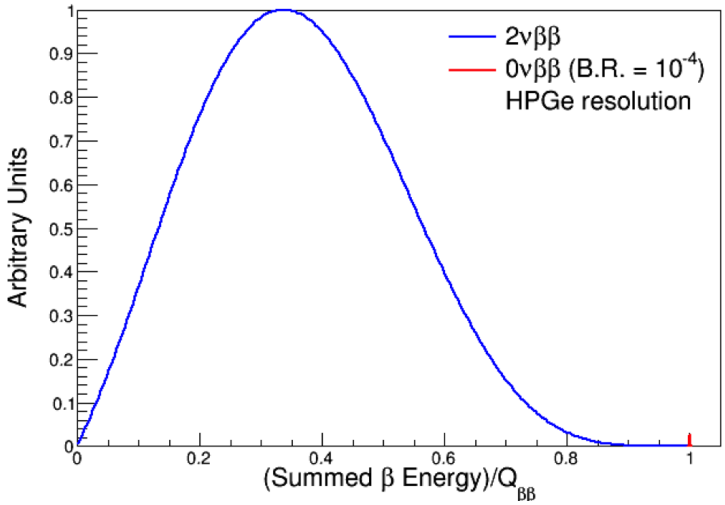

Figure 1.7: A hypothetical spectrum with a $0\nu\beta\beta$ signal, showing the summed energies of the two beta electrons. The $2\nu\beta\beta$ decay yields a continuous spectrum, with the electrons sharing energy with the two emitted neutrinos. The $0\nu\beta\beta$ signal is a monoenergetic source at the maximum sum energy. Figure courtesy the Majorana collaboration

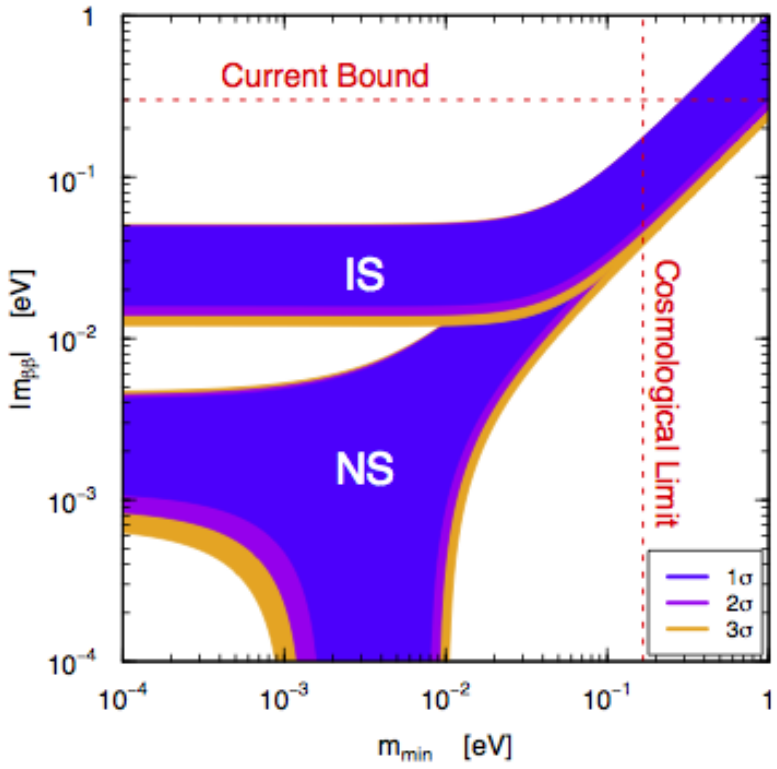

Figure 1.8: The Majorana effective mass, as a function of the lightest neutrino mass, including θ_{13} results from Daya Bay. The figure shows ranges for both normal and inverted hierarchies. Figure from Bilenky and Giunti [5].

is necessary between the two electron emission nodes. Because of this, the half-life of $0\nu\beta\beta$ decay has the form,

$$(T^{0\nu}_{1/2})^{-1} = G^{0\nu} \cdot \mid M^{0\nu} \mid^2 \cdot \langle m_{\beta\beta} \rangle^2 \tag{1.5}$$

Where $G^{0\nu}$ is the phase space factor, $M^{0\nu}$ is the nuclear matrix element, and the effective mass, $\langle m_{\beta\beta} \rangle^2$ is given by:

$$\langle m_{\beta\beta} \rangle^2 = \mid \sum_i U^2_{ei} m_i \mid^2 \tag{1.6}$$

Figure 1.8 shows the range of effective Majorana mass as a function of the smallest neutrino mass. The phases, as well as uncertainties in the nuclear matrix elements produce sizable spreads in the possible effective mass. The hierarchy of neutrino masses also play a large role. Because of the presence of phases within the mixing matrix, it is possible, via fine tuning, for the effective mass to be vanishingly small in the case of a normal hierarchy. $0\nu\beta\beta$ decay experiments have a chance to prove that neutrinos are Majorana, but no real chance to disprove it. One subgroup of the Heidelberg-Moscow experiment has reported evidence for an effective mass, ($\sim$0.4 eV)[38], but this result has been invalidated by results from the GERDA experiment[39].

1.3 Other Theoretical Implications

One natural question to ask is why the neutrino masses are so small. Many theories are attempting to find the answer to this question, one of which is referred to as the see-saw mechanism. This theory posits that the light left-handed neutrino is balanced out by the very massive right-handed neutrino. The mass terms can be described by the matrix:

$$M = \begin{pmatrix} m_M^L & m_D \\ m_D & m_M^R \end{pmatrix} \tag{1.7}$$

For the relation, $m_M^R >> m_D >> m_M^L$, the lower mass eigenvalue of the mass matrix can be written:

$$\mu = \frac{m_D^2}{m_M^R} \tag{1.8}$$

For m_D of the quark scale, and m_M^R of GUT scale, this relation results in neutrino

masses that are a small fraction of an eV, and naturally results in a hierarchical neutrino mass structure ($m_1 << m_2 << m_3$). Coupled with the mass splitting results from oscillation experiments, the see-saw mechanism predicts neutrino masses too small to be seen in both Katrin and current $0\nu\beta\beta$ experiments.

However, the see-saw mechanism is only one such compatible theory, and others exist which predict quasi-degenerate neutrino masses, as well as Dirac nature neutrinos. The absolute neutrino mass is, therefore, a very important parameter in illuminating the neutrino's true nature.

1.4 Cosmological Measurements

The mass of the neutrino has broad impacts on the evolution of our early universe. Relic neutrinos should, in theory, have a negative effect on the formation of structure. The fraction of energy contained in neutrinos can be calculated according to:

$$\Omega_\nu h^2 = \frac{\sum m_\nu}{93\ eV} \tag{1.9}$$

As a free parameter, this quantity can be used in our cosmological models to measure the sum of neutrino masses. The best-to-date upper limit of the neutrino mass found from cosmological result is from the Planck satellite CMB experiment[40, 41]. The result from the Plank TT spectrum reports a maximum sum of neutrino masses of 0.715 eV. More stringent results are obtained when incorporating effects from lensing models and external data sets including CMB polarization data, and baryon acoustic oscillations. The most stringent limit found using all available data states that $\sum m_\nu < 0.23eV(95\%)$. It should be noted that cosmological results are still model dependent measurements, and it is still important to have direct laboratory

measurements in order to check the validity of the ΛCDM model.

Cosmology also has an input on the number of neutrino species. In contrast to collider measurements of Z production widths, cosmological measurements are not limited to weakly interacting neutrino species alone, and should be sensitive to sterile neutrinos as well. The effective number of neutrino species, N_{eff}, is related to the measured relativistic energy density of the early universe by the relation:

$$\rho_R = \left(1 + N_{eff}\frac{7}{8}\left(\frac{4}{11}\right)^{4/3}\right)\rho_\gamma \tag{1.10}$$

Assuming the presence of only three neutrino species, we expect a value of N_{eff} of around 3, though a couple effects modify the expected result to 3.046[42]. It should be noted that deviations from the expected value of N_{eff} does not necessarily indicate more neutrino species, since other unexplained relativistic degrees of freedom can have an effect on the relativistic energy density. The most stringent result, quoted from the Planck collaboration states $N_{eff} = 3.36 \pm 0.34$, which is still consistent with the standard model prediction. More detail behind cosmological measurements and how they inform our understanding of neutrinos can be found in the literature, in particular *Abazajian, et al*[43].

1.5 Direct Mass Measurements

Several model independent neutrino mass measurements have been attempted. One method is to do time-of-flight studies from supernovae, since massive neutrinos, traveling at some high fraction of the speed of light, should exhibit some time delay relative to photons. Analysis of neutrino detections following the supernova 1987a put an upper limit to the neutrino mass of 16 eV[44].

Kinematics is a very common way to probe the neutrino mass. Experiments have used pion and tau decays to find upper limits on the muon and tau neutrinos, respectively. The limits obtained thusly, however, are several orders of magnitude above the range expected based on the electron neutrino limit and oscillation data[45, 46]. For a good overview of past and future neutrino mass measurements, see *Drexlin, et al*[47].

1.5.1 Tritium Decay

The most successful kinematic method of neutrino mass measurement is through beta spectroscopy of tritium beta decay. In short, a small portion of the energy released in the beta decay is spent on the creation of the neutrino's mass, which has a small effect on the shape of the spectrum near the endpoint. The shape of the electron energy spectrum can be written:

$$\frac{dN}{dK_e} = C \times p_e(K_e + m_e)(E_0 - K_e) \sum_i \mid U_{ei} \mid^2 [(E_0 - K_e)^2 - m_i^2]^{1/2} \tag{1.11}$$

$$C = F(Z, K_e) \times \frac{G_F^2}{2\pi^3} \cos^2\theta_C \mid M \mid^2 \tag{1.12}$$

The Fermi function, F, and nuclear matrix element, M, have no dependence on the neutrino mass, which only shows up in the phase space factor written out above.

Because Katrin is not sensitive to the splittings between the neutrino mass states,

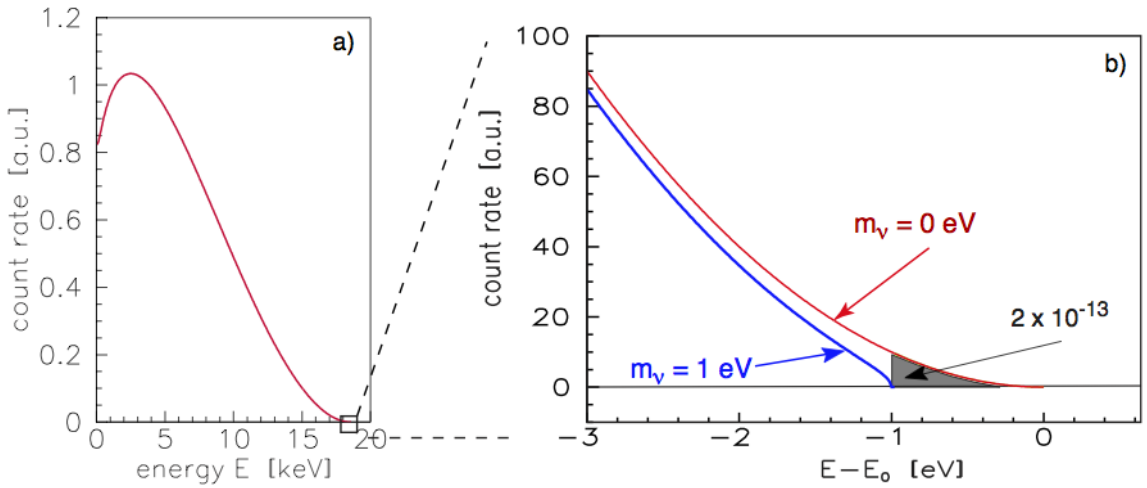

Figure 1.9: The tritium endpoint spectrum, showing the contribution from a neutrino mass of 1eV. Figure from the KATRIN design report[6].

we can simplify the spectrum to:

$$\frac{dN}{dK_e} = C \times p_e(K_e + m_e)(E_0 - K_e)[(E_0 - K_e)^2 - \langle m_\nu \rangle^2]^{1/2} \tag{1.13}$$

with the effective mass defined as the weighted average of all neutrino mass states:

$$\langle m_\nu \rangle^2 = \sum_i \mid U_{ei} \mid^2 \cdot m_i^2 \tag{1.14}$$

Figure 1.9 shows the effect a nonzero neutrino mass has on the tritium endpoint spectrum. The existence of sterile neutrinos, of course, adds additional mass terms, so the general equation 1.11 would be used to account for those additional masses.

The most commonly used isotope for neutrino mass measurements is tritium, which is ideally suited for the following reasons:

- Low endpoint (18.6 keV) accessible to electromagnetic spectroscopy
- Fairly low half life (12.3 yrs) allows high signal rate

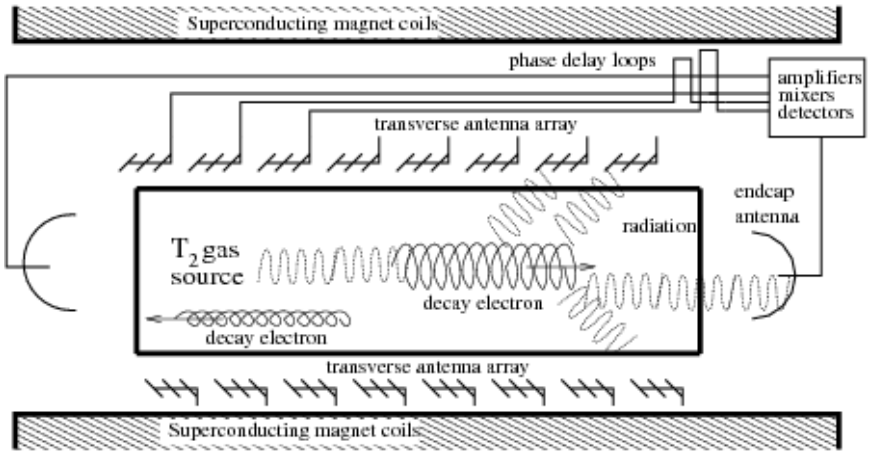

Figure 1.10: An illustration of the Project 8 method of beta spectroscopy through detection of cyclotron radiation from individual electrons. Figure from *Monreal and Formaggio*[7].

- Simple atomic structure of tritium and daughter ions
- Low Z minimizes inelastic scattering of outgoing electrons
- Super-allowed nuclear transition makes nuclear matrix element well understood

The current directly measured upper limit on the neutrino mass has been set from the tritium decay spectrum at both Mainz[48] and Troitsk[49], each quoting comparable upper limits of about 2 eV. This limit should be improved by a factor of ten following the conclusion of the KATRIN experiment.

Beyond KATRIN, a new spectroscopic technique will likely be required, given the scaling limitations of the MAC-E filtering technique used in KATRIN and the Mainz and Troitsk experiments. Project 8 aims to perform beta decay spectroscopy through the detection of the electron's cyclotron radiation[7, 50]. Recently, project 8 has achieved a major milestone in being the first to detect cyclotron radiation from single electrons- an important first step[51].

Chapter 2

KATRIN

2.1 Goals

The KArlsruhe TRItium Neutrino experiment will perform a neutrino mass measurement to within 0.2 eV[6]. The experiment is housed at the Karlsruhe Institute of Technology inside its state of the art tritium laboratory.

In addition to the planned neutrino mass scale measurement, KATRIN has possible insight into the presence of sterile neutrinos. First, KATRIN will probe a portion of the allowable mixing space for sterile neutrinos at the eV scale, without any modification or additional runtime. This is due to the fact that the tritium spectrum is a weighted sum of that produced by each neutrino mass state. Though the three known mass states are too close to be differentiated in this way, an eV-scale neutrino could be detectable depending on the mixing parameters.

KATRIN also has the ability, with modification, to probe the existence of keV-scale sterile neutrinos. This measurement would require modifications to the standard KATRIN setup, and cannot be done concurrently with the neutrino mass scale mea-

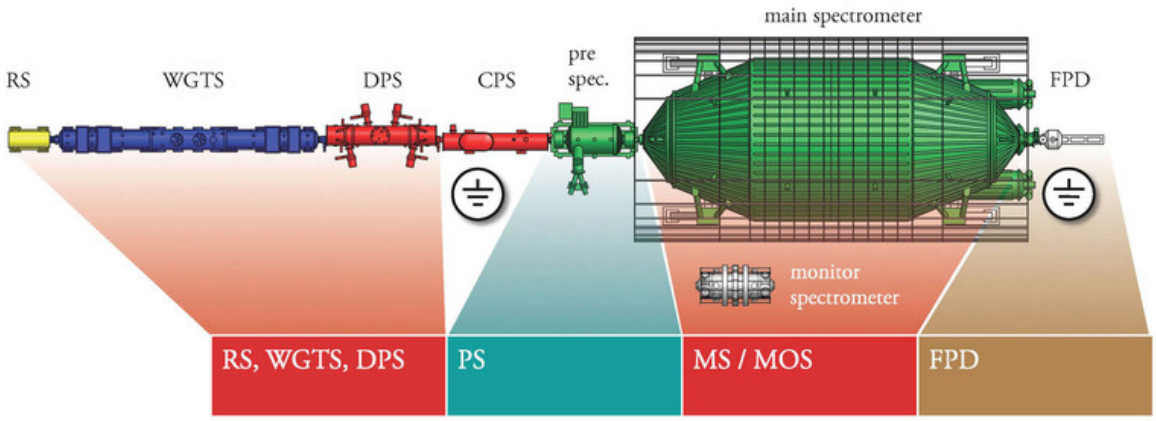

Figure 2.1: An overview of the KATRIN experiment showing the rear section, windowless gaseous tritium source, differential pumping section, cryogenic pumping section, pre spectrometer, main spectrometer, monitor spectrometer, and focal plane detector. Figure from the KATRIN collaboration.

surement. The modifications necessary, primarily limited to detector changes, are currently under development, and a keV scale sterile neutrino search is planned after the conclusion of the tritium endpoint measurement.

2.2 Experiment Overview

The experimental main beam line is comprised of several sections:

- A rear section to house calibration systems (talked about in depth below)
- A windowless gaseous tritium source producing 9.5×10^{10} electrons per second inside a 3.6 T magnetic field
- A transport and pumping section, consisting of differential and cryogenic pumping, which magnetically guides electrons while reducing the pressure from 3×10^{-3} to 10^{-11} mbar

- A pre-spectrometer to reject most of the electrons and minimize ionizations of residual gas in the main spectrometer
- A main spectrometer of the MAC-E filter type to perform the high precision energy measurement
- Finally, a pixelated silicon PIN diode to count electrons

In addition to the main beam line, an additional beam line is used to monitor the high voltage supply of the main spectrometer. This monitor beam line uses a third spectrometer (which is actuality the spectrometer used in the Mainz experiment), in addition to a condensed krypton monoenergetic source. The main spectrometer voltage is divided down to the center of the krypton line and plugged into the monitor spectrometer retarding potential. Small changes in the retarding potential will, thusly, produce large deviations in countrate in the monitor beamline, producing very sensitive monitoring of the main spectrometer potential.

2.3 Spectrometer Design

The Katrin main spectrometer is called a MAC-E (Magnetic Adiabatic Collimation Electrostatic) Filter. This conceptual design has been in use in both the Mainz and Troitsk experiments. In short, it is an electrostatic high-pass filter that uses magnetic collimation to reduce its transmission function. The main difficulty in designing an electrostatic filter is that an electric field can only affect momentum along the direction of the field. In the case of Katrin, tritium electrons are emitted isotropically and reach the spectrometer retardation plane at a variety of pitch angles, smearing out the spectrometer transmission function.

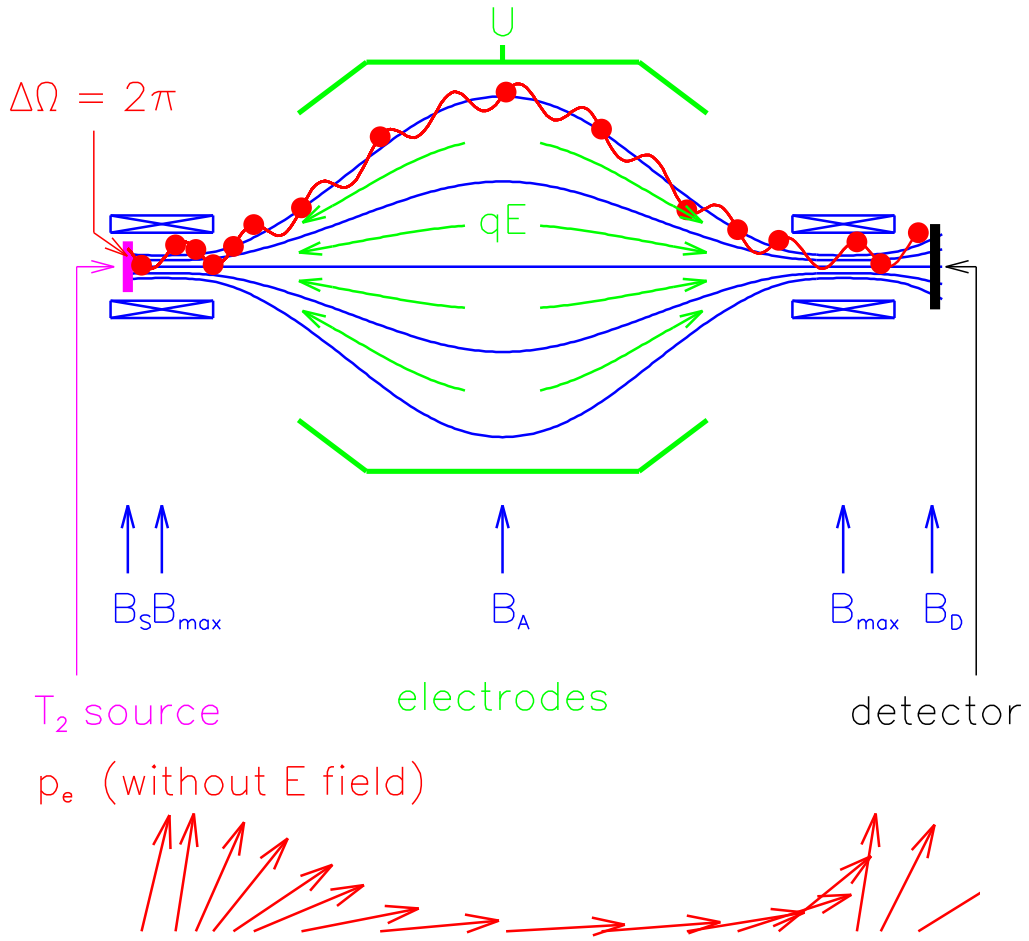

Figure 2.2: An illustration of the MAC-E filter, showing its effect on pitch angle for an electron undergoing cyclotron motion. Figure from the KATRIN design report.

Adiabatic guiding of the electrons provides the answer to this problem. Under adiabatic motion (in this case, meaning that the electric and magnetic fields change very little over the course of one cyclotron orbit) the dipole moment due to the electron's cyclotron motion remains constant. This dipole moment can be written:

$$\mu = \frac{E_\perp}{B} \tag{2.1}$$

Here, $E_\perp$ refers to the component of kinetic energy associated with its cyclotron motion. As a reminder, this is also the portion of the energy that is not measurable by electrostatic filtering. From the formula, we see that as long as the electron's motion is adiabatic, one can lower the transverse energy of the electron simply by reducing the magnetic field. As a consequence of this, the inherent energy resolution of the MAC-E filter can be written:

$$\frac{\Delta E}{E} = \frac{B_{max}}{B_{min}} \tag{2.2}$$

Figure 2.2 illustrates this concept. Of course, with the reduction in magnetic field, the analyzing plane must increase in size in order to encompass the same magnetic flux. This is exactly the reason that the extreme size of the KATRIN main spectrometer is necessary. KATRIN's design parameters have set $B_{max} = 6\ T$ and $B_{min} = 3\ G$ for a transmission function width under an eV.

In figure 2.3, we see a more detailed schematic view of the magnetic fields used in the spectrometer. Of particular note is the use of the pinch magnet with a field higher than that present within the source. This configuration allows for the narrowing of the spectrometer transmission function while also reflecting electrons with high pitch angle, which have a higher probability of scattering within the source. The maximum

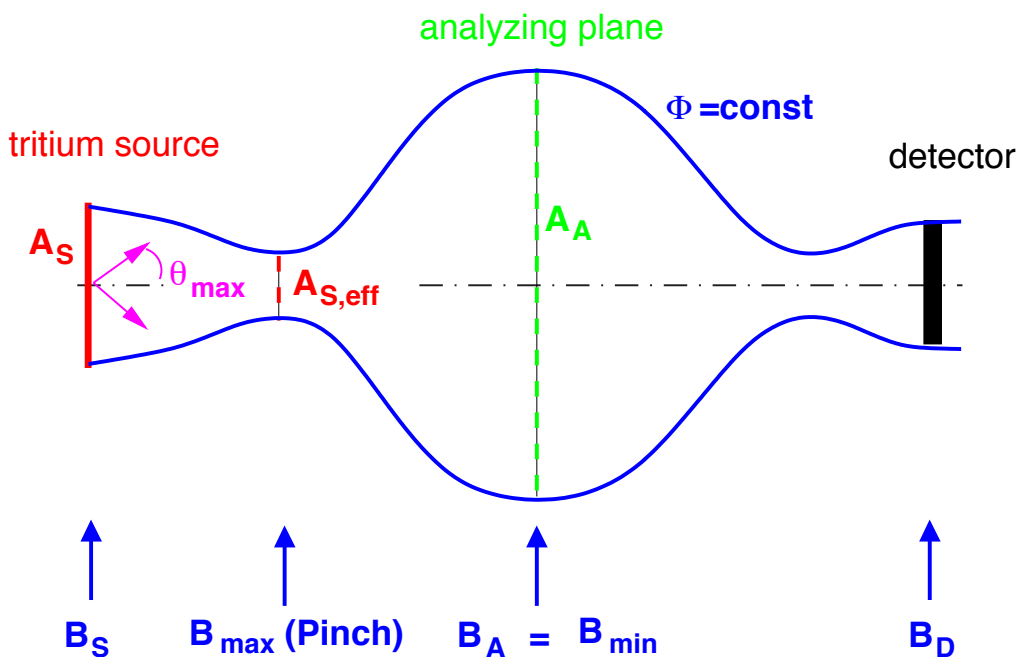

Figure 2.3: A more detailed illustration of the MAC-E filter magnetic field configuration.

starting pitch angle is:

$$sin\ \theta_{max} = \sqrt{\frac{B_{source}}{B_{max}}} \tag{2.3}$$

With the KATRIN source field value set to 3.6T, electrons emitted with pitch angle $\theta > 51°$ will be reflected at the pinch magnet. Reducing the number of high pitch angle electrons is important because reducing the number of electrons with large path lengths through the source also reduces systematic errors due to inelastic scattering.

2.4 Tritium Source Parameters

Apart from the transmission function of the main spectrometer, the other major limiting factor in the KATRIN neutrino mass measurement is signal rate. Therefore, design of source parameters is of utmost importance. Furthermore, because KATRIN will ultimately measure an integral spectrum, variations in source strength need to be minimized and closely monitored.

To begin, we can write the signal rate in the form:

$$S = N * f_\theta * P_0 \tag{2.4}$$

Here, N refers to the number of tritium decays in the source, f_θ is the fraction of decays with acceptable solid angle, and P_0 is the fraction of electrons that do not undergo scattering within the source. The fraction, f_θ can be written simply,

$$f_\theta = 1 - cos\ \theta_{max} \tag{2.5}$$

The number of decays, N, is proportional to the cross sectional area of the source, A_S, the purity of the source, ε, and the column density, pd:

$$N = k * A_{source} * \varepsilon * pd \tag{2.6}$$

The proportionality constant, k, is related to the decay rate of tritium in the energy range we are interested in.

The cross section area of the source is related to the area of the spectrometer, due to the extra magnetic flux that would have to be contained within the spectrometer,

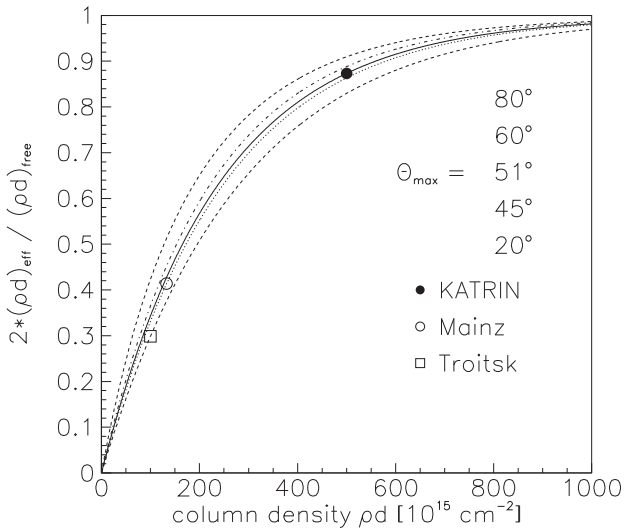

Figure 2.4: The *effective* column density (normalized according to its asymptotic maximum) plotted against its actual column density. As shown, the effective column density (and thus, the signal rate) reaches a maximum due to increased incidence of scattering within the source.

by the relation:

$$\frac{A_{source}}{B_{source}} = \frac{A_{spectrometer}}{B_{spectrometer}} \tag{2.7}$$

As discussed before, assuming the spectrometer size and B_{max} are both at their practical limits, this additional magnetic flux would only be contained by increasing B_{min}, which widens the spectrometer transmission function.

The column density, pd, also cannot be increased at will, because it also increases scattering, decreasing the percentage of electrons that make it to the spectrometer without energy loss (see figure 2.4). Furthermore, increasing the column density also increases the potential systematic error due to inelastic scattering in the tritium source. KATRIN will apply a column density of $pd = 5 \times 10^{17}$ molecules/cm^2.

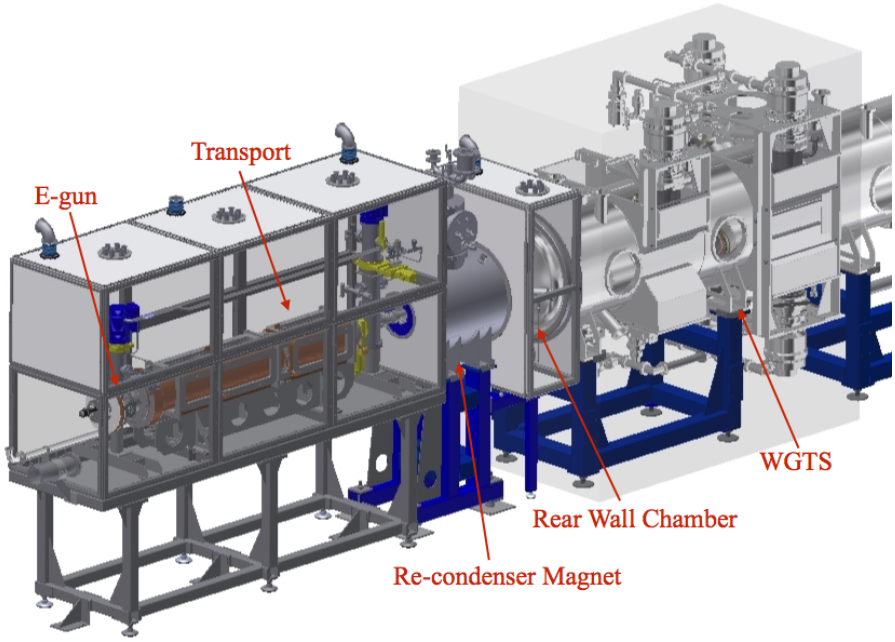

Figure 2.5: A CAD view of the rear section, containing many of the KATRIN calibration systems. From the left we see the electron gun, transport section, the re-condenser magnet, the rear wall chamber, and the rearmost portion of the windowless gaseous tritium source.

2.5 The Calibration and Monitoring Systems

As noted in the previous section, the source monitoring systems are incredibly important for KATRIN operation. The main components consist of:

- An angular selective electron gun for measuring the main spectrometer transmission function and source column density.
- A rear wall electrode that can define the tritium source potential.
- Source activity monitoring via Bremsstrahlung X-ray detection[52, 53].

- In-line source isotope monitoring via Laser Raman spectroscopy[54, 55, 56, 57].

The last item, dealing with source activity monitoring and isotope purity monitoring, will not be detailed in the remainder of this paper so the reader is directed to explore the sources cited for more information.

2.5.1 The Rear Wall and Source Activity Monitoring

The two main requirements of the rear wall dictate its design. These requirements once again, are:

- Define the tritium source potential. In particular, the work function must be well known and homogenous across the surface. Tritium adsorption must be minimized to keep the work function steady.
- Monitor the source activity in real time.
- Allow for production of photoelectrons to counteract potential space charge buildup in the WGTS.

The surface material that satisfies these conditions is gold. Many substrate materials have been investigated, including beryllium, sapphire, and silicon, before finally settling on stainless steel because of good work function uniformity results obtained from early prototypes. Work function homogeneity is chiefly important because it defines the reference potential for electrons emitted within the source. Rear wall samples have been tested using a scanning Kelvin probe and an atomic force microscope using kelvin force microscopy (see figure 2.7.

The other requirement- monitoring the source activity- is accomplished by detection of the Bremsstrahlung X-rays originating from electrons impacting the gold

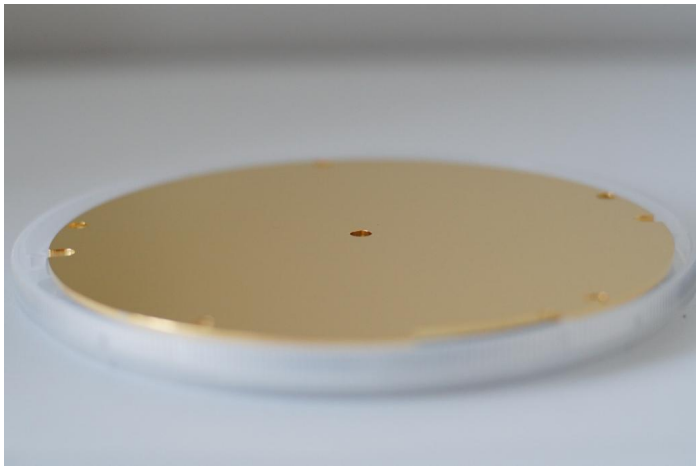

Figure 2.6: One rear wall sample made to the final design. The holes and channels along the outside are used for mounting, while the hole in the center is used for electron transmission. Photo from K. Schoenung.

surface. One method of source activity monitoring that was previously explored used a multilayer structure grown on a silicon substrate. The fabrication of such a device proved to be too difficult, and the idea was abandoned. Nonetheless, some results obtained can still be interesting and the techniques may prove useful in other applications, so the work done toward that goal is detailed in chapter 3.

2.5.2 The Electron Gun

The electron gun is the primary means of measurement and calibration once KATRIN has begun data taking. It will be used for multiple purposes, including spectrometer transmission function measurements, electron-tritium energy loss function measurements, periodic column density determination, and trap formation explorations. The electron gun must be able to produce electrons at any pitch angle within the tritium source. More discussion of the electron gun design and construction is in chapter 4.

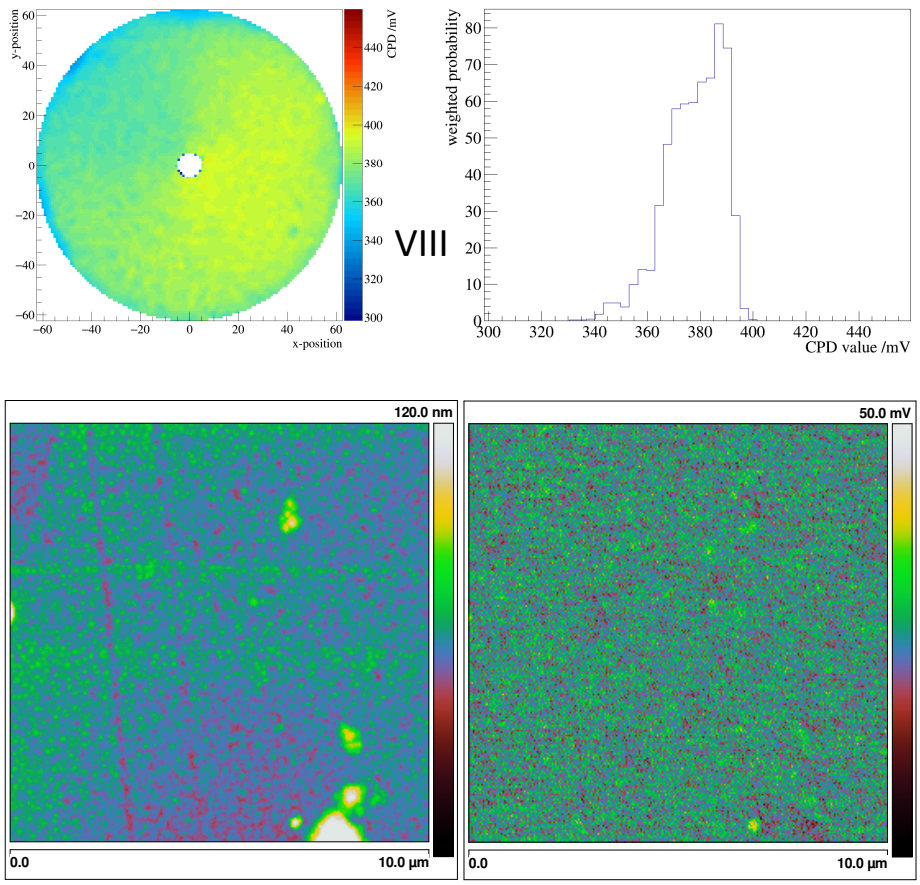

Figure 2.7: Work function uniformity measurements of rear wall samples using a Kelvin probe for macro-scale uniformity (top) and atomic force microscope for nano-scale uniformity (bottom). The AFM scan is composed of a topology scan (left) and work function scan (right). Kelvin probe figure courtesy K. Schoenung.

Chapter 3

Multilayer Rear Wall Production and Testing

The multilayer rear wall was designed to provide a method of monitoring the source activity. While it was found to be insufficient to work within KATRIN, progress made toward that goal may find use elsewhere, and is detailed here. First, was a concept which used a thin insulator. When problems arose within this concept, another idea was devised using a thick insulator.

3.1 Thin Insulator Concept

The idea behind the thin insulator design is simply to use the layers of the structure as an energy selective charge collection device. The device is fabricated starting with a conductive or semi conductive substrate. Upon this substrate a thin insulator is grown or deposited, followed by deposition of a thin gold layer of 50nm.

When exposed to a tritium source, high energy electrons (of more than a few

keV) can penetrate through the insulation layer and into the substrate, where they are separated from ions and low energy electrons, which are stopped in the gold surface. This is beneficial because the number of ions and secondary electrons depend on processes within the plasma that are not well understood. An off-the-shelf pico ammeter is good enough to measure current out of the substrate to measure the source activity to within the target precision.

3.1.1 Fabrication and Results

Prototypes of different material were made using 3-inch silicon wafers (1-10 Ω-cm, P-type). Samples were fabricated within the nano fabrication facility at UCSB, a high-quality facility capable of most common techniques used in nano fabrication and materials research.

Early on in the development process, it was thought that the rear wall would have to be made out of beryllium due to design constraints. To avoid health complications inherent with beryllium, silicon wafers were coated in aluminum in order to test the feasibility of deposition techniques onto an electrical conductor.

The insulation layer consisted of silicon dioxide or aluminum oxide, and was deposited using two techniques. The first was ALD (atomic layer deposition) which has the advantage of being completely conformal and having few pinholes. The second technique was PECVD (plasma enhanced chemical vapor deposition), which is a much faster process than ALD, but produces layers that lack the quality. It was observed that pinholes were reduced by using a combination of the two processes, with thicknesses of about 50nm ALD, and 100nm PECVD. ALD was used to deposit either aluminum oxide or silicon dioxide, while PECVD was only used to deposit silicon dioxide. An SEM cross-sectional image is shown in figure 3.1.

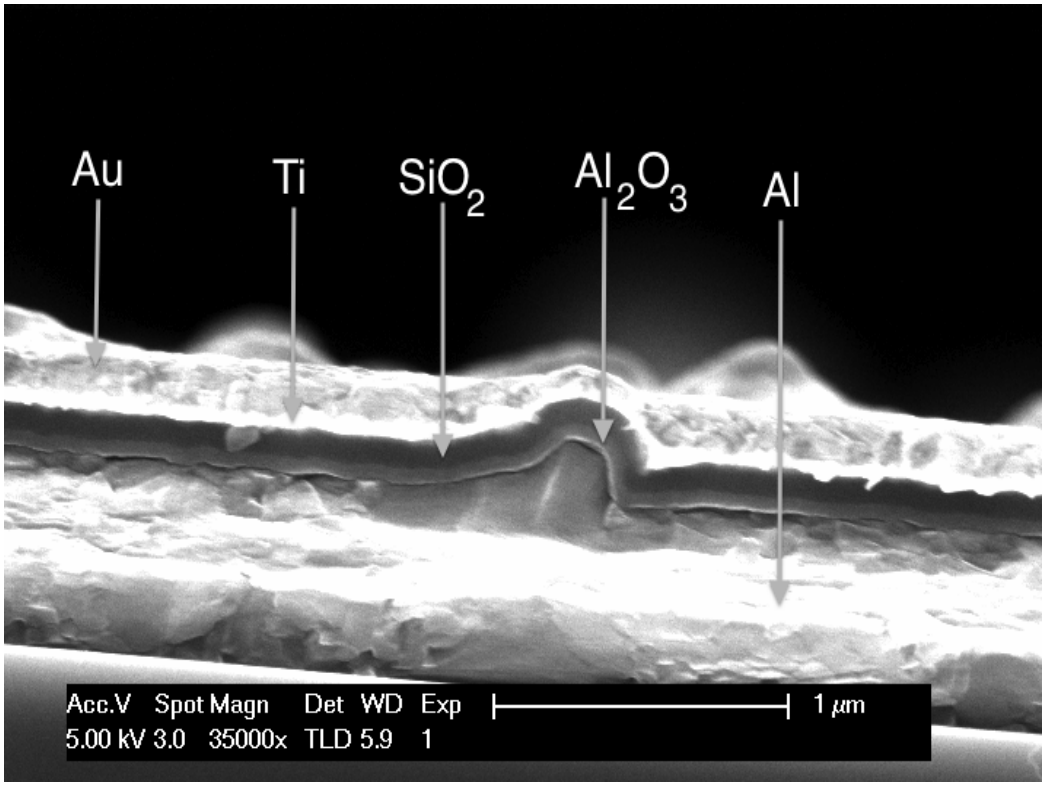

Figure 3.1: SEM image showing the layers deposited in the fabrication of early multilayer prototypes.

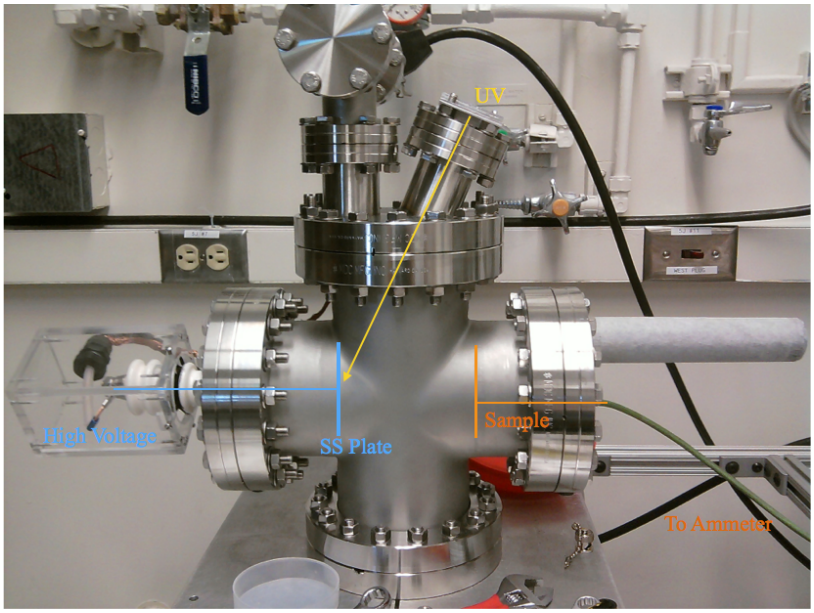

Figure 3.2: The test setup for multilayer rear wall testing. Overlayed shapes show the approximate locations of the sample, the stainless steel photoelectron plate, and light source.

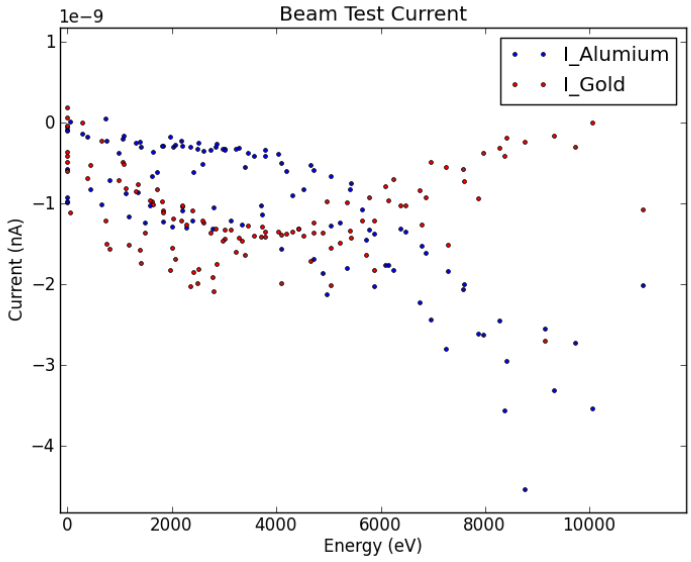

Figure 3.3: A proof-of-concept measurement showing the current measured from each conducting layer in an early multilayer prototype.

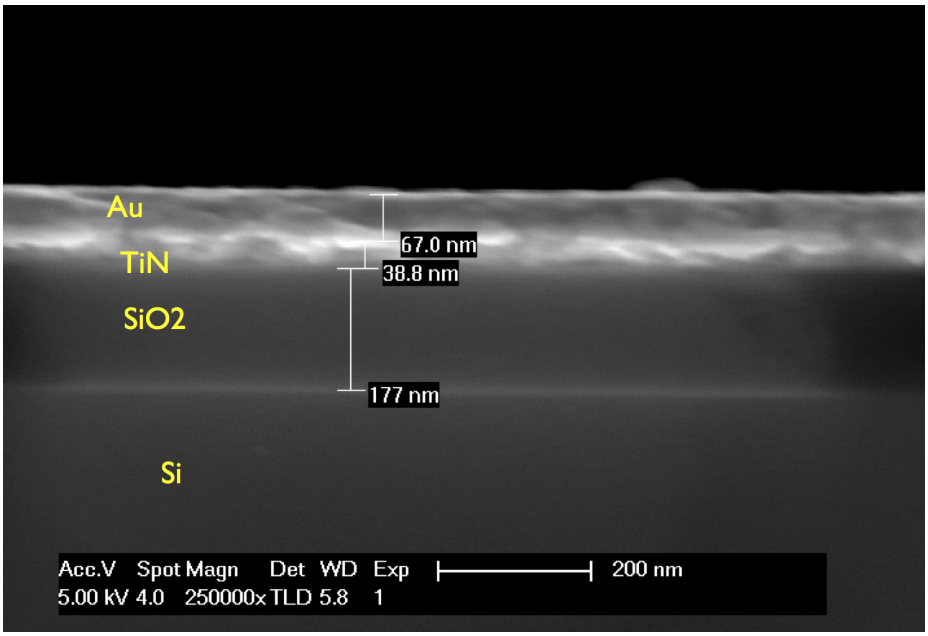

Figure 3.4: SEM image showing the layers deposited in the fabrication of a silicon prototype.

One early success has led to the measurement shown in figure 3.3. Electrons were generated by UV illumination from a deuterium lamp pointed at a stainless steel surface. As can be seen, the behavior of the device is as expected, as higher (negative) currents are seen on the substrate layer as the electron beam energy is turned higher.

The large spread in current values was due to high amounts of noise and short time spent on the measurement. Plans were made to improve the measurement to obtain cleaner results, but the device subsequently sustained damage which caused a short to form between the gold and aluminum layers.

When design changes were made to the rest of the rear section of KATRIN, it became possible to use other materials, and we began to explore silicon as a substrate. Thermal oxidation was used to produce silicon dioxide, but none of the samples had

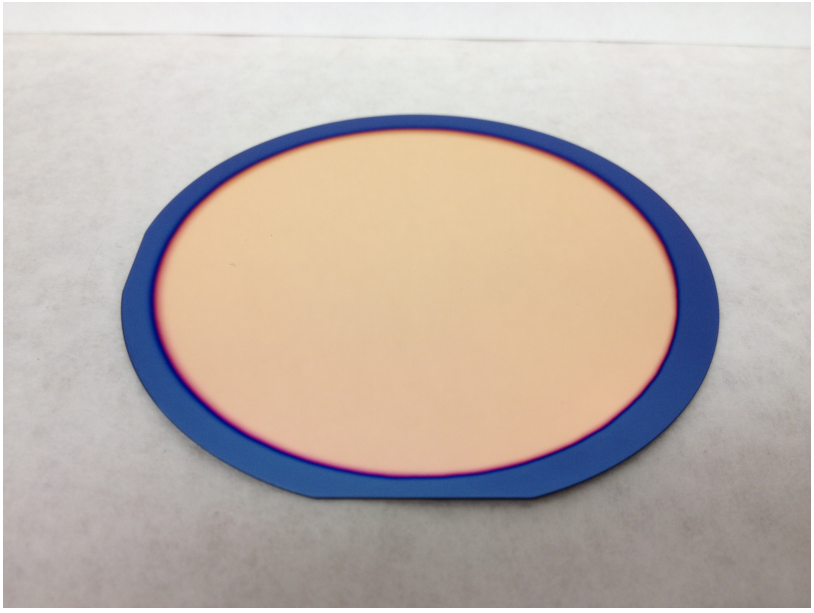

Figure 3.5: An example silicon prototype. The blue color seen in the silicon is due to thin film optical interference.

sufficient insulation between the gold and silicon layers. Figure 3.4 shows the cross-section view of one of these prototypes.

What may be apparent is that the difficulty in creating the multilayer structure with such a thin insulation layer is that it is very hard to avoid pinholes that cause short-circuiting between conducting layers. While it was possible at sizes 1-2 inches in diameter, at 3-inches and above, the failure rate was too large to be practical. Perhaps the technique can be used for applications only requiring small devices.

3.2 Thick Insulator Concept

We attempted to minimize the risk of pinholes by growing thicker insulation layers ($\sim 1\mu$m). At this thickness, virtually all samples had good insulation. However, electrons of energy $\sim$18 keV will not penetrate through to the conducting layer beneath.

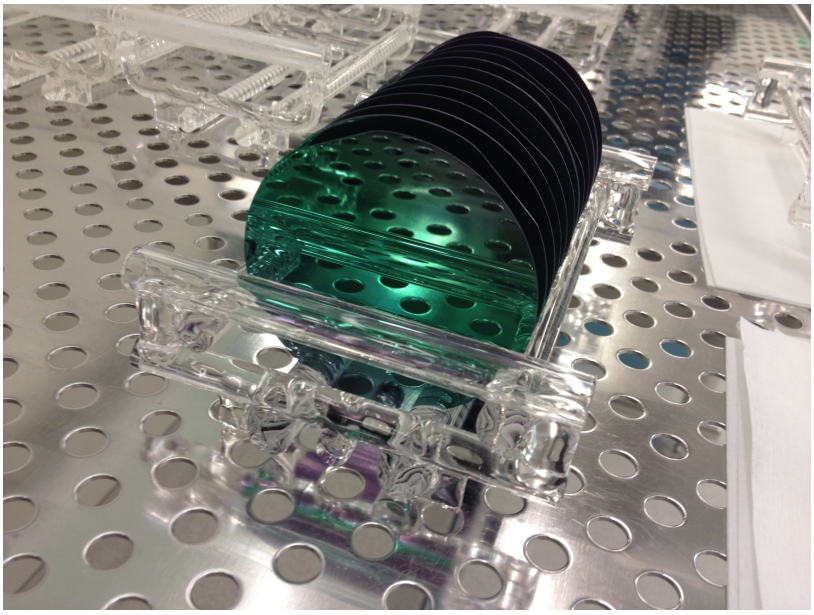

Figure 3.6: Silicon wafers following 1 micron oxidation

We made the decision to try using the insulator as an active detection region. A bias between the gold and silicon regions was applied, so that electron-hole pairs produced inside the insulator could be collected. This detection method has been used in other applications, including micrometeoroid detection[58, 59, 60].

3.2.1 Fabrication and Results- Thick insulator

A thermal wet oxide growth to 1 μm was performed on several 3-inch diameter samples at 1050 degrees C. The oxide was etched in patches on the backside of the wafers using hydrofluoric acid before deposition of aluminum to produce contact with the silicon layer. Titanium nitride and gold were sputter deposited onto the surface. The insulation between gold and silicon layers were measured to be of order 10s to 100s of MΩ.

A series of measurements were made using the same setup in the previous section.

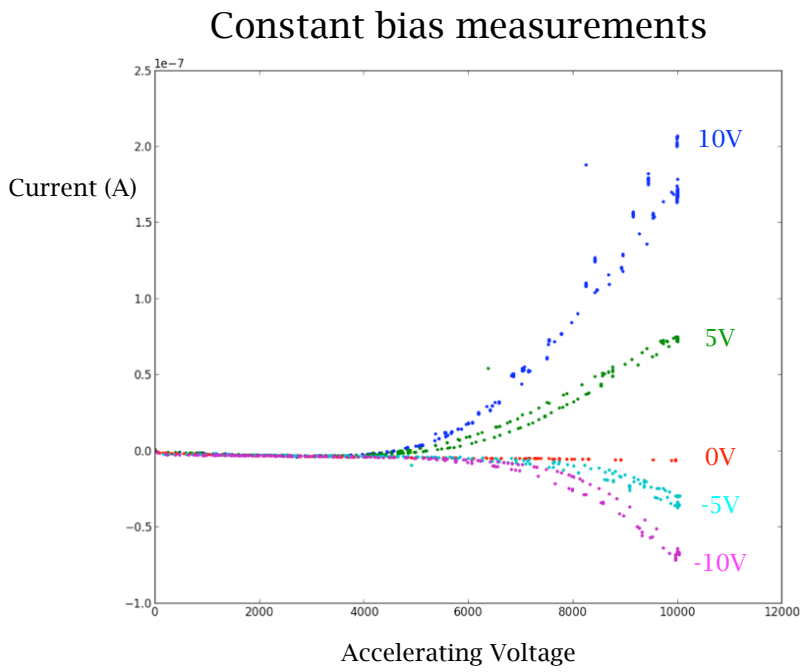

Figure 3.7: Current measured from the silicon layer of a thick insulator multilayer prototype, for different applied voltages.

Some results are shown in figures 3.7, 3.8 and 3.9.

Figure 3.7 shows results from a measurement in which the bias across the insulation layer was held constant while the beam energy is varied. Current is measured off of the gold surface (which is roughly grounded), while the indicated voltage is applied to the silicon layer. A few observations can be made. First, we note the large amplification in current due to electrons and holes created by electrons within the oxide (for comparison, the "0V" set of data represents the current impinging on the gold surface due to the beam itself).

Next, we note the asymmetry between currents measured from positive and negative biases.

Another observation is of the apparent hysteresis seen as the accelerating voltage

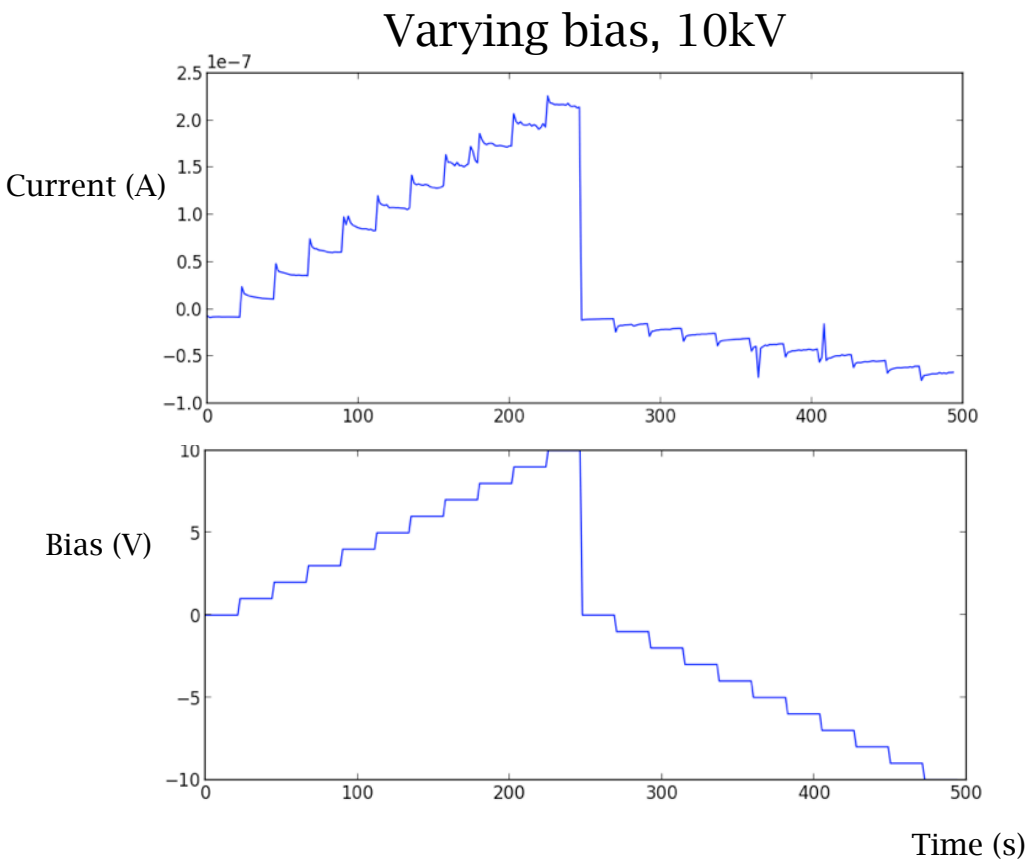

Figure 3.8: The time dependence of the current as the bias voltage is changed in a thick insulator multilayer prototype.

is swept up and down. This hysteresis can be explained by the presence of space charge that continues to migrate out of the insulator.

We can further explore the presence of space charge within the insulator by varying the bias voltage applied to the silicon layer. Figure 3.8 shows the time dependent behavior of the current as the bias voltage is changed. The current immediately jumps, and decays down to a steady state. We believe this decay is due to the presence of space charge that has accumulated under the lower bias voltage. As the higher bias allows the charge to drift more quickly toward the conductive layers, the

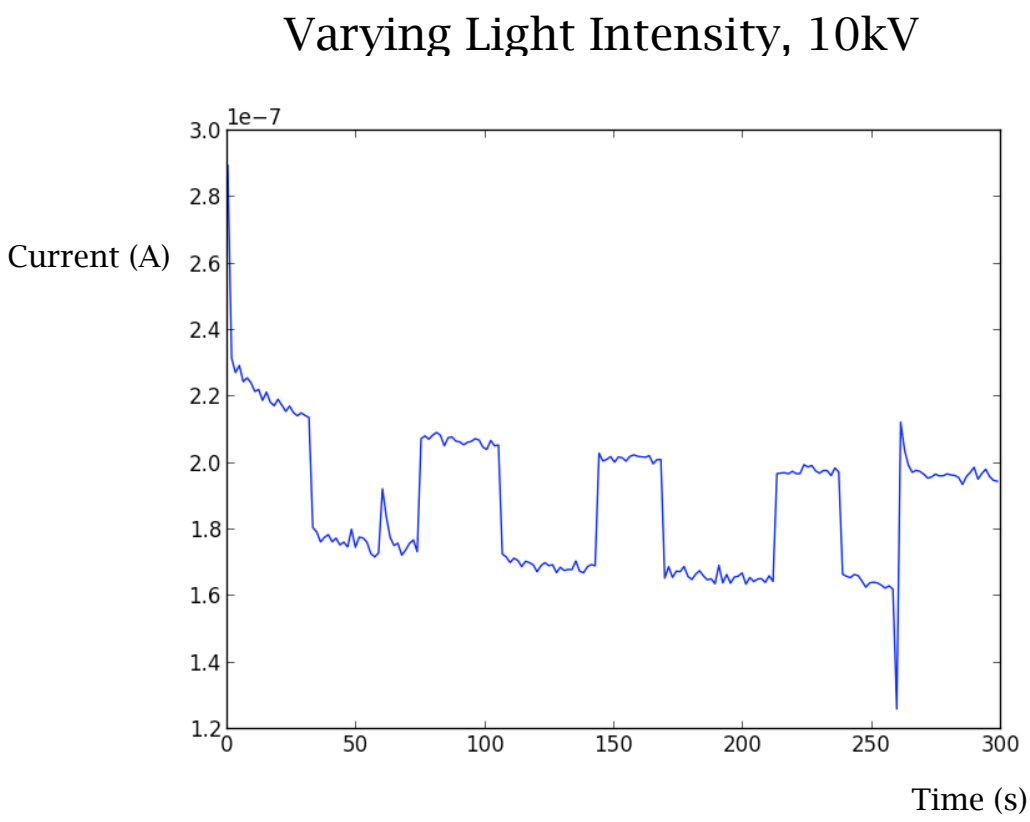

Figure 3.9: The effect of varying the current of the electron beam by changing the UV light levels. Sudden changes in current correspond to sudden changes in the light level by means of occluding the light source.

space charge diminishes, and we see the current drop.

Finally, figure 3.9 shows the responsiveness of the system to varying of the electron beam current. We can see that the current measurement responds within a second to changes in the beam current. Though the problem of space charge and uncertainties that come with it create doubts when it comes to the use of this device over long time scales, it looks promising when it comes to detecting short term changes.

Though this technique showed promise and warranted further investigation, it too suffered one fatal flaw. The high capacitance of such a large multilayer device caused unstable behavior in the ammeter measurements. The oscillations we observed

following this first set of measurements were due to this capacitance causing positive feedback within the input stage of the ammeter. The circuit contained within the input stage of the ammeter is standard among high precision instruments, and we determined that trying a different measuring device was unlikely to help, and no other solution was found for stopping these oscillations without subsequently hindering the measurement. Once again, if the application could make use of smaller devices, this problem would have been alleviated.

Chapter 4

The Electron Gun

As stated previously, the electron gun has use in many calibration measurements during KATRIN operation. These measurements include spectrometer transmission function measurement, electron energy loss functions, tritium column density determination, and trap formation studies.

To accommodate the different measurements that are needed, the electron gun has to be designed for two different modes. First, the high rate mode has the following requirements:

- Rate $R > 10^6\ e^-/s$
- Energy Spread $\Delta E < 2\ eV\ rms$

And for the low spread mode, we have the following requirements:

- Rate $R \geq 10^5\ e^-/s$
- Energy Spread $\Delta E < 0.2\ eV\ rms$

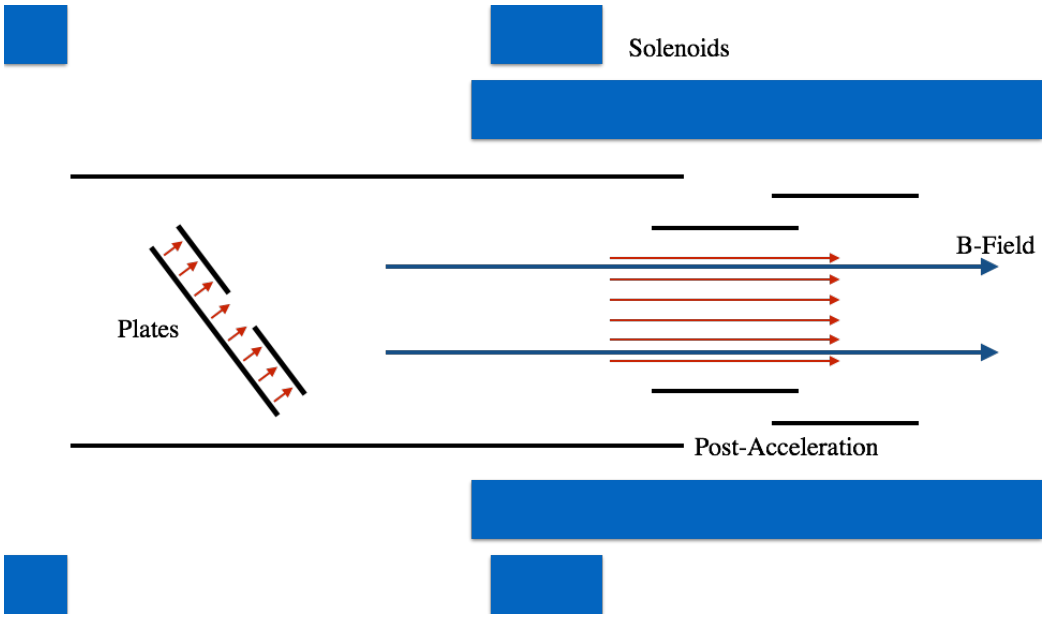

Figure 4.1: A conceptual representation of the electron gun design. Solenoids are represented in blue, with electrodes in black. Regions of high electric field are indicated with red arrows.

- Stability $\Delta R/R < 10^{-3}$ over three minutes

Both modes must support electron energies up to 20keV, with tunable pitch angle to 51° within the WGTS. These requirements were fulfilled using an innovative design using a set of tilted acceleration plates and post-acceleration.

4.1 Electron Gun Electromagnetic Design

Figure 4.1 shows the conceptual design behind the operation of the electron gun. Electrons originate from a gold-terminated fiber in the rear plate. A potential of a few kilovolts between the back and front plates give the electrons the transverse momentum necessary to generate high pitch angles. A cylindrical electrode surrounding the plates, called the "drift chamber," is held at the same potential as the front plate,

keeping the drift region virtually free of any electric field. The rest of the acceleration takes place within a guide solenoid, by use of a pair of cylindrical post-acceleration electrodes. By keeping the post-acceleration region within an area of high magnetic field, we preserve adiabaticity, which is an important aspect when attempting to measure the electron pitch angle.

Post-acceleration Concept

To understand how the electron pitch angle is measured, we first remind ourselves of the properties of adiabatic transport. As noted before, the magnetic moment due to the cyclotron motion remains constant under adiabatic transport. The magnetic moment is written:

$$\mu = \frac{E_\perp}{B} \tag{4.1}$$

Where $E_\perp = p_\perp^2/2m$, or the component of the energy associated with the cyclotron motion. Using the previous equation, assuming one knows $E_\perp$ at any point, knowledge of the magnetic field allows for the calculation of $E_\perp$, and by extension the pitch angle, at any point where adiabaticity holds. With this in mind, we express the electron pitch angle in the following way:

$$\sin^2\theta = \frac{E_\perp}{E_\perp + E_\parallel} \tag{4.2}$$

During a pitch angle calibration run, the post-acceleration voltage is decreased while the voltage between the plates are held constant. The post-acceleration region of the electron gun only alters $E_\parallel$. As $E_\parallel$ decreases, the pitch angle increases to the point that electrons become magnetically reflected at the 6T pinch magnet. We can

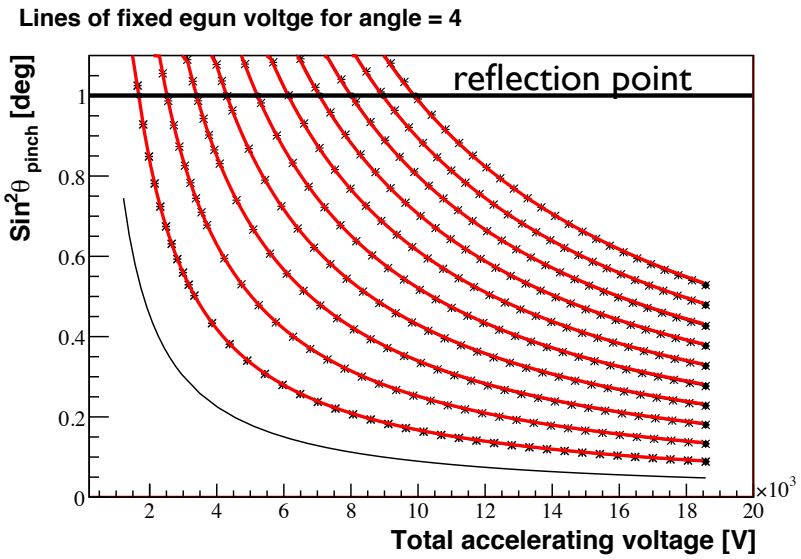

Figure 4.2: Simulation showing the accuracy of the pitch angle calibration procedure. Each curve corresponds to a different plate voltage. The points are individual simulations, and the red lines are the extrapolations based on the reflection point.

tell when the electrons are reflected by monitoring their count rate at the detector. We can label the total electron energy at reflection, E_R. At other post-acceleration voltages, the pitch angle at the pinch magnet is the following:

$$\sin^2 \theta_{pinch} = \frac{E_R}{E} \tag{4.3}$$

Once again, when the pitch angle is known anywhere, it can be calculated anywhere in which the magnetic field is known.

To see how the calibration procedure would work, refer to figure 4.2. The post-acceleration voltage is stepped down until the reflection point is measured, and the pitch angle at full voltage can be extrapolated. It should be noted that some parameter sets (those resulting in very low pitch angle) don't ever produce reflection at the pinch magnet, and the pitch angle will not be calibrated in those cases.

Following the post-acceleration section, there is an electron transport section that guides the electrons into the source section. The transport section uses three solenoids, along with two sets of magnetic dipoles for steering in both dimensions. There is also a set of electric dipoles, which are used for clearing any trapped electrons, via $\vec{E} \times \vec{B}$ drift.

4.2 Prototype Design and Construction

Electromagnetic design optimizations were done by collaborators at KIT, and the full mechanical design was split among several people in KIT and UCSB. The electron gun was then constructed at UCSB in order to test its performance. Figures 4.3 and 4.4 show photos of different components of the electron gun that were taken during the construction process.

The UV light source is a laser-driven Xenon light source from Energetiq. The light source was chosen because we did not achieve high enough electron rates with a deuterium lamp. Light is filtered using one of several short wavelength filters in a filter wheel, and focused on the end of a fiber mounted inside the electron gun vacuum system. The other end of the optical fiber is located at the rear plate electrode, and is vacuum deposited with 40 nm of gold for photoelectron emission.

4.3 Prototype Testing and Results

The main purposes of the electron gun testing are summarized as follows:

- Verify voltage stability
- Measure energy spread, count rates, and beam size

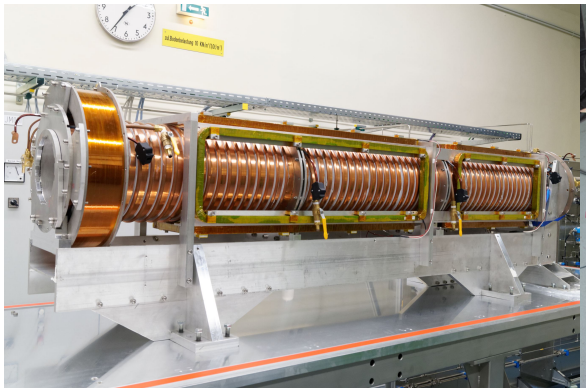

(a) The electron gun solenoids

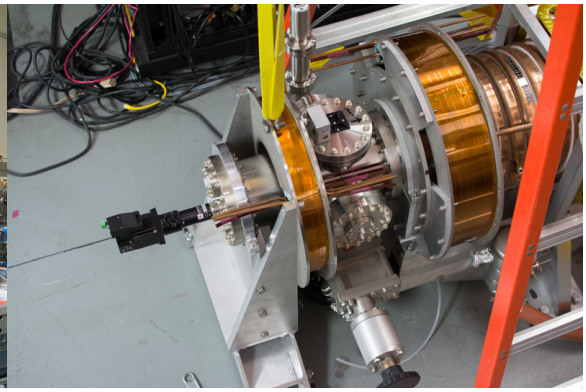

(b) The exterior of the electron gun source end

(c) The electric dipole assembly, used to clear trapped electrons

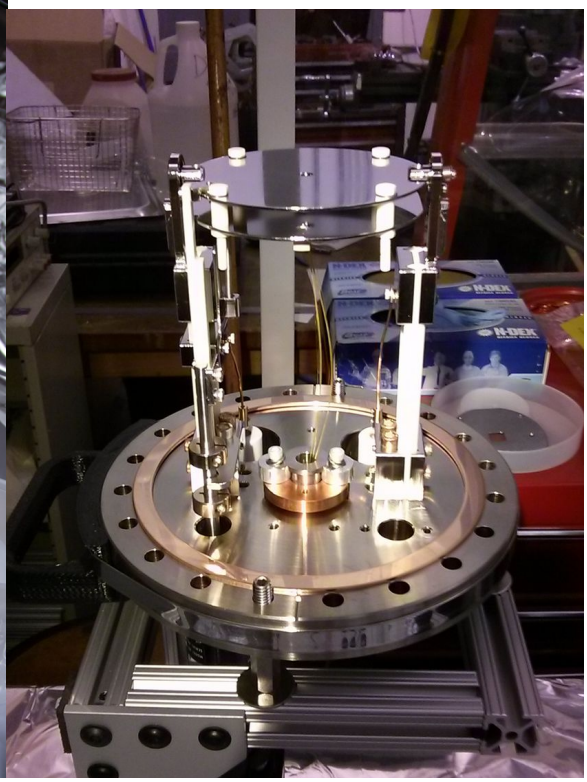

(d) The electron source plates

Figure 4.3: Some photos of the major components of the electron gun. Photos courtesy Greg Courville and Florian Priester.

Figure 4.4: Some other components of the electron gun, including the drift chamber (central long cylindrical electrode), and postacceleration electrodes (right front assembly). Photo courtesy Greg Courville

- Demonstrate angular selectivity
- Measure the rate stability
- Search for stray light electrons
- Verify dipole electrode functionality

The first item and last three items will not be discussed in detail here. It is sufficient to say that we did not encounter any large issues. We did not encounter troubling high voltage instabilities or evidence for electrons from stray UV light. Also, the rate stability was measured at 0.15% RMS over 90 minutes without any work put into stabilizing the UV light source, so we expect the performance to improve. Lastly, the purpose of the dipole electrodes is to clear any trapped electrons between the electron gun plates and any other high voltage sources, like the pre and main

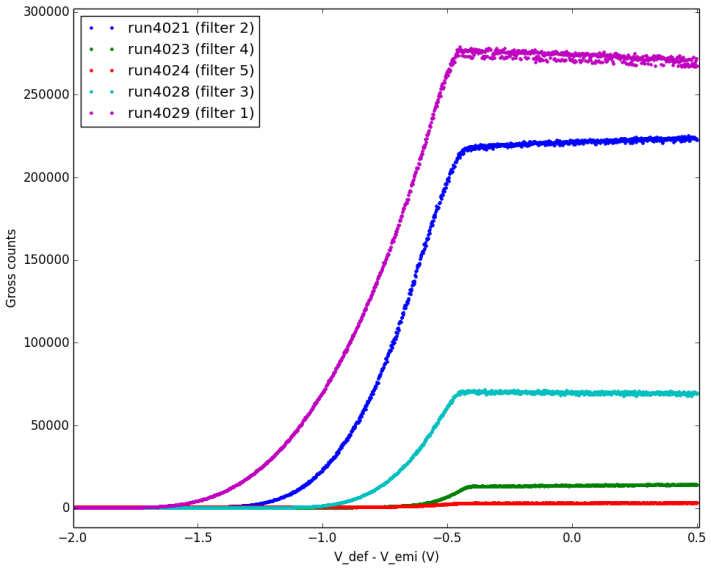

Figure 4.5: Electron counts as a function of offset voltage between the two electron gun plates.

spectrometers. We created a penning trap by placing a spectrometer near the electron detector, and found no evidence of trap filling when the dipoles were on voltage.

Energy Spread

To measure the electron energy spread, we measured the electron count rates as we varied the voltage separation between the front and back plate of the electron gun. This measurement used a specially designed floating voltage source to carefully control the voltage separation while keeping both electrodes at high voltage. Figure 4.5 shows the measurement results for several filters. Filters 1 through 3 all had RMS energy spreads below 0.2 eV, with filter 3 nearing 10^5 electrons per second. The high electron rate mode, which needs 10^6 electrons per second, can be achieved using broader filters.

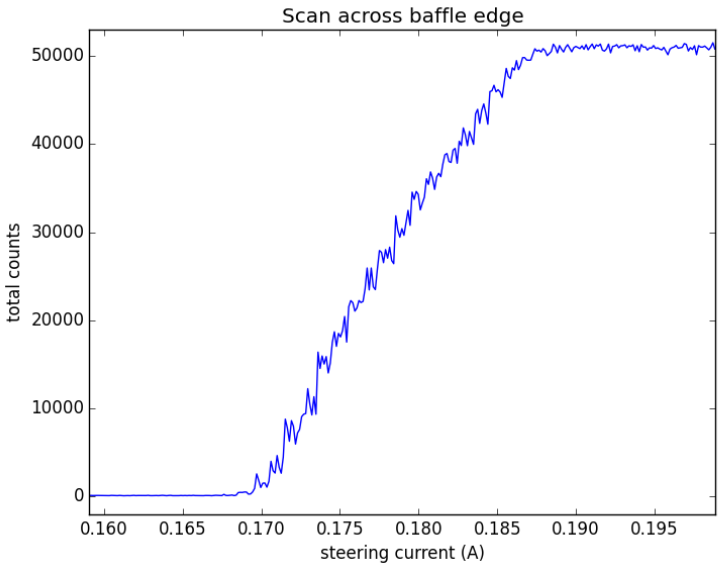

Figure 4.6: Electron count rate as the beam is steered across the edge of a baffle.

Beam Size

The electron beam size can be estimated by steering the electron beam across the edge of a baffle. The baffle is placed in the center of the beam path, and magnetic dipoles are used to steer the beam across the baffle, and then back onto the detector. The width of the response function suggests a beam size of about $140\mu m$.

Angular Selection

We verified the angular selectivity of the electron gun using two methods. The first was to monitor the phase of the beam as we modulate the solenoid magnetic field. This method was only possible at large pitch angle because the technique loses sensitivity at low angles. As seen in figure 4.7, the angular spread means that we get a spread in phase at the detector, so the beam "spot" becomes more of a crescent. The change in the phase as we modulate the magnetic field is due to the fact that the

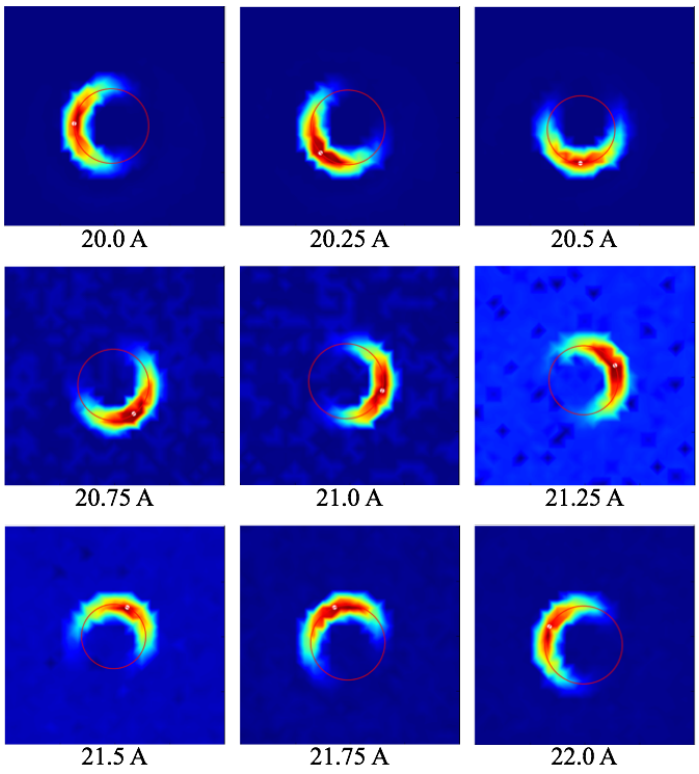

Figure 4.7: Rotation of the electron beam as the magnetic field is modulated.

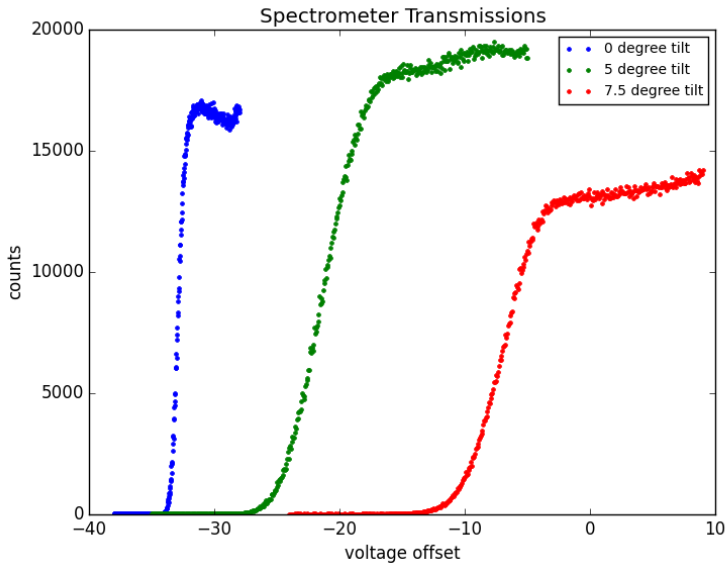

Figure 4.8: Electron transmission functions for three different settings. The beams all contained the same energy, so the shift in the transmission function is due to the change in the pitch angle.

pitch angle of the electron is changed, which also changes the time that the electron takes to get through the beam path. The phase change we see in figure 4.7 suggests a pitch angle of about 20°, which is close to the expected 18°, from simulations.

For lower pitch angles, we estimate the electron pitch angles using the spectrometer. We expect to see a shift in the transmission function when the pitch angle is increased due to the reduction in momentum perpendicular to the retardation plane. In figure 4.8, the voltage shifts in the 5 and 7.5 degree tilted runs indicate pitch angles of 1.7 and 2.9 degrees in the 190 Gauss estimated field at the spectrometer retardation plane. These figures suggest pitch angles in the tritium source of 24 and 45 degrees.

Chapter 5

Electron Scattering from the Rear Wall

5.1 Motivation

The presence of a gold surface at the rear of the KATRIN source is necessary, yet provides a potential complication. This complication is the possibility of electrons backscattered from the rear wall affecting the measurement results. Though these relatively few backscattered electrons are unlikely to appreciably skew the endpoint measurement, we nonetheless thought it worthwhile to explore the issue experimentally, due to possible deficiencies in electron scattering models, or effects from roughness of the gold surface.

In addition, the keV-scale neutrino search that is planned after the conclusion of the standard KATRIN experiment can be similarly affected. Secondary electron sources or backscattered electrons have the possibility of altering the detected spectrum. While it is possible to change the KATRIN rear section following the endpoint

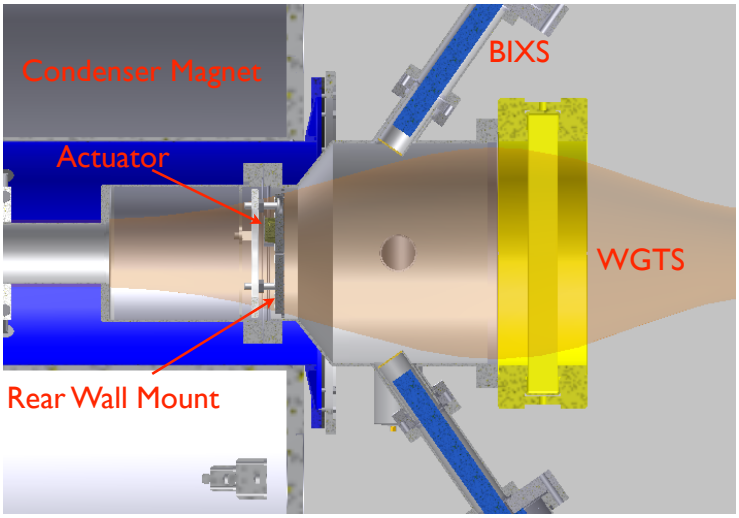

Figure 5.1: A CAD view of the rear wall chamber. The magnetic flux corresponding to the detectable region of the source is indicated.

measurement, it would require long downtime, and is much more involved than the alterations already planned due to the high tritium exposure of materials in the rear section. Therefore, any potential issues pertaining to anything within the rear section for the keV neutrino search must be addressed before closing of the vacuum system.

For systematics relating to the tritium endpoint spectrum, we are primarily concerned with the electron energy loss close to the incident electron energy. For the keV-scale search, however, our interest is in the broad spectrum, including possible mono energetic Auger secondaries.

5.2 Theory

5.2.1 The Endpoint Spectrum

It came as a surprise that there is a relative lack of research into electron backscattering off of materials for energies greater than a few keV. The study of reflection

electron energy loss spectroscopy (REELS) is fairly well studied for use in materials research and surface science[61, 62, 63]. Extensive literature searches did not, however, reveal any sources measuring high resolution (< 10 eV) electron backscatter energy loss spectra with initial electron sources greater than a few keV. Sources using lower initial energies can, nonetheless be instructive.

The endpoint of the spectrum, in theory, should contain energy loss signals from both elastic and inelastic collisions with gold atoms. Elastic collision losses rise due to the recoil energy imparted to the target gold atom, but are too small (a fraction of a volt) to be detectable in this measurement. Inelastic transitions are those that impart energy to electrons and modify their energy states.

The greatest structure of interest in the electron backscatter spectrum at the endpoint is the presence of plasmon peaks. A plasmon is a quantum of charge density oscillation that is commonly found in plasmas or metals with high free electron densities. It is a psuedoparticle and can be thought of conceptually quite like the phonon, which is instead a quantum of mechanical oscillation. Plasmons can be formed in the bulk of a material or can be localized at the surface.

Plasmons, in general, are important factors determining the optical properties of materials, since they are commonly excited by electromagnetic fields. They can, however, also be excited by electron interactions, so we expect to see energy loss peaks at the plasmon energies. For more information see *Baragiola, et al*[64].

A literature search found few sources relating to the energy loss spectrum in gold at the endpoint. One relevant source, Yoshikawa, et al[65], models electron energy loss and shows experimental data from an initial electron beam of 1 keV. In the paper, they report plasmon energy loss peaks of 5.6, 16.5, 25.5 and 33.5 eV.

K $1s$				
80.725				
L_1 $2s$	L_2 $2p_{1/2}$	L_3 $2p_{3/2}$		
14.353	13.734	11.919		
M_1 $3s$	M_2 $3p_{1/2}$	M_3 $3p_{3/2}$	M_4 $3d_{3/2}$	M_5 $3d_{5/2}$
3.425	3.148	2.743	2.291	2.206

Figure 5.2: Binding energies in Gold for the lowest electron shells. All energies in keV.

5.2.2 The Expected Full-Range Spectrum

Much like the literature on electron backscattering, most of the literature regarding Auger electron emission is limited to lines below about 2 keV[66, 67, 68]. There are a few papers detailing backscattering using high energy electrons, but they do not address the issue of energy loss at high resolution[69]. It benefits us, then, to look at electron interactions in matter from a more first principles approach.

We can start our discussion regarding electron backscattering in gold with the gold shell structure. Figure 5.2 shows the binding energies of the deepest energy levels in gold (taken from the x-ray data booklet[8]). At 80 keV, the K level is unreachable, so we will focus on L-shell interactions. When looking at the full spectrum of the backscattered and secondary electrons, there are a few signals of interest that we might see. First, we expect to see core-loss structures at energies around the incident electron energy minus the binding energies of each shell.

The second feature of interest is Auger peaks. The most readily found sources of gold Auger lines only go up to about 2 keV, though there are certainly more. An Auger electron is created following the ejection of an inner-core electron. In our case, this inner core electron will come from the L-shell. A higher level electron can then drop to the empty space, and one of two competing effects can happen. First, the

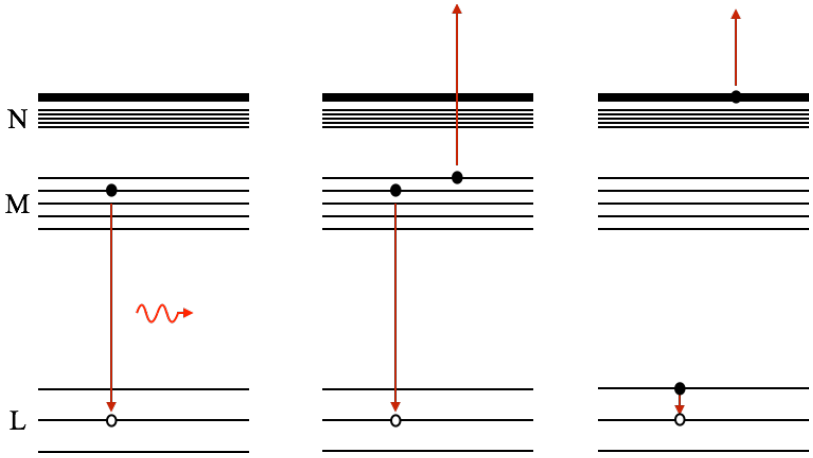

Figure 5.3: Mechanism for production of characteristic X-rays (left), Auger electrons (center), and Coster-Kronig electrons.

$L\alpha_1$	$L\alpha_2$	$L\beta_1$	$L\beta_2$	$L\gamma_1$	$M\alpha_1$
9.71	9.63	11.44	11.58	13.38	2.12

Figure 5.4: Relevant characteristic X-Rays of Gold. Energies in keV.

excess energy of the transition can be emitted in the form of a characteristic X-ray. Second, the excess energy can be transferred to a second higher-lying electron, which is also ejected. Therefore, an Auger electron emission leaves a doubly ionized atom. A related transition, the Coster-Kronig cascade, results when one of the two electrons involved comes from the same shell as the initial vacancy. Coster-Kronig electrons are of lower energy, and won't be explored, but it should be noted that the transition still leaves the system with an inner shell vacancy that can result in further X-ray or Auger transitions. Figure 5.3 summarizes these production mechanisms. For more information, see [70].

Both X-ray and Auger emission start with the same initial state- with an inner shell vacancy. For that reason, these are competing processes. We can define the X-ray fluorescence as the fraction of the time such a vacancy will result in a characteristic X-

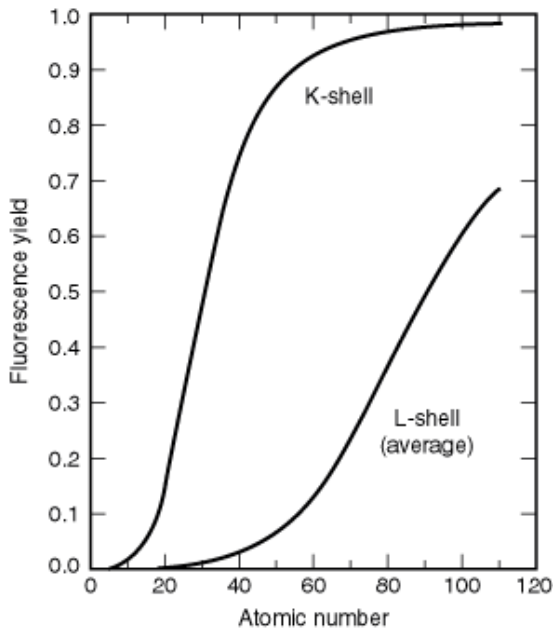

Figure 5.5: Best fit of X-ray fluorescence values as a function of Z. Figure from the X-ray Data Booklet[8].

ray. The rate of Auger plus the Coster-Kronig production is then simply unity minus the X-ray fluorescence. Figure 5.5 shows best fit values of the measured fluorescence from the literature, as a function of Z. At $Z = 79$, gold should have an L-shell fluorescence of about 30%, meaning the majority of L-shell vacancies should result in an Auger electron.

The expected Auger spectrum is significantly more complex than what we see from characteristic X-rays. This is due to the fact that an Auger emission involves movement of electrons from three separate energy levels- the initial vacant inner shell, the electron that falls to the inner shell, and the electron that is emitted. It should be noted that it does not matter which electron ends up in which state, and in fact is not knowable. Therefore, a particular Auger line can be expressed using those three energy levels. If we label the three energy levels {1,2,3} the energy of the Auger

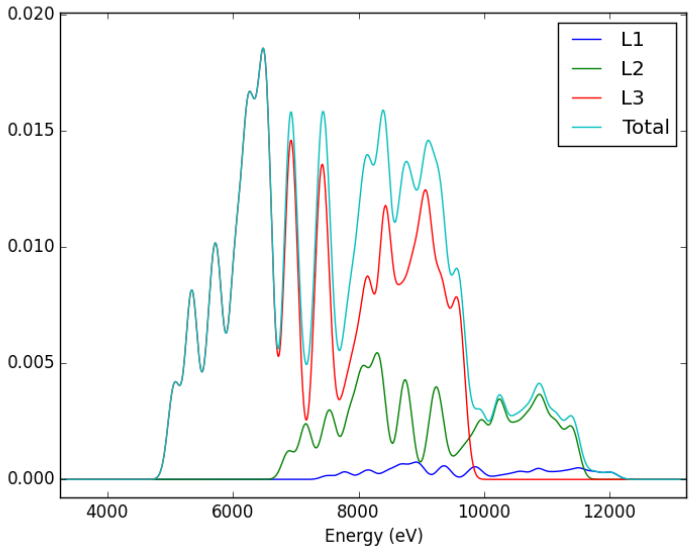

Figure 5.6: A hypothetical gold Auger spectrum.

electron can be written:

$$E_A = E_1 - E_2 - E_3 \tag{5.1}$$

The equation is not strictly correct, because we should, in principle, consider the energy levels in singly-ionized state. However, this correction is small compared to the energy resolution we need for our discussion, and the un-ionized binding energies will suffice.

Figure 5.6 shows a hypothetical Auger spectrum containing the LMM and LMN transitions, which should represent the largest contributors in the measurements to follow. The relative intensities of $L1$, $L2$, and $L3$ peaks are based on electron impact ionization cross sections and Auger yields taken from the literature. Cross section values used were 5×10^{-23}, 1.7×10^{-22}, and 4.2×10^{-22}[71, 72], and Auger yields

were 0.234, 0.503, and 0.693[73] for $L1$, $L2$, and $L3$ respectively. Relative intensities of peaks within each family are assumed to be the same, with the exception that LMN peaks are set to half the peak height of the LMM peaks. The ratio between LMN peaks and LMM peaks was not found in the literature, so the spectrum shown should be considered for illustrative purposes only. Furthermore, the contribution from Coster-Kronig transitions and their secondary interactions was not included.

What we can see, however, is that the number of closely lying L, M, and N states make the resultant spectrum very dense. Most of the individual lines are not distinguishable at moderate energy resolution (set to 100 eV in the figure). Overall, the primary features are the peak around 6, 8-10 keV (resultant from the LMM transitions) and the secondary feature around 11 keV (from LMN transitions).

Of course, we also expect other features to occlude the Auger electron signal. We expect backscattered core-loss electrons to produce structure at energies around the initial energy minus the shell ionization energies. Secondary electrons are mostly limited to energies of a few keV, but will dominate interesting structure in that region.

5.3 Experimental Setup

The surface that is under investigation in this section is a gold coated stainless steel disk of construction identical to the construction that will be used in the final rear wall. The stainless steel disk is electropolished prior to galvanic gold deposition of a few microns. The sample was cleaned using an ultrasonic bath of acetone, followed by isopropanol prior to insertion in the chamber.

To get the best energy resolution possible, we have chosen to use a focusable mono energetic electron beam as the primary electron source. It was most cost-effective to

Figure 5.7: The scanning electron microscope (ISI SS40) used in the electron backscatter experiment.

repurpose an electron beam from a scanning electron microscope for this source. An ISI SS40 SEM was purchased second hand for use in this project. While we retained the use of the SEM control electronics, the chamber and vacuum pump were found to be insufficient for our needs. This was due to the fact that the chamber ports were very small, and evacuating the spectrometer chamber would have taken far too long. Furthermore, we opted to get rid of the included diffusion pump to maintain cleanliness of the chamber.

The primary beam was mounted into a custom chamber of vacuum pressure in the low 10^{-6} torr range and focused on a gold surface. The gold sample was mounted at an angle with the normal held 42 degrees from the incident beam. The choice of 42 degrees, rather than 45, which would provide the highest backscatter rate, was made because light from the electron gun filament could reflect off the gold surface and produced high backgrounds when the sample was mounted at 45 degrees.

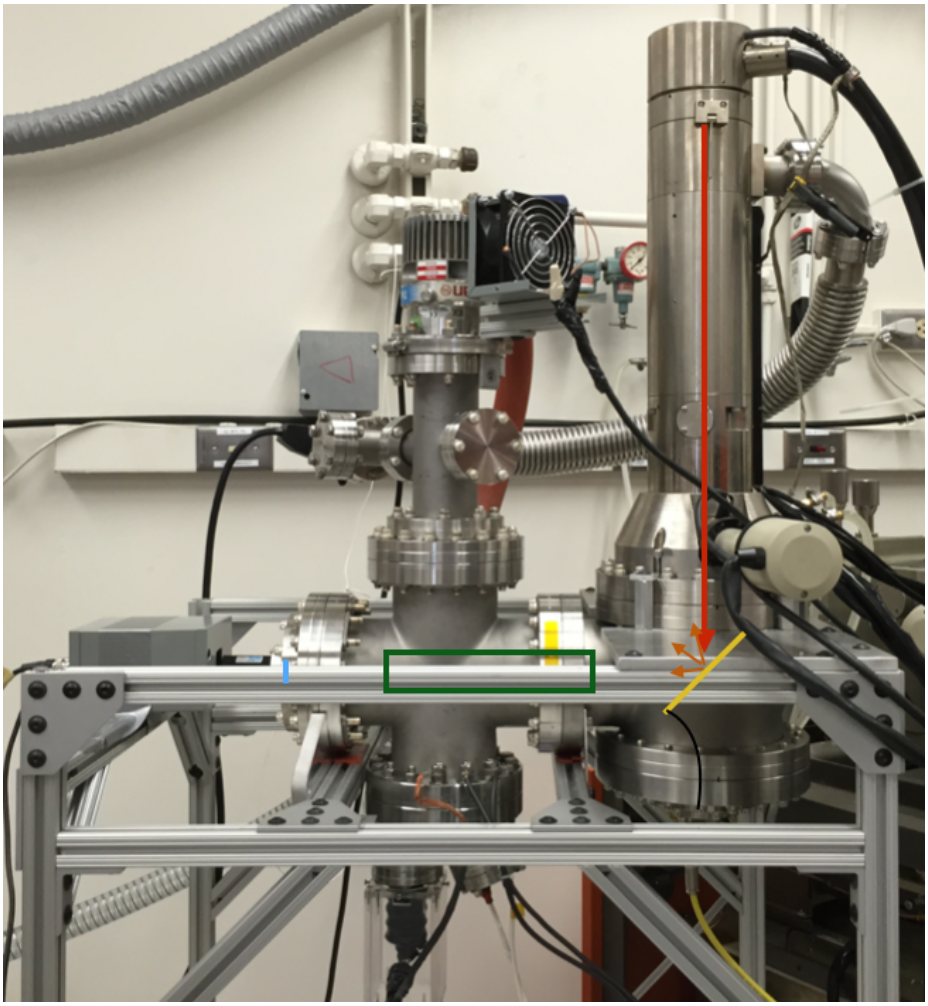

Figure 5.8: The electron backscatter experiment assembly, including custom CF flanged chamber containing the gold sample. The basic locations of each assembly are outlined, including the primary beam path (red), the gold surface (yellow), spectrometer (green), and scintillator (blue).

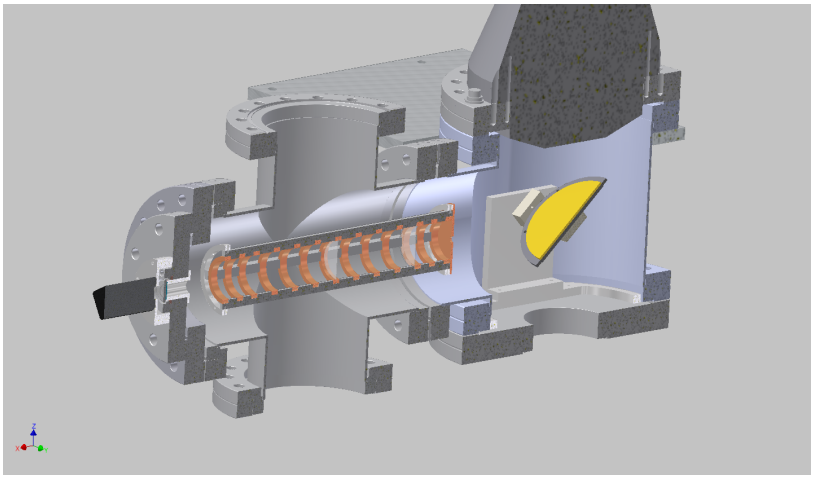

(a) The whole internal layout

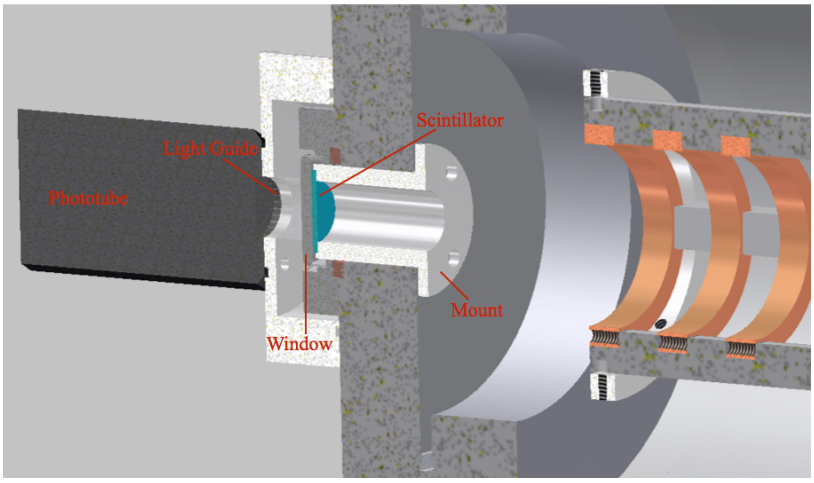

(b) Closeup view of the scintillator and phototube mount

Figure 5.9: Sectioned CAD views of the electron backscatter internals

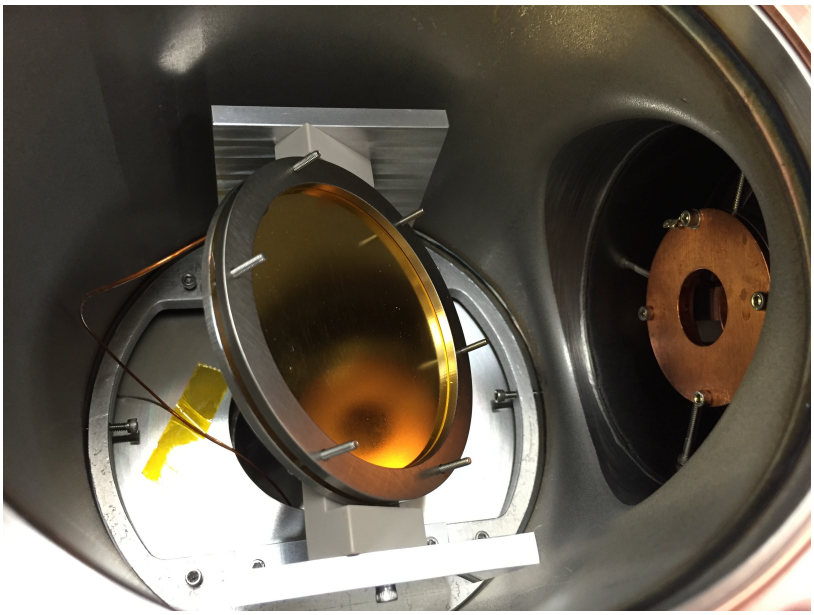

Figure 5.10: A view, before mounting the electron gun column on top, of the gold sample, as mounted in the chamber. The end of the spectrometer can also be seen.

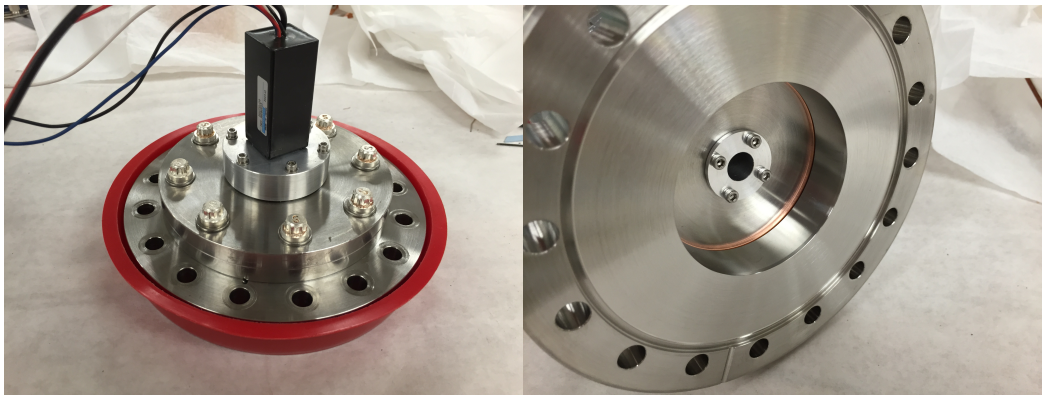

Figure 5.11: The phototube and scintillator mount assemblies

A custom made electrostatic spectrometer (detailed below) was placed with its axis 90 degrees from the primary beam axis and pointed at the center of the gold sample. On the other side of the spectrometer, a P47 scintillator disk was pressed up against the vacuum window, and a Hamamatsu photomultiplier tube was used to detect the scintillation light. A short acrylic cylinder was mounted between the phototube and window and functioned as a light guide. The endpoint tests and full range scans differed only in the spectrometer used. The spectrometer used in endpoint testing was a longer one, designed for energy resolution with an Einzel lens for electron collimation. For full-energy range scans, the problem of electron optics was tackled by using a shorter spectrometer and placing it as close to the detector as possible. More details on the spectrometers are below.

Signals from the phototube were amplified using an Ortec fast filter amplifier, and fed into a CAEN desktop digitizer. A Stanford Research systems -20kV high voltage supply was used to control the retarding potential, while a Glassman -20kV supply controlled the Einzel lens in the spectrometer entrance. A Keithly 487 pico ammeter was attached to the gold sample in order to monitor the stability of the incident beam. All instruments were controlled using custom software, written in Python.

5.3.1 The Spectrometer

The spectrometer was custom-designed and built specifically for this experiment using a stacked-ring design. A resistor chain creates the stepped voltage gradient. A stainless steel mesh with pitch of about a milimeter is held at the retarding potential to provide the maximum uniformity in voltage at the retarding plane, which is critical for energy resolution. The final design of the spectrometer was arrived at from a combination of simulation results, electrostatic discharge considerations, and

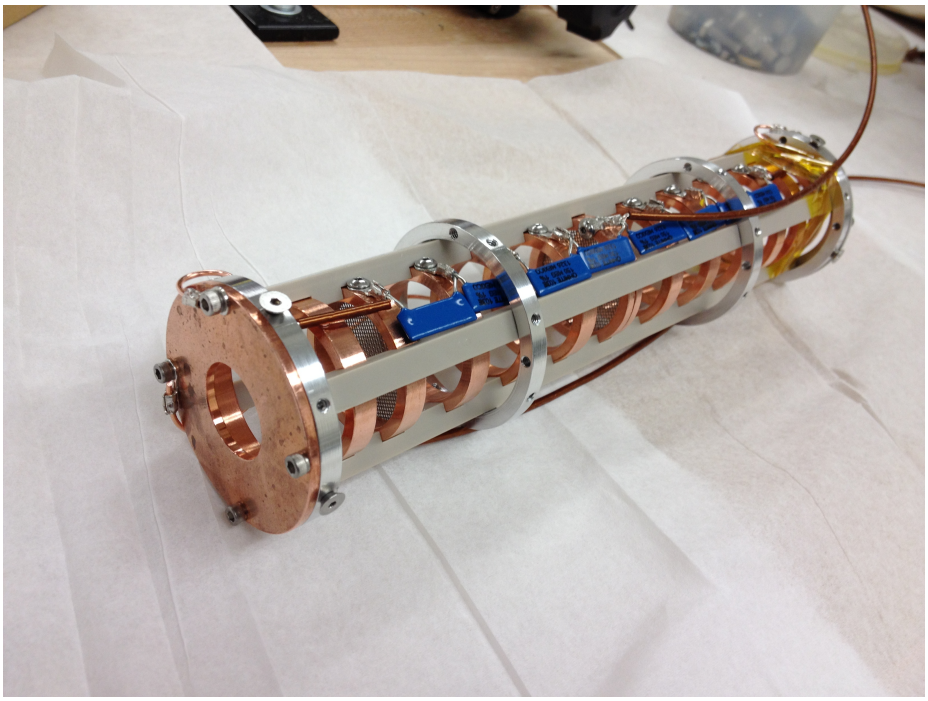

Figure 5.12: The spectrometer used in the electron backscatter endpoint measurement. It is comprised of spaced rings forming an Einzel lens, and followed by a gradual ramp (by use of a resistor chain) to the retardation potential. A mesh is held at the retardation potential for maximum uniformity of potential at the retardation plane.

convenience of mechanical design.

For the sake of energy resolution and signal rate, an Einzel lens was included at the entrance to the spectrometer. An Einzel lens affects electron paths in much the same way that optical lenses affect light. It is produced by placing one ring electrode at high voltage (a few kV), between two grounded electrodes. When tuned optimally, the Einzel lens collimates the electrons, so that they reach the retarding potential normal to the plane of the mesh, and minimizing the width of the transmission function.

For scans of the entire range, electron optics effects made measurements with the main spectrometer infeasible. This was due to the fact that the Einzel lens only

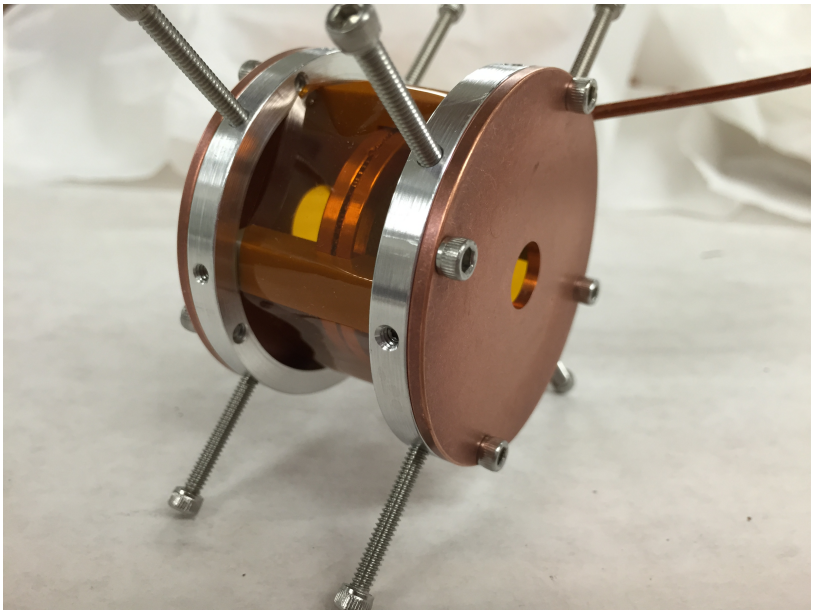

Figure 5.13: The spectrometer used in the full scan measurement. There is simply a mesh sandwiched between two ring electrodes at the retardation potential. The input and output pinholes are grounded.

focuses electrons with a narrow range of energy, and electrons of a wide energy range could not all be sufficiently focused onto the detector. For this reason, a second spectrometer was built, and is shown in figure 5.13. This one consisted of a single ring with a built in mesh, identical to the electrode at the retarding plane used in the full spectrometer. This ring was simply mounted between two disks with pinholes of 3/8" (entry) and 1/2" (exit). The total length of this shortened spectrometer is about 1.5". Optical effects that might change the signal were minimized by placing the spectrometer at the far rear of the chamber, as close to the detector as possible.

Simulations

Electron behavior was explored in simulation using Kassiopeia, an electron tracking software toolkit developed by the KATRIN collaboration. Electric fields are

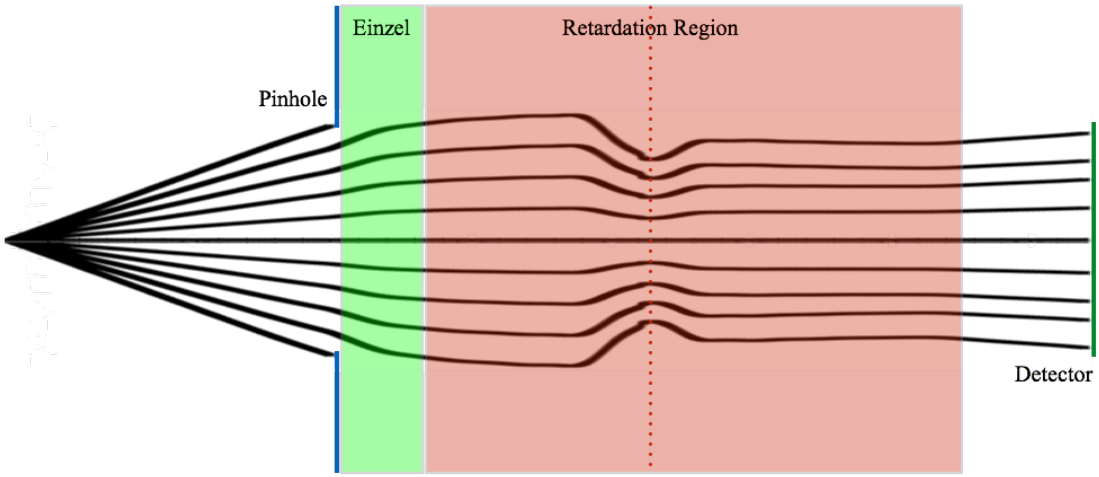

Figure 5.14: Simulated electron tracks through the spectrometer. Colored boxes delineate the different regions of the spectrometer, with the Einzel lens region in green and retardation region in red. Tracks are simulated for 18,002 eV electrons through a field with -18 kV retardation potential and -6 kV Einzel lens.

solved using KEMfield, which incorporates an implementation of the boundary element method. Electron paths are solved using Runga-Kutta method.

Simulations helped with the electromagnetic design of the spectrometer, and verified the intended performance. The basic idea behind the design is to limit the electron optical effects to the Einzel lens region. The Einzel lens electrodes are spaced closer together than the retardation electrodes because simulations showed that closer spacing magnifies the optical effects. Conversely, the number and spacing of the retardation electrodes were selected to use the available vacuum space, while also making resistor mounting as easy as possible. Simulations also informed the decision to include a mesh following the Einzel lens because the reduction of shine-through between the Einzel lens and retardation sections improved the uniformity of the optical response.

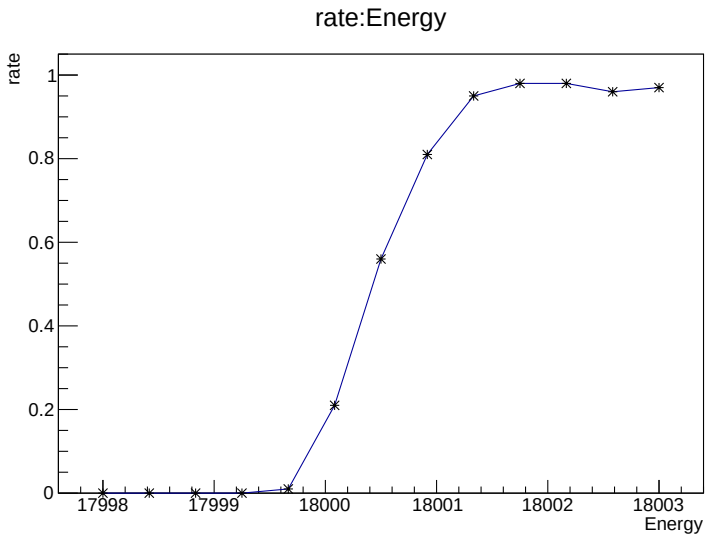

Figure 5.15: Spectrometer transmission function found from simulation, using a -18 kV retardation potential, with -6 kV Einzel lens.

Simulations show that the transmission function of the spectrometer is very good in principle, nearing 1 eV transmission width. The simulations used 100 electrons, distributed isotropically within the opening pinhole of the spectrometer at each energy. It should be noted that we do not expect this performance in practice for two reasons. First, the meshes used at the retardation plane and following the Einzel lens were modeled as continuous plates which were made transparent to electrons. This concession was necessary because it simply was the closest possible method of simulating the potential of the mesh. Because of this, the potential will not be as uniform in practice. Secondly, the simulations assume a point source for electrons, but in reality, the initial electron beam will have some finite area, and the electron paths will be slightly different.

5.4 Experimental Procedure

In the case of full range scans, because there is no Einzel lens, the measurement procedure is relatively simple. Parameters for scan range, measurement time, and number of points are decided, and the voltage is stepped up in strictly increasing fashion. At each voltage, pulses are counted using the CAEN digitizer for the prescribed period of time. The current of the incoming beam was measured at one second intervals to monitor beam stability.

Endpoint scans were performed much the same way, only with the added complication of the Einzel lens. The voltage on the Einzel lens had to be varied with the retarding voltage for two reasons. First, the focusing power of an Einzel lens is energy dependent. Secondly, changing the retardation potential altered the optical effects as well. To get the optimal Einzel lens parameters, a sparse two dimensional scan was first performed over the retardation potential range of interest. At each retardation voltage, an Einzel voltage was found that yielded the highest count rate. It was found that the relationship between the optimal Einzel and retardation voltages was well modeled as a parabolic relationship, and a fit was performed. The fit was then used to continuously vary the Einzel lens voltage as the final scan was performed.

5.5 Analysis and Results

5.5.1 Full-spectrum analysis

Because we measure the spectra in integrative mode, we have to extract the backscatter spectrum by finding the derivative of the measured data. Numerical differentiation of noisy data is a well-known and difficult problem. Figure 5.16 shows

the major steps of the analysis. The critical step is the use of a Savitsky-Golay filter for smoothing.

The first step is to use the current data to eliminate suspect data points. The electron source was found to be sometimes unstable, and any data taken during these bouts of instability need to be accounted for. Luckily, the readings of current from the sample allow us to monitor the electron source. Data points where the variation in current were too high were thrown out, and replaced with a value derived from a linear fit to the surrounding data. Next, a background subtraction is done. In some data runs, field electron emission at the spectrometer resulted in increasing background at high voltage. The background subtraction was done using an exponential fit to the data above the expected spectrum endpoint. This background subtraction did, however, have the effect of washing out the endpoint signal in some cases, so the expected elastic collision peak is not present in high voltage runs.

Finally, the data is smoothed using a Savitsky-Golay filter. In a Savitsky-Golay filter, a polynomial fit is performed within a window surrounding each point, and the point is replaced with the expected value given the fit. Fit parameters can then be used to directly find the derivative at each point, and the variance in the fit parameters used to estimate the uncertainty at each point. The best results were found simply using a linear fit for each point, since the additional terms at higher orders added additional uncertainties to the fits. The polynomial fit window is widened as needed to reduce the uncertainty in the derivative. Widening the window, of course, reduces the effective energy resolution. A χ^2 test then was used to compare the fit residuals to the expected statistical uncertainties.

Figure 5.17 shows the results of runs at 15 keV and 18 keV initial beam energy. It should be noted that this 18 keV spectrum is derived from a data set collected

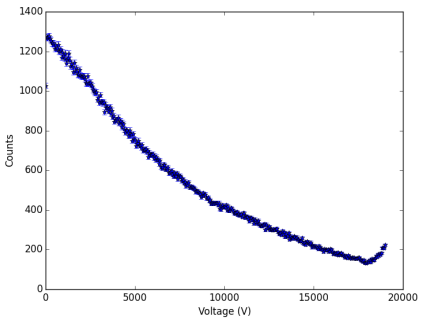

(a) Raw Data

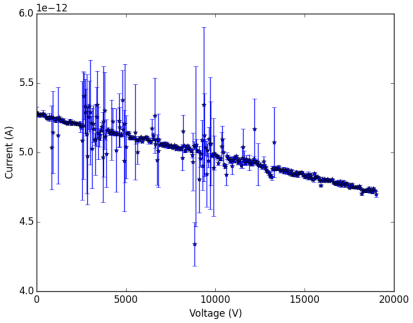

(b) Measured Currents

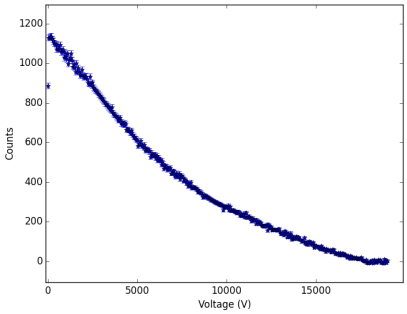

(c) BackGround subtracted, with suspect data points corrected

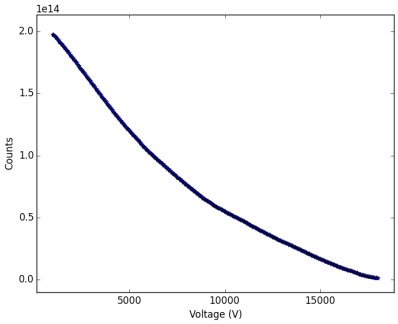

(d) Smoothed

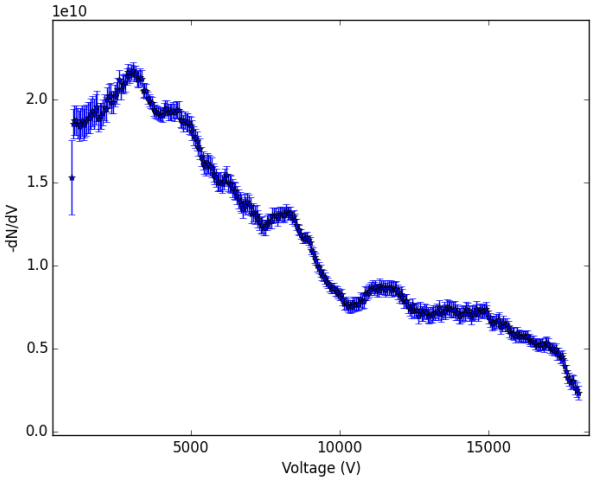

(e) Derivative

Figure 5.16: The steps involved in finding the backscatter spectrum from transmission data with an 18 keV source.

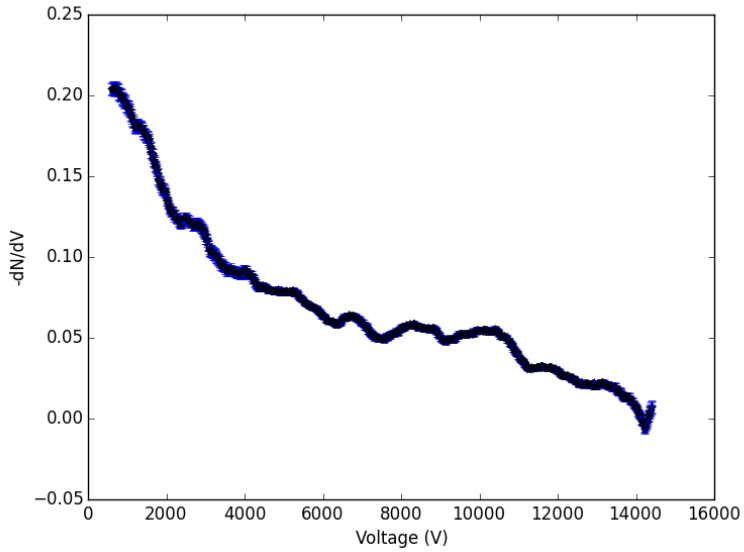

(a) 15 keV source

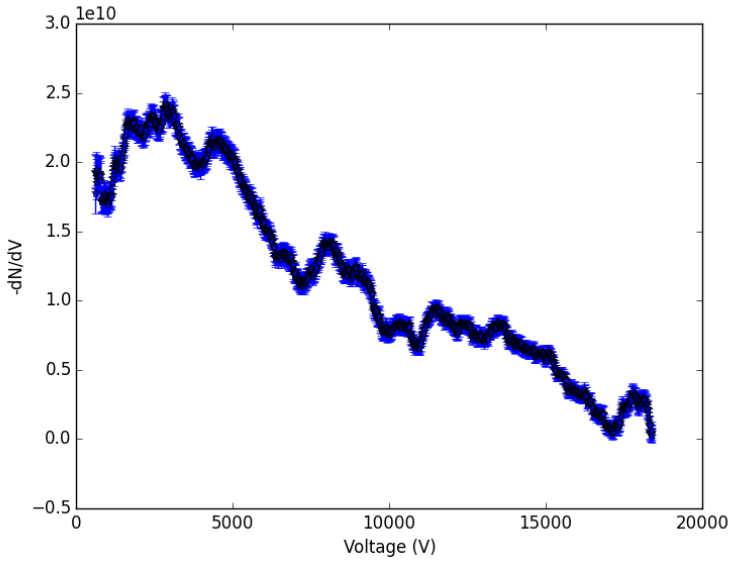

(b) 18 keV source

Figure 5.17: More spectra as derived from the analysis detailed in the text for two different beam energies.

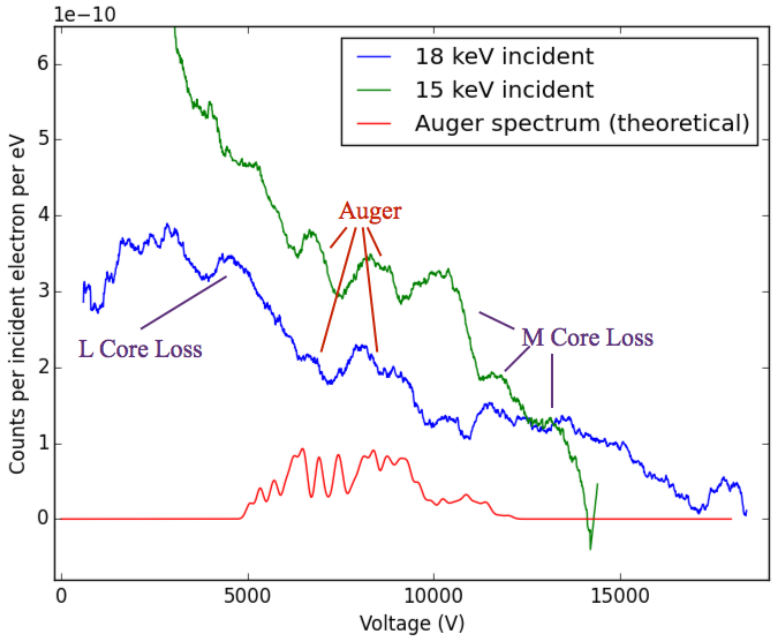

Figure 5.18: The number of counts per eV, per electron measured from 15 keV and 18 keV electron sources.

independently of the data shown in figure 5.16. The two sets contain the same major features, so we are assured that those features are not the result of transient instabilities in the electron source.

From the 15keV and 18keV spectra, we see a few interesting features. First, we see clusters around 6-9kV and 10-11kV, suggesting that we are, indeed, observing the Auger electrons in both cases. In the case of the 18 keV spectra, the L_3 core loss lies at around 6 keV, so is likely occluding the Auger feature we expect there, though we do see an Auger peak, as expected, in the 15 keV spectrum. One puzzling feature in the 15 keV spectrum is the large feature at around 10 keV, which is far too large to be solely due to Auger electrons. One possible explanation is that the extra electrons are due to core loss backscattered electrons from the M shell ionizations.

To get an idea of the rate of Auger emission, refer to figure 5.18. Here, the count rate is normalized to show the count rate per eV, per incident electron, which is estimated based on the current measured from the sample. The current measured from the sample should not be viewed strictly equivalent to the initial beam energy, due to lost counts from backscattered and secondary electrons, so the values derived should only be seen as approximate. Furthermore, it is difficult to make quantitative statements about the spectrum because of how many closely lying features are present and uncertainty surrounding the underlying continuum. However, we can still make some approximate statements.

Concentrating on the 15 keV and 18 keV data surrounding the features in the 8-10 keV region, which should not contain any other known features, we integrate the total counts underneath the features and get about 5×10^{-8} total counts per incident electron. From the geometry of the experimental setup and open area of the spectrometer mesh, this leads us to the conclusion that about 5×10^{-5} of the incident electrons are resulting in an Auger electron in this energy range. Given electron impact cross section for L shell ionization of about 6×10^{-22} cm^2, compared to total cross section of 3×10^{-18} cm^2[72], this fraction of Auger electron production is reasonable.

5.5.2 Endpoint analysis

The best endpoint data was found using an electron beam energy of 10 keV, due to the fact that the electron gun yielded greater electron currents at 10 keV. Figure 5.19 shows the raw data and derivative, as derived from the procedure detailed previously. By flipping around the derivative spectrum and offsetting it to the elastic peak, we get the energy loss spectrum shown in figure 5.20. It should be noted that we do not

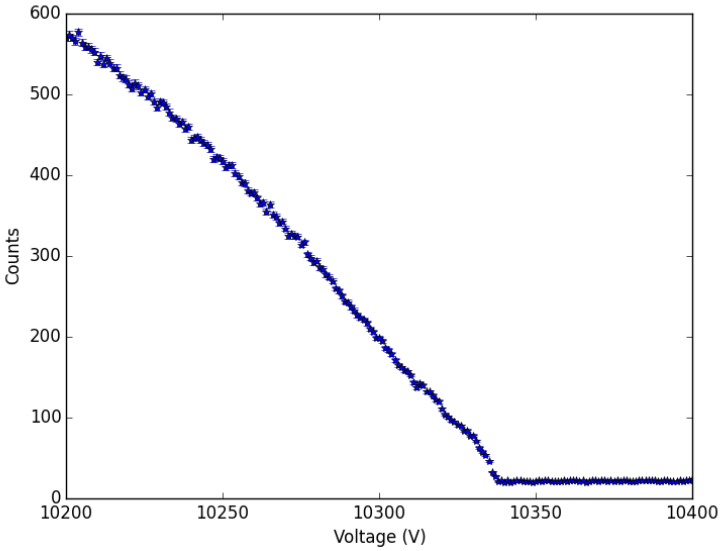

(a) Endpoint raw data

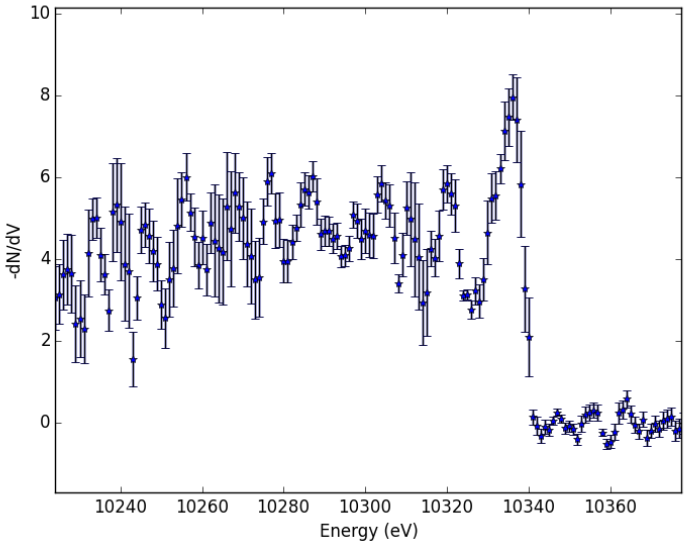

(b) Endpoint derivative

Figure 5.19: The endpoint spectrum, using a 10 keV initial beam.

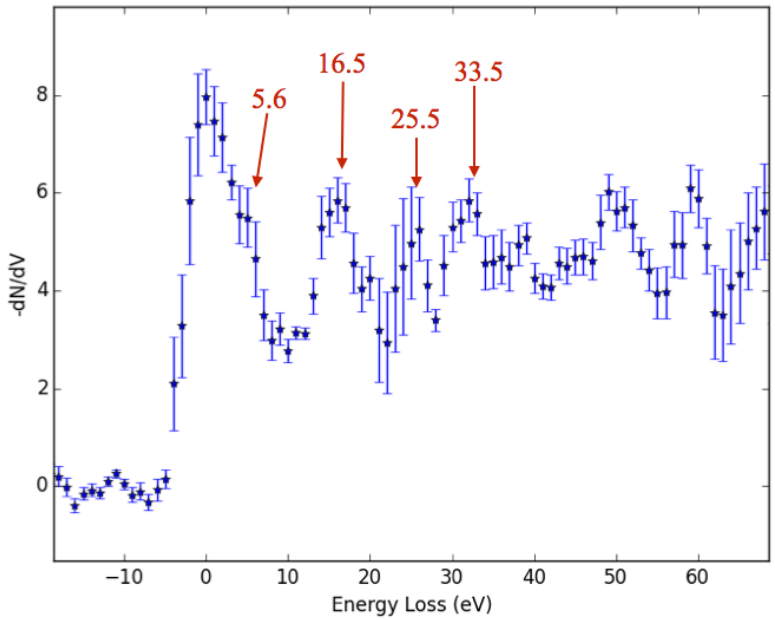

Figure 5.20: The electron energy loss spectrum with notable peaks.

have independent verification of the initial beam energy, so there is an uncertainty in absolute energy of order 1eV. There are several peaks that could be due to plasmon interactions within the gold. The asymmetric shape of the elastic peak suggests another peak nearby, but the energy cannot be precisely defined.

The apparent oscillatory behavior seen beyond the elastic peak has been analyzed, and it has been concluded that it is merely due to statistical variation.

We can compare the measured spectrum to results in the literature. Yoshikawa et al [65] presents experimental data for backscattered electrons from gold from a 1keV beam. They show peaks at energy loss values of 5.6, 16.5, 25.5, and 33.5 eV. Our results are in very good agreement, considering the uncertainty we have in the initial beam energy. Additional peaks we see at 50 and 59 eV could be multiple scattering peaks not normally seen at lower beam energies. The primary difference between our

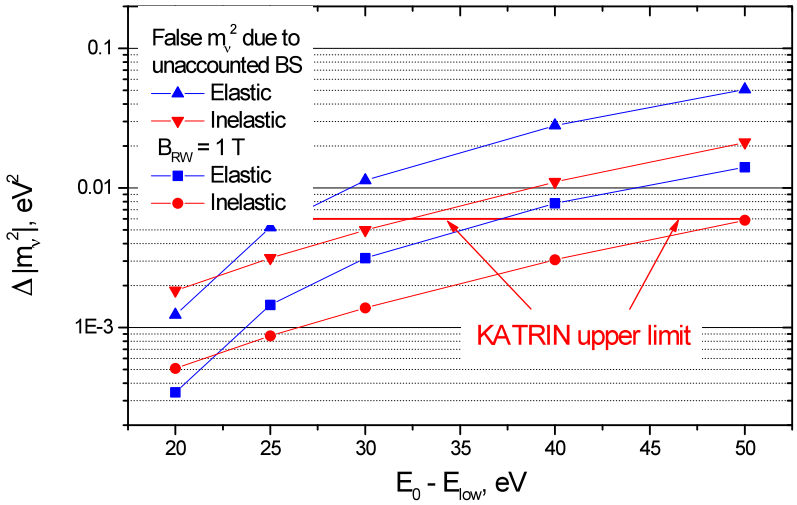

Figure 5.21: The effect on the KATRIN tritium spectrum from backscattered electrons. Results are from Titov and Spalek, from simulations performed in 2008. Shown are results assuming 1 T and 3.6 T magnetic field at the rear wall.

results and those found in the literature is from the relatively small amplitude of the elastic peak, but this is expected from the higher energy of the initial beam.

Simulations have been performed previously by Spalek and Titov (see figure 5.21 for a summary of their results)[74]. Given the agreement between these experimental results and expectations from the literature, we conclude that the results from the simulations previously done are still valid.

Chapter 6

Sterile Neutrino Search Using the KATRIN Experiment

6.1 Motivation

The prospect of a sterile neutrino in the keV-mass scale has long been discussed as a potential dark matter candidate[75]. More recently, the discovery of an unexplained X-ray line at 3.5 keV indicates a possible sterile neutrino of mass 7.1 keV[33]. A 7 keV sterile neutrino, with sufficient production mechanism, could in fact account for the entirety of the dark matter observed within the universe[34, 35]. Finding evidence for such a sterile neutrino would be an exciting development that would change the face of physics. Katrin is well poised to run a direct search for a sterile neutrino of this energy, since a sterile neutrino of that energy range would fall within the middle of the tritium decay spectrum. The high strength of the Katrin tritium source should provide excellent statistics.

6.2 Using KATRIN to Find keV Scale Sterile Neutrinos

As detailed in section 1.5.1, the observed beta energy spectrum from tritium decay is the superposition of spectra stemming from all neutrino species. In the case of the three known neutrino species, the mass splittings are too close to be resolved using the KATRIN experiment, and the three masses can be considered quasi-degenerate. In the case of a keV-scale neutrino, however, this is not the case. Referring to equation 1.11, we can write the combined spectrum in this form:

$$\begin{aligned}\frac{dN}{dK_e} = &\cos^2\theta \left(\frac{dN}{dK_e}\right)_{m_\nu} \Theta(E_0 - E_e - m_\nu) \\ &+ \sin^2\theta \left(\frac{dN}{dK_e}\right)_{m_s} \Theta(E_0 - E_e - m_s)\end{aligned} \tag{6.1}$$

Here, m_ν and m_s refer to the normal quasi-degenerate mass and sterile mass, respectively. Figure 6.1 shows the effect on the tritium decay spectrum expected from the presence of a 7.1 keV sterile neutrino at unrealistically large mixing angle. As is evident from the figure, the presence of a sterile neutrino results in a "kink" in the spectrum.

Due to the high strength of the KATRIN tritium source, it is possible to observe this kink at low sterile neutrino mixing angle, provided that the measured spectrum is well modeled[36]. Figure 6.2 shows the result of a hypothetical measurement divided by the standard tritium spectrum, assuming KATRIN-like statistics. The kink is very clearly seen at mixing angle of $\sin^2\theta = 10^{-7}$. The ability to see this signature relies on the ability to sufficiently model the expected tritium spectrum. Several modifications

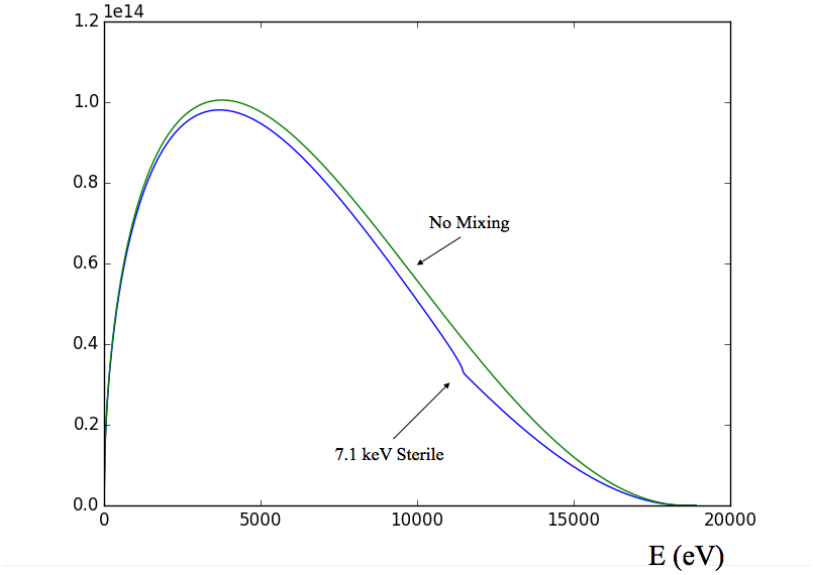

Figure 6.1: Tritium spectrum showing the presence of a 7.1 keV sterile neutrino with a mixing angle of $\sin^2\theta = 0.2$

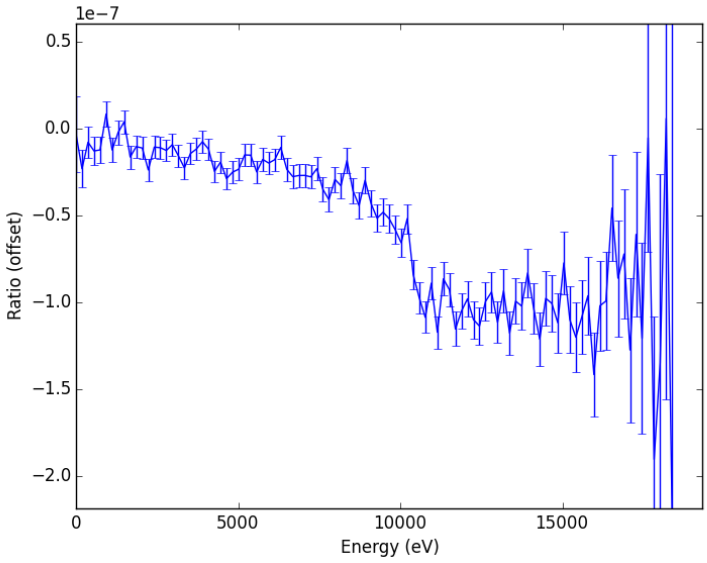

Figure 6.2: The offset ratio between a hypothetical measured spectrum with 8 keV sterile neutrino and a spectrum with no sterile neutrino. Here, the mixing angle is set to $\sin^2\theta = 10^{-7}$, and we assume statistics of $\sim 10^18$ electrons.

to the tritium spectrum have been examined, including nuclear and atomic correction terms, as well as detection effects like limited energy resolution and efficiency. Some modifications to the spectrum, like electron backscattering and collisions within the tritium source still need to be explored.

Because the KATRIN experiment, as it is currently planned, is optimized for endpoint measurement, some modifications will be required in order to perform a sterile neutrino search. In particular, the silicon PIN diode detector is not capable of handling the large signal rates of the KATRIN source away from the endpoint. Upgrades to the detector system are planned for after the endpoint measurement is performed. One goal of these upgrades is to allow for a differential measurement, wherein the main spectrometer is held at a voltage lower than the measurement region, and the detector itself provides sufficient energy resolution to accommodate the measurement.

6.2.1 Sterile Neutrino Search Using Wavelet Analysis

Though many analysis techniques are currently being explored, one method that shows promise is wavelet analysis[37]. Wavelet analysis is encouraging as a tool because it is insensitive to smooth modifications to the tritium decay spectrum that result from many sources of systematic uncertainties.

Wavelet analysis is much like Fourier analysis, but while Fourier analysis provides information in frequency space alone, wavelet analysis provides information in both time and frequency space. A discrete wavelet transformation is implemented as a matrix transformation that yields two sets of data. The first set (labeled x_k) consists of a down-sampled, low-pass filtered copy of the input vector. The second output vector (γ_k) is the time-domain of the high-pass filtered component of the input data.

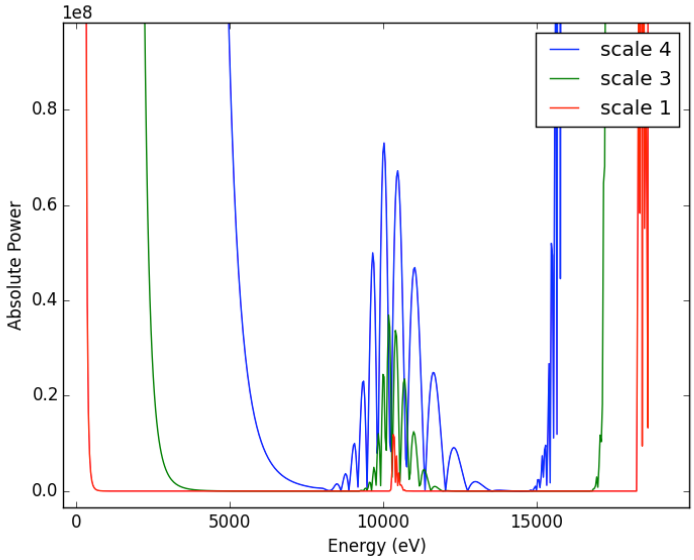

Figure 6.3: The absolute power obtained from a stationary wavelet transform for a sterile neutrino spectrum at $m_s = 8keV$ and $\sin^2\theta = 10^{-5}$. The higher level transforms have higher sensitivity at the expense of energy resolution. Edge effects come into play at the extremes of the spectrum, and limit the applicability of this technique.

The down-sampled low-pass filtered component of the data can then be subjected to further wavelet transformations. Each successive wavelet transformation contains tighter restrictions in frequency space at the expense of precision in the time domain. The details behind the implementation of discrete wavelet transformations are covered in more depth in the literature, and the reader is directed to explore other sources for more information [76].

In the analysis presented here, we use the wavelet *Daubechie 18*, the same as used by *Mertens, et al*, cited above. Though previous work has been done using the standard discrete wavelet transform, the analysis here is done using the stationary wavelet transform, used for its transformation invariant properties. In the stationary wavelet transform, rather than performing each subsequent transform on a sub-sampled set

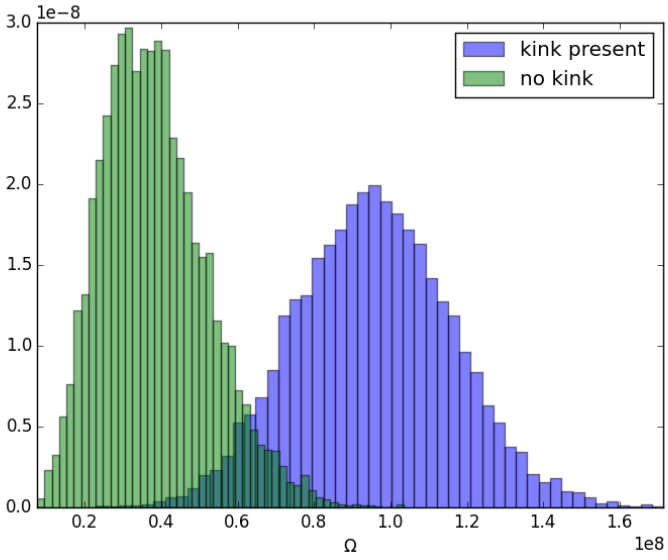

Figure 6.4: Distributions for Ω for sterile neutrino fraction $\sin^2\theta = 4.6 \times 10^{-7}$, compared to a no sterile neutrino case.

of the original data, the sub-sampled set is buffered with zeros to yield a data set of equal length to the original input. The output of the stationary wavelet transform can be seen in figure 6.3. Of note is the fact that edge effects limit the sensitive region of the transform, due to the fact that our input data is not cyclical, and a sharp transition appears at the boundary. It is possible to limit this problem by changing the edge conditions of the input data set through padding it with data that can smooth the transition. These sorts of techniques will not be explored in this work.

We define, as the relevant parameter for kink detection, the parameter Ω, defined according to:

$$\Omega = \sum_{k=E_{kink}-\Delta}^{k=E_{kink}+\Delta} |\gamma_k| \tag{6.2}$$

Here, Δ is set to the value $5 * 2^{s-1}$, where s is the order of the stationary wavelet

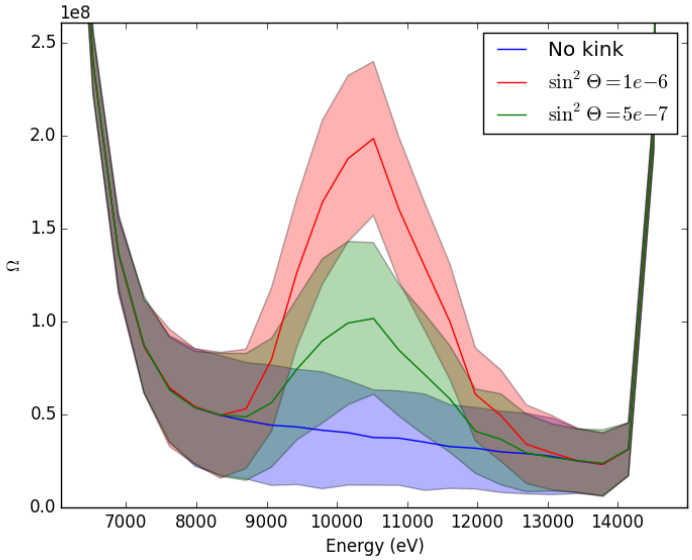

Figure 6.5: The measurement parameter, Ω, as a function of energy, for a fourth order stationary wavelet transform, with an 8 keV sterile neutrino. The colored bands represent 90% confidence levels.

transform. As seen in figure 6.4, which represents results from 10,000 spectra, the presence of a kink can be found to 90% confidence level at $\sin^2\theta = 4.6 \times 10^{-7}$.

Figure 6.5 shows Ω as a function of energy for a spectrum with an 8 keV sterile neutrino. Because this analysis is performed with a fourth order transform, we get the maximum sensitivity to a kink signature, but with low energy resolution. The high order of the transform also limits the energy range of applicability, but once again, this problem can, perhaps, be negated by addition of padding around the boundaries.

To get an idea of the full capabilities of a measurement using KATRIN statistics, refer to figure 6.6. We can see that we should theoretically see the presence of a kink for sterile neutrino contribution of around $\sin^2\theta = 4 \times 10^{-7}$ for most of the central region of the spectrum.

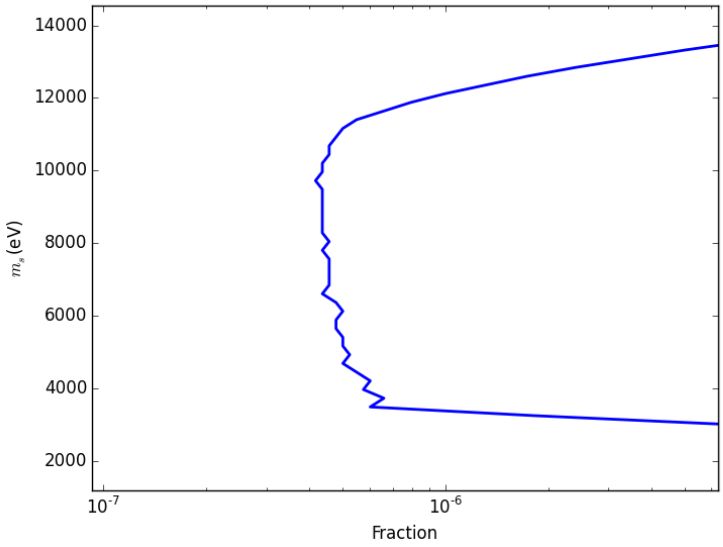

Figure 6.6: The exclusion zone from a sterile neutrino search assuming KATRIN–like statistics, as a function of energy. The line indicates the 90% confidence level.

6.2.2 Possible Systematics

The sensitivity of the wavelet transform is wonderful when it comes to detecting the kink inherent in a sterile neutrino tritium decay spectrum. However, that sensitivity means that we have to watch out for possible false positive signals stemming from other electron sources that can modify the decay spectrum. Previous work has shown that distortions in the spectrum need not harm the measurement as long as the distortions are sufficiently smooth.

Of particular note is the presence of a gold surface at the rear of the tritium source. Backscattered electrons and secondary electrons are expected to come from the rear wall surface as a result of interactions with the tritium source electrons. It should be noted that the gold surface is not required for the sterile neutrino search for physics reasons. Once again, the gold surface was chosen for its work function

uniformity and tritium adsorption properties. These issues are not as important to the sterile neutrino search, which does not have the same energy resolution requirements. However, the rear wall is located in a region of extremely high tritium exposure and safety regulations may not allow for its replacement following the initial tritium mass measurement. Also, it is not clear whether or not there is a suitable material that would not have the same issues. Possible solutions to the following issues are presented further down.

Backscattered electrons

Backscattered electrons from the gold surface or other surfaces within the beam path can alter the measured tritium spectrum. At first glance, this does not look to be a problem because the energy loss spectrum is continuous and slow changing and only shows up in convolution with the tritium spectrum itself. However, the presence of core-loss peaks within the energy loss spectrum might create kink-like signatures that are measurable via wavelet transform. Here, we construct a worst-case scenario by adding electrons with a monoenergetic energy loss function.

Figure 6.7 shows a hypothetical spectrum with added backscattered electrons from a single core loss line at 8 keV. The spectrum does not have quite the "kink"-like appearance of the sterile neutrino spectrum, so we might expect that the wavelet analysis does not pick up the backscatter effect as well. Results confirm this suspicion, as a backscatter rate of 10^{-4} was necessary for detection at the 90% level. This high requirement, coupled with the fact that the simulated spectrum here only represented an extreme worst-case scenario, indicates that backscattered electrons will not be an issue.

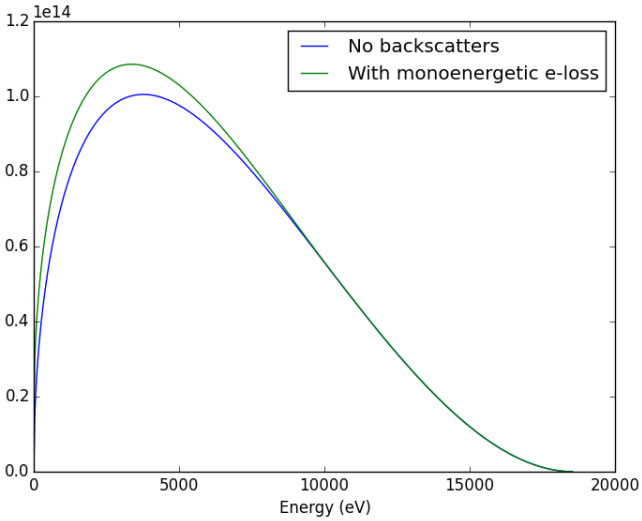

Figure 6.7: Tritium spectrum with added backscattered electrons from a core-loss peak of 8 keV.

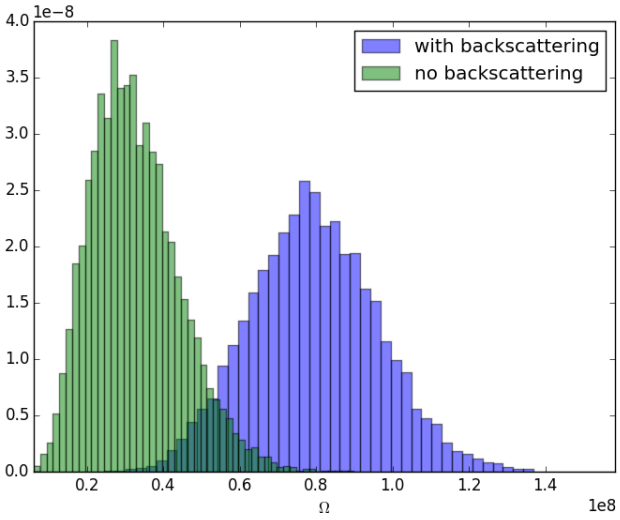

Figure 6.8: Results of 10,000 hypothetical measurements containing 5.3×10^{14} core-loss electrons.

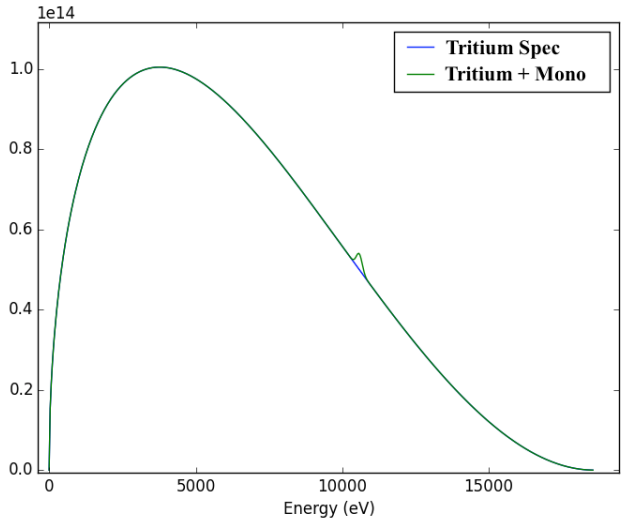

Figure 6.9: Tritium spectrum with a single Auger source at 10.5 keV.

Mono-energetic Electron Sources

One possible alteration to the tritium spectrum is the presence of mono-energetic sources. Possible sources of mono-energetic electrons is radioactive sources within the detection region or Auger electron production. Figure 6.9 shows an example spectrum with a mono-energetic source at 10.5 keV. The possibility of Auger electron production is troubling because they produce sharp distortions.

The analysis from section 6.2.1 was repeated, this time on spectra that included a single mono-energetic source with a standard Gaussian distribution. Figure 6.10 shows the result from a spectrum containing a mono-energetic source at 10.5 keV with standard deviation of 100 eV, which can represent a combination of inherent spread of the electron source and detector energy resolution. A total of 1.1×10^9 electrons was detectable at the 90% level. This number of electrons has to be compared to the total assumed signal source of 10^{18} electrons. Assuming that the electrons are

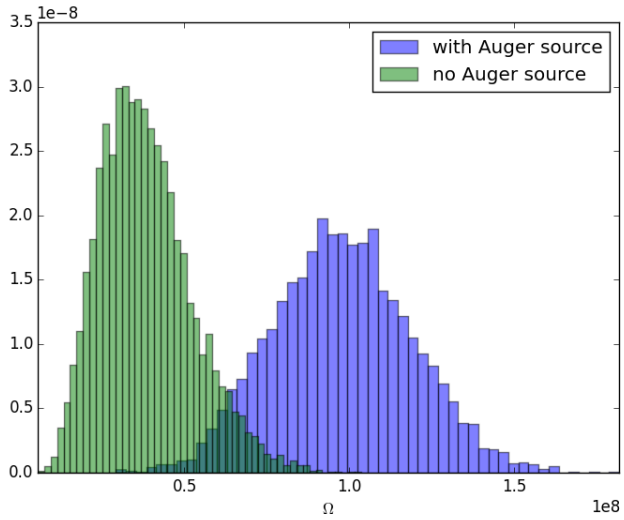

Figure 6.10: Results of 10,000 hypothetical measurements containing a mono-energetic source of 1.1×10^9 electrons.

Auger electrons, only source electrons above a certain energy can result in an Auger emission. We can estimate that ∼10% of source electrons are of sufficient energy, so we have to worry if about 10^{-8} of those electrons result in an Auger emission in the proper energy range.

From figure 6.11, we see that the dependence of Ω with energy also has a shape similar to that found in a spectrum with a kink signature. Overall, though wavelet transformation may be insensitive to systematics that result in smooth changes to the tritium spectrum, sharp modifications like mono-energetic electrons can still pose a problem.

Of course, we don't expect to see just one monoenergetic source, and in the case of Auger electrons from the gold surface, there might be many closely lying energy lines. Figure 6.12 shows Ω as a function of energy if we include a total of about 7×10^{10} electrons comprising the spectrum in figure 5.6. We see that the biggest

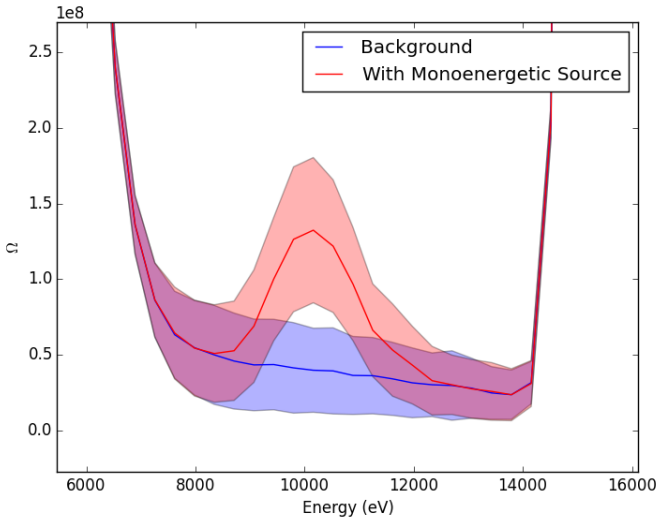

Figure 6.11: Ω as a function of energy for a spectrum with mono-energetic electron source.

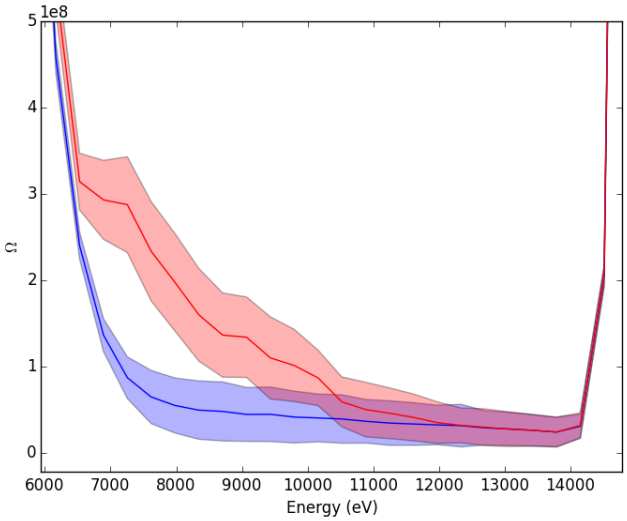

Figure 6.12: Ω as a function of energy assuming an Auger spectrum like the one in figure 5.6

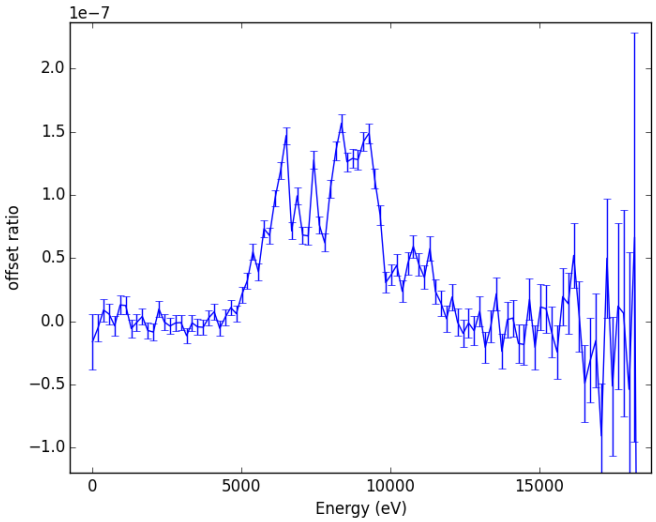

Figure 6.13: The offset ratio between a spectrum with a theoretical Auger source with the normal tritium spectrum, assuming KATRIN statistics.

problem might be the occlusion of any kink signature. To get a frame of reference, from our measurements in chapter 5, we expect roughly 10^{-4} Auger electrons per incident electron. With about 10^{17} electrons of sufficient energy, we expect 10^{13} Auger electrons coming from the gold surface. It seems that we need to find a way to reduce the number of these electrons by several orders of magnitude.

From figure 6.14, we see just how low the Auger electron rate will have to be to avoid false positives. As little as 10^{-8} Auger electrons per primary tritium electron is enough, at certain energies, to result in an apparent kink signature.

To mitigate this problem, perhaps the shape of the spectrum near the apparent kink can be used to differentiate between the two cases. From figure 6.13, we see that the shape of the spectrum with an Auger electron source is vastly different from the case with a kink signature. However, once again, using this analysis method assumes that one has a good model for the measured tritium spectrum. Multiple sources clus-

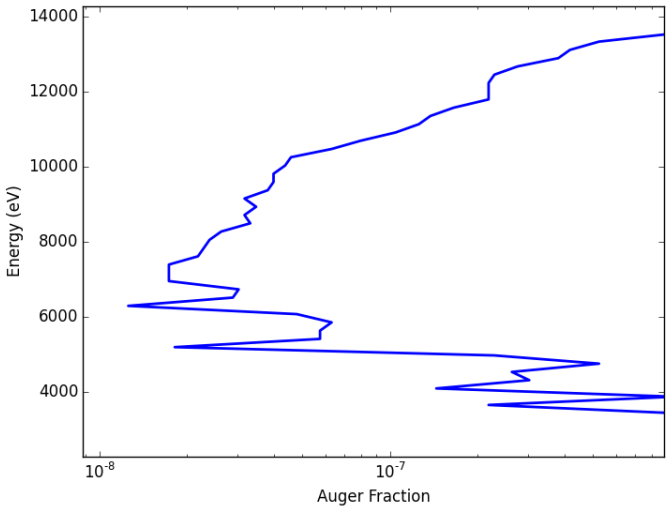

Figure 6.14: The limit of detection, assuming KATRIN statistics, of the presence of Auger electrons, as a function of search energy. Units of the x-axis are the total number of Auger electrons, as a fraction of the number of tritium electrons. The line indicates the 90% confidence level.

tered together, like with a hypothetical gold auger spectrum, may make the analysis difficult or impossible in the region of the possible sterile neutrino signature.

The other possibility to deal with auger electron problems is to reduce the number of auger electrons that make it to the detector. This could be done by reducing the magnetic field at the rear of the tritium source to force the Auger electrons backwards due to the magnetic bottle effect. This can be done due to the fact that the work function uniformity of the gold surface is not essential to the sterile neutrino measurement, since energy resolution, and hence work function uniformity, are not as important. For example, reducing the field to 100 Gauss would reduce the number of electrons by a factor of three. However, the geometry at the opening of the rear section may not make this low field possible (see figure 5.1 for a view of the geometry in the rear wall chamber). By reducing the magnetic field, the magnetic flux would

intersect other components of the rear section (mostly stainless steel), and even more Auger lines would have to be accounted for.

Another alternative is to increase the tritium pressure in the rear of the source by reducing the pumping capacity. This can only be done if it can be established that the rear system can handle the higher tritium levels, and if the transport and pumping sections are still sufficient to reduce vacuum levels in the main spectrometer. However, raising the tritium pressure makes it less likely that electrons originating from the rear wall surface can make it through the source without multiple collisions smearing out and occluding the Auger energies. The kink-like signature of a sterile neutrino would be less occluded because those electrons originate from throughout the tritium source and do not, on average, traverse through the same column density.

Chapter 7

Outlook

Neutrinos have proved to be a fascinating area of research in the recent past and promises to continue to be in the foreseeable future. When we look at the landscape that is the modern field of particle physics, projects involving accelerators and particle colliders like the LHC are generally the first that comes to mind to both the scientific community and the public at large. However, there is, perhaps, an equal or greater chance for new discovery coming from the study of neutrinos.

There still remains much to learn about the neutrino, and what we learn in the coming years will undoubtedly shape the course of discovery to follow. The neutrino, after all, was once thought to be a simple, massless, weakly interacting particle with no particular properties of note. The discovery of neutrino oscillation has brought complexity to this particle, and the discoveries have not seemed to stop there. The possibility of sterile neutrino states introduces exciting possibilities that have consequences in our understanding of the underlying field theories and cosmology.

The mass of the neutrino is a major missing piece of our understanding of neutrinos. Knowledge of the absolute mass scale is a critical piece in our determination

of the nature of the neutrino, as well as the neutrino's role in cosmological evolution. Measuring the neutrino mass, or at least improving our limits on it, is of utmost importance, and the KATRIN experiment will play a critical role.

Going forward, many questions will remain. We will look to neutrinoless double beta decay experiments like MAJORANA or GERDA to answer the question of the nature of the neutrino- whether it is Majorana or Dirac. Oscillation experiments using reactor and accelerator neutrinos will have to provide more evidence for or against the possibility of sterile neutrinos. Or perhaps neutrino mass measurements like KATRIN or Project 8 will eventually confirm or deny that possibility.

Overall, it seems that the study of neutrinos is still just beginning.

Appendix A

The Halftone Method

A.1 Introduction

Countless experimental measurements require the use of tightly constrained electric potentials. In principle, for any potential satisfying the Laplace equation, it is possible to create that potential within a volume by constraining the potential along the boundary of the volume. There are two primary methods currently used to create these fields. First, one can start with electrodes of easily machined shape and use several electrodes on different defined voltages to get an approximation of the target potential. This method has the weakness of requiring several voltages, with either separate voltage sources or resistor chains to define them for sufficient voltage accuracy. The second method is to specially machine electrodes to match equipotential surfaces of the target field, meaning that fewer voltages are required, but the machining cost is much higher.

As an example, we examine the design of quadrupole electric fields, which have uses in many applications in ion trapping and optics[77, 78, 79]. An ideal quadrupole

field is generated using hyperbolic electrodes, but are generally created using cylindrical electrodes instead. The use of cylindrical electrodes creates problems including lower mass resolution and odd features in typical mass spectra[80, 81], though are typically dealt with by using additional "compensation" electrodes that diminish unwanted higher order terms of the potential. Though possible to produce[82], hyperbolic electrodes are costly. We hope that the halftone method can provide a third technique which can be beneficial in many applications.

A.2 Halftone method

A.2.1 Conceptual overview

In the halftone method, we assume that we have a few voltage sources, with as little as two. The halftone method also has the advantage of using very simple geometries. For example, halftone designs can be accomplished using pieces of printed circuit board, or PCB. The potential is defined by patterning of electrodes across the surface. Although we have as little as two applied voltages, continuous definition of the target potential is achieved by regulating the *proportions* of each potential within a certain region. This technique requires that electrodes are placed in close proximity, potentially with sharp edges. For this reason, electrodes have to be designed with close attention to the competing demands of potential accuracy and flashover risk.

A.3 Defining Segmented Boundary Conditions

We focus the following discussion on rectangular volumes composed of planar electrodes. The extension to cylindrical or other geometries is fairly trivial. Although

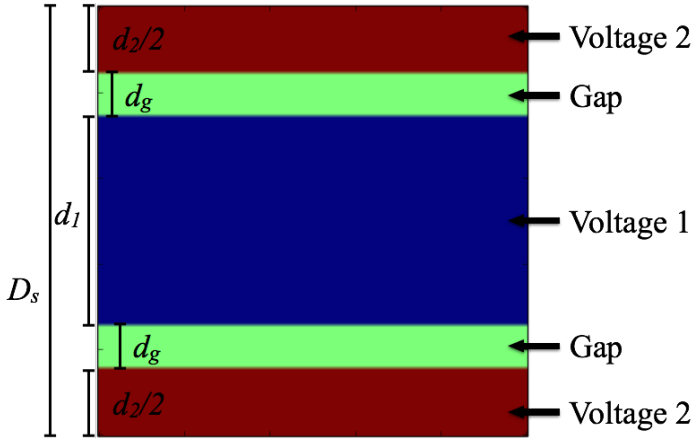

Figure A.1: Example segment showing potential pattern. The red and blue represent two different voltages, with the gaps in green.

we have chosen to draw electrodes with a high degree of symmetry, no such symmetry is *required* for the halftoning technique to work.

The PC board patterns used here are generated based on a simple algorithm. The aim is to create an electrode pattern that will replicate our target potential, $V(x, y, z)$. Each face of our box is divided into strips, which are individually patterned according to figure A.1. Two voltages (red and blue) are divided by gaps (in green) of prescribed thickness. We assume the use of two voltages, V_1 and V_2, segment width D_s, gap width d_g, and widths d_1 and d_2 (refer to figure). The pattern is repeated over the entire surface such that the voltages at the top and bottom (in red in the figure) are continuous with the electrodes above and below. In calculating the average voltage, we assume the potential within the gaps are the arithmetic average of V_1 and V_2. The average potential is calculated as (after eliminating d_2):

$$V_{eff} = V_2 + \frac{(V_1 - V_2)(d_1 + d_g)}{D_s} \tag{A.1}$$

The width, d_1, is varied along the length of the strip according to the intended

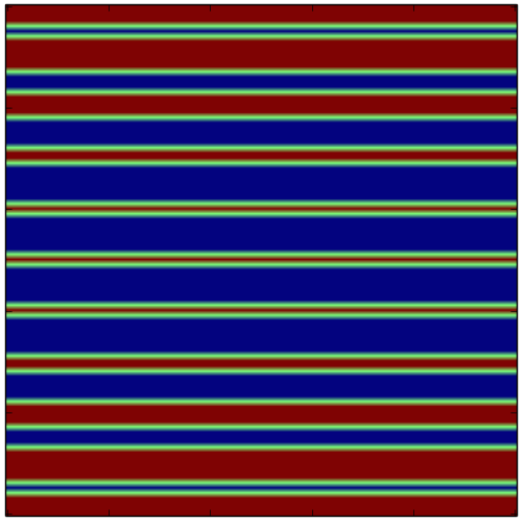

Figure A.2: An example pattern for a whole face in a quadrupole design.

potential distribution. The target field is sampled and the width of the strips varied based on a balance between target field accuracy and computation time. Solving for d_1, and setting V_{eff} to the average of the target field over the segment ($\widetilde{V}$), we get:

$$d_1 = \frac{\widetilde{V} - V_2}{V_1 - V_2} D_s - d_g \tag{A.2}$$

Figure A.2 shows what the voltage pattern looks like for a whole face. The generated pattern shown is of one of four faces used to create a quadrupole field. Because a quadrupole field is invariant along one axis, the generated pattern is very simple.

More complex patterns can be explored, like the one shown in figure A.3. Rather than specify purely rectangular geometries, the electrode thicknesses can be varied continuously along the length of the strip to match the target potential. Voltage patterns are not limited to just two voltages, and do not need any particular symmetries to function as intended. Discretization algorithms are still being developed in order to minimize sharp angles and prevent electrical shorts while minimizing distortion of

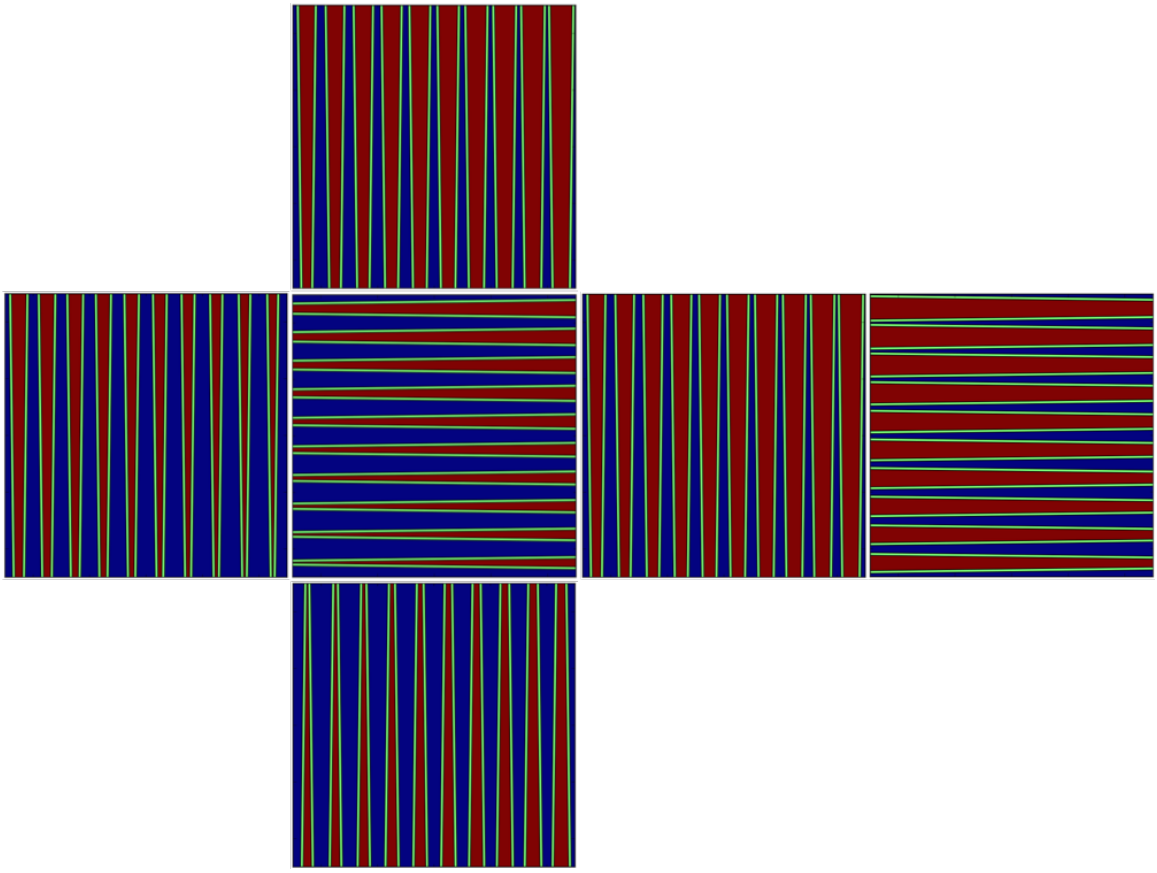

Figure A.3: A more complex pattern, showing all six faces in exploded view. This pattern was generated to produce a potential of the form: $\Phi(x, y, z) \propto x + y + z$.

the field.

The chief difficulty in defining these discretized boundary conditions is coping with required gaps between voltages. From equation A.1, we can see that the gaps limit the effective voltage of each segment. For example, if we define $V_1 = 100\ V$, $V_2 = 0\ V$, and $d_g = D_s/10$, we can only continuously adjust the effective voltage per segment within the range $10V - 90V$. This restriction creates distortions in the field when the effective voltages along the boundary cannot be accurately reproduced.

The issue can be avoided by changing the applied voltages to values beyond the intended potential range. In the previous example, if the range $0V - 100V$ is necessary, one can choose voltages $V_1 = 115\ V$, and $V_2 = -15\ V$. Choices of applied voltage and gap distance must be made, of course, with careful consideration given to the risk of flashover.

A.4 Potential Calculation Using Fourier Expansion

Though other calculation methods were explored, including the Boundary Element Method, we have chosen to perform electric potential calculations by direct solution of the Laplace equation. The reason for this is two-fold. First, by limiting ourselves to rectangular geometries (which are easily constructed from PC board), the Laplacian solution is greatly simplified, and the flexibility inherent in BEM is no longer necessary. Second, the direct solution helps in aiding our understanding of these fields.

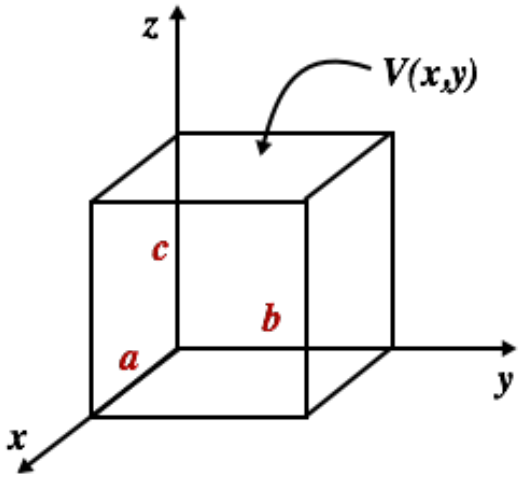

Figure A.4: Geometry used for Laplace equation calculation

A.4.1 Solutions to the Laplace Equation in Rectangular Geometries

Solutions to the Laplacian in rectangular coordinates is covered in many basic E&M textbooks. We will follow the calculation detailed in Jackson's *Classical Electrodynamics*[83]. Examining a rectangular box with dimensions a, b, and c, we look at the case where the potential is zero at all faces except the one at $z = c$, which has an applied condition $V(x, y)$ (see figure A.4). The general solution for this boundary condition is:

$$\Phi(x, y, z) = \sum_{n,m=1}^{\infty} A_{nm}\ sin(\alpha_n x)\ sin(\beta_m y)\ sinh(\gamma_{nm} z) \tag{A.3}$$

With constants α_n, β_m, γ_{nm},

$$\begin{aligned} \alpha_n &= \frac{n\pi}{a} \\ \beta_m &= \frac{m\pi}{b} \\ \gamma_{nm} &= \pi\sqrt{\frac{n^2}{a^2} + \frac{m^2}{b^2}} \end{aligned} \tag{A.4}$$

and coefficients, A_{nm} given by,

$$A_{nm} = \frac{4}{ab\ sinh(\gamma_{nm}c)} \int_0^a dx \int_0^b dy\ V(x,y)\ sin(\alpha_n x)\ sin(\beta_m y) \tag{A.5}$$

For the case where all six faces have defined boundary conditions, the potential is the sum of contributions from all faces, each calculated in this way.

In our case, $V(x, y)$ is defined through a series of polygons of varying shape but constant potential. For a single polygon, D, with contour C, the integral inside equation A.5 can be calculated using Green's theorem:

$$\iint_D \left(\frac{\partial Q}{\partial x} - \frac{\partial P}{\partial y}\right) = \oint_C P dx + Q dy \tag{A.6}$$

We have some flexibility in choice of P and Q, for example, we can use the following:

$$\begin{aligned} Q &= -\frac{1}{\alpha_n}\cos(\alpha_n x)\sin(\beta_m y) \\ P &= 0 \end{aligned} \tag{A.7}$$

The coefficients can then be calculated using the following, where C_i and V_i rep-

resent the contour and voltage applied to each polygonal electrode:

$$A_{nm} = -\frac{4}{ab\ \alpha_n \sinh(\gamma_{nm}c)} \sum_i V_i \oint_{C_i} \cos(\alpha_n x) \sin(\beta_m y) d\vec{r} \tag{A.8}$$

Equation A.8 can be broken down further by splitting up the line integral into those of the individual line segments that make up each electrode. The solution to the line integral along a straight line can be found analytically, but the solution is long and uninteresting and it will be left up to the readers to work out themselves. It is important to note, however, that time-consuming techniques like numerical quadrature are not needed to calculate the expansion terms.

A.4.2 Estimation of Uncertainty Due to Fourier Expansion

We must find some way of estimating the uncertainty in the calculation due to the finite number of terms we can use in the Fourier expansion. The boundary conditions we use contain very sharp transitions, and many of the features on the boundaries only appear in high order terms. However, these high order terms have increasingly small effect on the potential away from the boundary.

Combining equations A.3 and A.5, we can extract the multiplicative term $sinh(\gamma_{nm}z)/sinh(\gamma_{nm}c)$. For large values of γ_{nm}, this term becomes vanishingly small for all regions away from the boundaries. Thus, when focusing our attention away from the edges of our geometry, only a relatively small number of terms is necessary.

To explore this effect, let's define a function, ϕ_{nm}, which represents each term of the Fourier expansion, evaluated at $z = c$. We write ϕ_{nm} as:

$$\phi_{nm}(x, y) = A_{nm}\ sin(\alpha_n x)\ sin(\beta_m y)\ sinh(\gamma_{nm}c) \tag{A.9}$$

This allows us to rewrite equation A.3 in this suggestive manner:

$$\Phi(x,y,z) = \sum_{n,m=1}^{\infty} \phi_{nm}(x,y)\frac{sinh(\gamma_{nm}z)}{sinh(\gamma_{nm}c)} \tag{A.10}$$

In other words, each term of the expansion evaluated at (x, y, z) is merely the corresponding term evaluated at (x, y, c) and reduced by the factor $sinh(\gamma_{nm}z)/sinh(\gamma_{nm}c)$, which ranges from 0 to 1 for all z inside the box.

Now, suppose we've calculated coefficients up to A_{NM}, with N and M finite positive integers. We can then define the function $E_b(x, y)$ which represents the difference between the calculated potential, evaluated at the boundary, and the actual boundary condition.

$$E_b(x,y) = V(x,y) - \sum_{n=1}^{N}\sum_{m=1}^{M} \phi_{nm}(x,y) \tag{A.11}$$

This error is the sum of all terms with $n > N$ or $m > M$. We can get a conservative estimate of the error away from the boundary by propagating E_b through the box according to $sinh(\gamma_{nm}z)/sinh(\gamma_{nm}c)$, where (n, m) is either $(N + 1, 1)$ or $(1, M + 1)$, one of which represents the largest term that has not been included within the calculation.

$$\begin{aligned} E_1(x,y,z) &= E_b(x,y)\frac{sinh(\gamma_{N+1,1}z)}{sinh(\gamma_{N+1,1}c)} \\ E_2(x,y,z) &= E_b(x,y)\frac{sinh(\gamma_{1,M+1}z)}{sinh(\gamma_{1,M+1}c)} \end{aligned} \tag{A.12}$$

The greater of E_1 and E_2 represents our uncertainty estimation. While it is not a strict mathematical upper bound of the error, it generally provides an overestimate

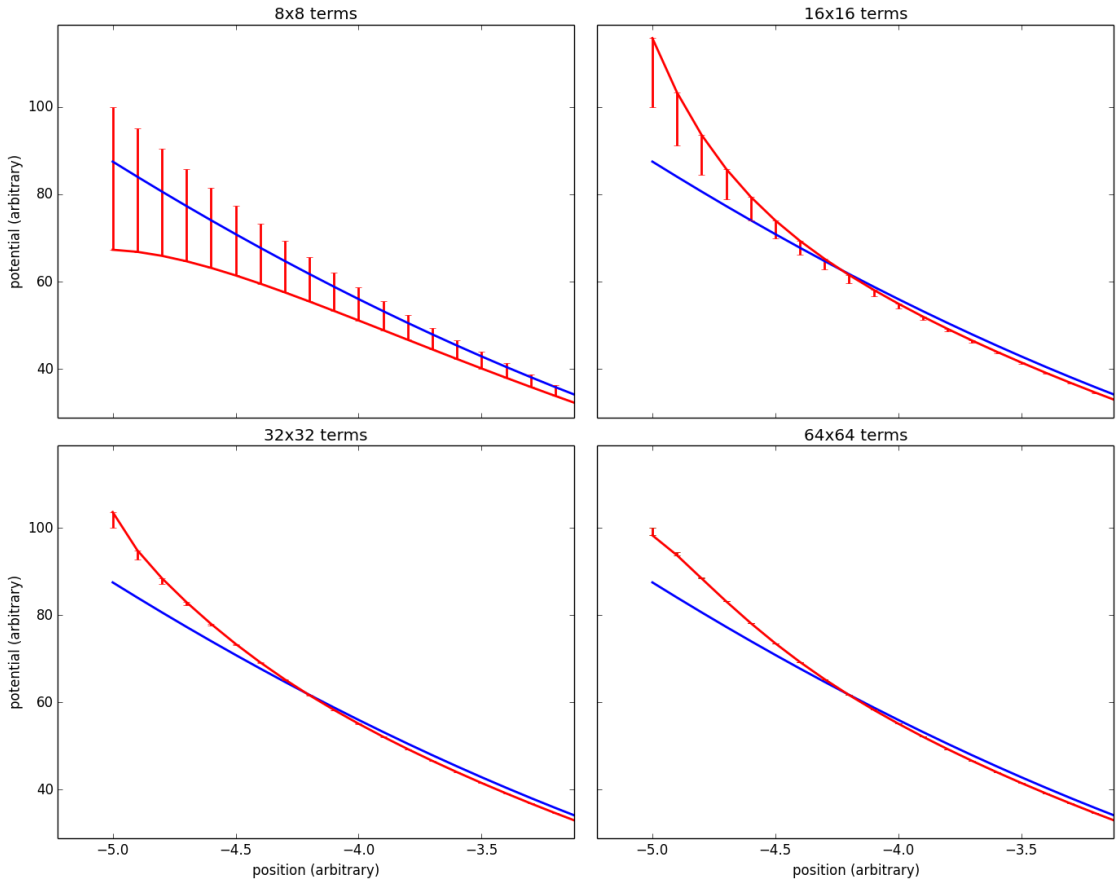

Figure A.5: Calculation of Potential (red), with error bars showing derived uncertainties. Each plot shows the calculation using different numbers of terms. In this geometry, the boundary is at x = -5. The target potential is also shown in each plot in blue.

of the uncertainty.

We can see that adding terms reduces the uncertainty in two ways. First, it generally reduces the error, E_b, at the boundary. Second, the higher order of the terms causes the $sinh(\gamma_{nm}z)/sinh(\gamma_{nm}c)$ term to drop off much faster.

Figure A.5 shows an example of a potential calculated using different numbers of terms. In this example, as little as 16x16 terms is enough to conclusively show deviation from the target field far from the boundary (deviations close to the boundary

are expected in our case). The uncertainty estimation shows that this deviation is a result of an imperfect boundary specification, and not due to an insufficient number of terms applied to the Fourier expansion.

A.5 Electrode design examples

A.5.1 Paul Trap

Here we produce a quadrupole field using this technique and explore the expected performance of such a device. The quadrupole field was chosen for ease of calculation, and also because of its use in many applications including ion storage, electron and ion optics, and mass spectrometry. Although this example happens to have a high degree of symmetry, it is by no means necessary for the halftone technique to work.

An ideal quadrupole field can be expressed mathematically in the form:

$$\Phi(x, y) = \frac{\phi_0}{r_0}(x^2 - y^2) \tag{A.13}$$

Two versions of the quadrupole field were generated to show variability in accuracy with respect to the level of discretization and gap size. Both had dimensions 10mm x 10mm x 20mm (the long dimension along the z-axis). The first used segment widths (D_s) of 1mm and gap widths (d_g) of 0.1mm, while the second had values of 2mm and 0.2mm, respectively (we'll be referring to these fields as field 1 and 2 from now on). One face of the field 1 design is shown back in figure A.2. Maps evaluated at the $z = 0$ plane are shown in figure A.6. The calculations were performed using $64 * 64 = 4096$ terms for each face. The calculations, of course, are valid for any geometry that has the same relative proportions.

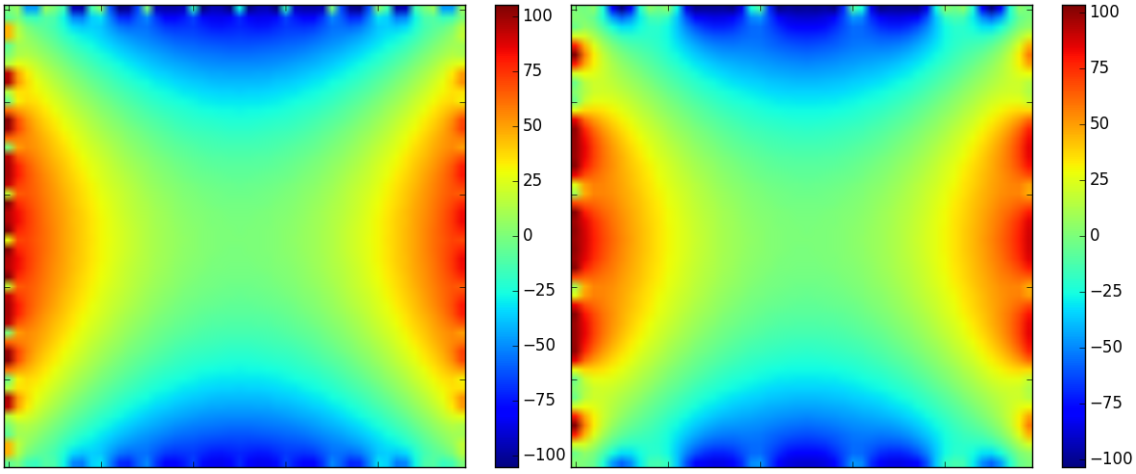

Figure A.6: Calculated potentials for two electrode patterns, as explained in the text

Figure A.7 gives some representation of the accuracy of the generated field with respect to the target field. The results show the effect of varying the discretization and the gap widths in the pattern. Though these two factors are not independently explored here, further studies have shown that increasing either reduces the accuracy of the field.

Another way to analyze these fields is through multipole expansion. The solution to the Laplace equation in two-dimensional polar coordinates can be written in the form:

$$\Phi(r,\theta) = \sum_{m=1}^{\infty} C_m (r/r_0)^m cos(m\theta) + \sum_{n=1}^{\infty} S_n (r/r_0)^n sin(n\theta) \tag{A.14}$$

The constants, C_m and S_n are calculated:

$$C_m = \frac{1}{\pi} \int_{-\pi}^{\pi} V(r_0,\theta) cos(m\theta) d\theta \tag{A.15}$$

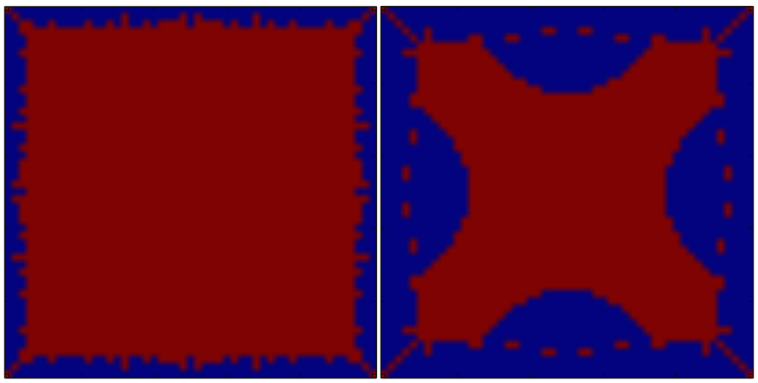

(a) Field 1, 1% (b) Field 1, 0.1%

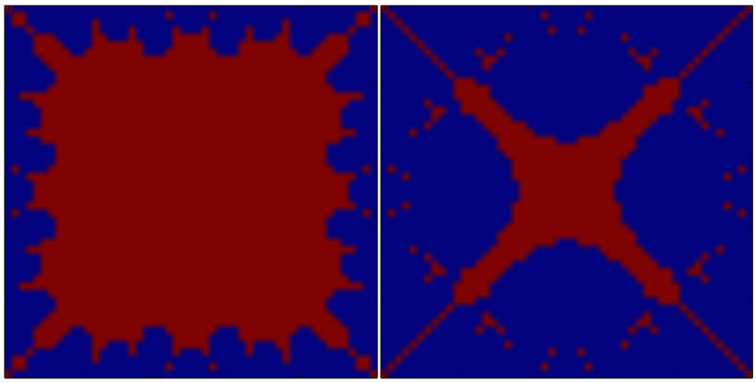

(c) Field 2, 1% (d) Field 2, 0.1%

Figure A.7: Maps for generated fields showing regions (in red) where the fields are within some percentage of the total potential range compared to the target field.

	C_6/C_2	C_{10}/C_2	C_{14}/C_2	C_{18}/C_2
PCB electrodes				
Field 1	3.04e-4	8.40e-8	-6.73e-7	6.15e-8
Field 2	1.59e-3	-9.56e-4	-3.80e-4	-3.05e-5
Cylindrical electrodes				
$r = 1.14511 * r_i$	2.48e-5	-4.20e-5	-7.37e-7	9.18e-7
$r = 1.12 * r_i$	2.41e-4	-4.23e-5	-2.71e-7	6.24e-7

Figure A.8: The first four terms after the quadrupole, present in both generated fields, and two sample cylindrical electrode configurations. The terms are calculated for two sample radii.

$$S_n = \frac{1}{\pi} \int_{-\pi}^{\pi} V(r_0, \theta) sin(n\theta) d\theta \tag{A.16}$$

For symmetry reasons, all S_n terms are zero, and the only non-zero C_m terms are those that satisfy the condition $m = 2(2k + 1)$, where k is an integer. The largest contribution comes from the C_2 term, which represents the quadrupole contribution. In an ideal field, all other terms are zero.

For comparison, we've simulated the field generated from cylindrical electrodes using the Boundary Element Method. There is some variation within the industry when it comes to the diameter and spacing of the electrodes. We've simulated two possible configurations. It has been shown that the hexapole term can be eliminated through selecting diameter, r, vs inscribed radius, r_i such that $r = 1.14511 * r_i$. Another study, however, using simulations of ion trajectories, showed that better mass discrimination can be obtained with diameters satisfying $r = (1.12 - 1.13) * r_i$[84, 85].

Figure A.8 shows the first four terms after the quadrupole for each field, normalized to the quadrupole term. Once again, we see that field 1, having more discretization, has better performance. For comparison, we also show the same values for two

simulated cylindrical quadrupole designs, using the configurations $r = 1.14511 * r_i$, and $r = 1.12 * r_i$. The presence of the C_6 term in the first cylindrical configuration is probably due to a combination of BEM method discretization approximation and imperfect specification in the geometry.

In either case, field 1 is at least on par with the cylindrical electrode configurations, with field 2 once again suffering due to the large electrode size and wide gaps. Of course, we cannot just use the multipole expansion alone to ascertain filter performance. More in depth investigation using ion tracking is needed to determine the relative performance of these filters.

It is also important to note that cylindrical electrode configurations generally have a much smaller active trapping area relative to the overall .

Example Application: Mass Filter

The motion of ions in a quadrupole field is a well known problem and the formalism is described in a number of sources. For now, we begin with some results shown in *Syms, et al*[86]. First, the relationship between the peak of the AC voltage applied, ion mass, frequency, and inner radius of the quadrupole, for optimum trapping:

$$V = 14.46 * 10^{-8}\ m\ f^2\ r_0^2 \tag{A.17}$$

Here, m is in atomic mass units, f in Hz, and r_0 in meters. Next, because we are interested in the uncertainty in mass, we have the following relation:

$$\Delta m = 3.854 * 10^9\ V_z / f^2 L^2 \tag{A.18}$$

Here, V_z is the axial ion energy in eV, and L is the length of the trap. Assuming

we can freely alter the frequency to match the desired filtering, we can eliminate f^2 and get the following formula for the fractional uncertainty in mass filtering:

$$\frac{\Delta m}{m} = \frac{557.3\ V_z r_0^2}{V L^2} \tag{A.19}$$

The fields that were generated and shown in the previous section had values $r_0 = 5mm$, and $V = 200V$. Assuming a reasonable value for axial energy $V_z = 2eV$, and a typical length 10cm, we get a fractional resolution $\Delta m/m = 0.014$. So, for example, at $m \approx 100\ u$, this filter would have just over 1 u resolution. Of course, the resolution can be improved at will by increasing the length of the filter, but increased length will also increase the risk of surface flashover, and may need to be avoided.

The obvious drawback of this technique is the limited voltage range. This problem, of course, is alleviated if we find other ways to increase the allowable voltage. Another possible solution involves the fact that, (looking at equation A.19) the uncertainty has a linear dependence on voltage, but a squared dependence on the dimensions of the trap. We can improve the resolution of the trap by making it as small as possible. For example, values $r_0 = 500\mu m$ and $L = 4cm$ can get to $1u$ resolution with just $10V$ across the gaps. Such small dimensions would require gap widths of a few microns, and the fabrication becomes more complicated. Fairly simple contact lithography is capable of this precision, but the cost is higher compared to normal PCB fabrication, and mounting of the patterns would be very difficult.

A.5.2 Penning Trap

Penning traps are also commonly used in ion mass spectroscopy and other applications. An ideal Penning trap has a potential field of the form:

$$\Phi = \frac{V_0}{4d^2}(2z^2 - x^2 - y^2) \tag{A.20}$$

In this case, d is a characteristic distance of the trap, and V_0 is the voltage applied to the electrodes. In the case of high precision ion mass spectroscopy, this field is generated using carefully constructed hyperboloid-shaped electrodes that are both difficult and costly to construct. An alternative, cheaper method uses cylindrical electrodes with additional "compensation" voltages for better definition of the potential field[87]. The halftone method can, perhaps, produce an approximation of the performance of these devices at a fraction of the cost.

Fields were generated for the patterns shown in figure A.9. The box dimensions were set to 5cm along each axis, with electrode pitch of 2mm, and gaps of half a millimeter. The two voltages applied were 0V and 100V. The generated field can be seen in figure A.10, with accuracy represented in figure A.11.

To further explore the real-world performance of this electrode arrangement, we will use the formalism described by Bollen, et al[88]. We can express the field along the z axis as a polynomial series thusly:

$$V(z) = \frac{V_0}{2}\left(C_0 + \frac{C_2}{z_0^2}z^2 + \frac{C_4}{z_0^4}z^4 + \frac{C_6}{z_0^6}z^6 + \cdots\right) \tag{A.21}$$

Here, V_0 represents the applied voltage, and z_0 is half the length of the trap, along the z axis. The constant component of the field, C_0, has no effect on particle motion, and can be ignored. Because of z-axis symmetry, only even terms contribute. Terms

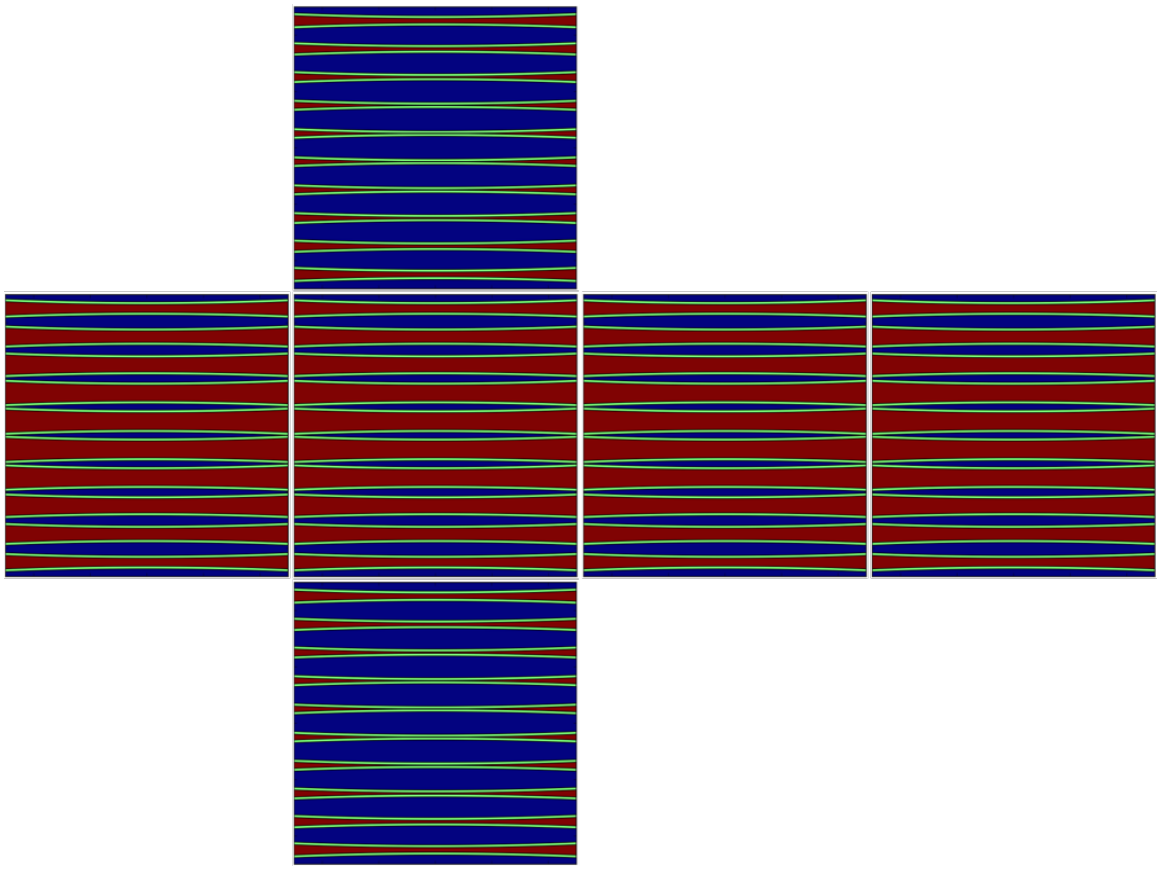

Figure A.9: The generated pattern, showing all six faces, used in making a halftone penning trap.

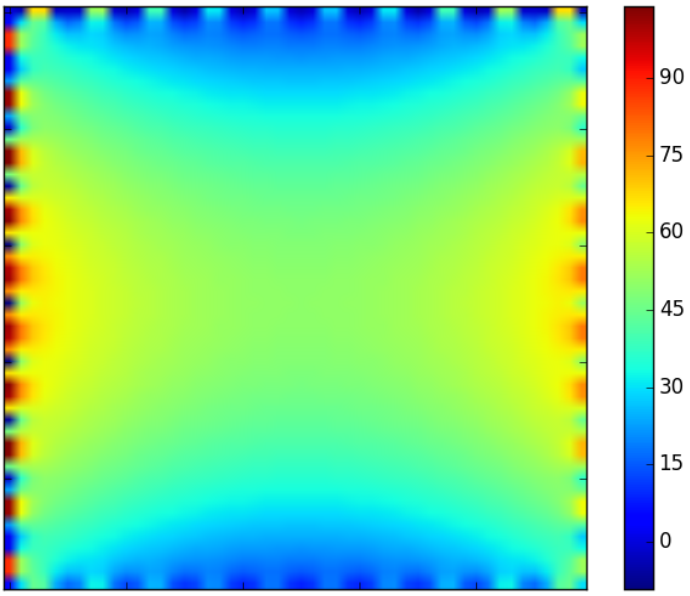

Figure A.10: Field at the $x = 0$ plane generated by the penning trap pattern.

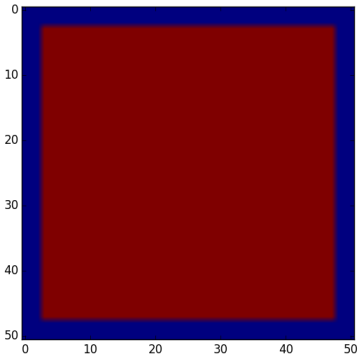

(a) Penning Trap, 1%

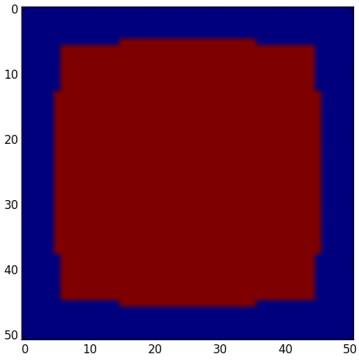

(b) Penning Trap, 0.1%

Figure A.11: Maps for generated fields showing regions (in red) where the fields are within some percentage of the target field. Each map is taken at the z=0 plane.

past the quadratic term represent imperfections in the field and create spreads in the frequency of particle oscillations.

The most important factor in trap performance is the octupole term, C_4, with other terms contributing less at higher orders. The field generated using the halftone design showed very good performance in this regard. The first two terms were $C_4 = 4.0 \times 10^{-3}$ and $C_6 = 6.7 \times 10^{-2}$. These values are in line with or better than those typically found in traps using hyperbolic electrodes, though are generally bettered by traps which incorporate compensation electrodes. A full discussion of imperfections in Penning traps and their effect on ion measurements is beyond the scope of this paper, and the reader is directed to other sources like [89] or [90]. Once again, it is possible that the presence of higher order terms inherent in the halftone design can create effects that have not been explored in the literature, so a full simulation would be necessary for rigorous examination of the performance of such a trap.

A.5.3 Overlaying Multiple Trap Designs

One possible application for the halftone method is to create multiple electric potentials patterned onto the same PCB. These electrodes would have to be carefully designed such that switching the field pattern is done by altering the connections to each electrode. Figure A.12 shows one such example. We generated a single face of a Penning trap and Paul trap design, and by rotating the strips of one design relative to the other, we create a two dimensional array of electrodes that support either field depending on how the voltages are applied. Because of the added complexity of accurately modeling the potential between the electrodes in this sort of design, we have not yet modeled the full potential from a design like this one, but we have included this discussion to present one possible way that the halftone method can be

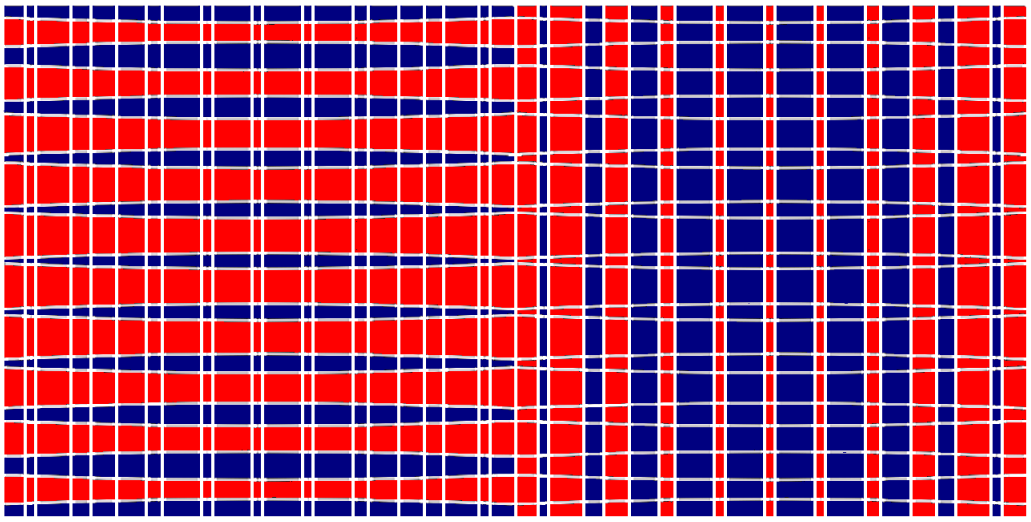

(a) Penning Trap (b) Paul Trap

Figure A.12: An example electrode design which supports generating two different fields.

used which is not currently possible with commonly used methods.

A.6 Conclusions

Here we have described some early results of what we have chosen to call the "halftone" method of electric field design. We believe this method can be used to great effect in low cost or rapid prototyping applications. The calculations presented here indicate that the method can produce results on par with the state of the art, so long as problems stemming from breakdown tolerance can be dealt with. This continues to be an evolving area of study that should show improvement in the future.

The authors acknowledge the use of the KEM-Field, an electric and magnetic field solver developed by the KATRIN collaboration.

Bibliography

[1] K. A. Olive and P. D. Group, *Review of Particle Physics*, *Chinese Physics C* **38** (Aug., 2014) 090001.

[2] J. L. Hewett *et al.*, *Fundamental Physics at the Intensity Frontier*, *arXiv:1205.2671 [hep-ex, physics:hep-ph]* (May, 2012). arXiv: 1205.2671.

[3] Y. G. A. Gando, *White paper: CeLAND - Investigation of the reactor antineutrino anomaly with an intense 144ce-144pr antineutrino source in KamLAND*, .

[4] J. A. F. J. Barrett, *Resolving the Reactor Neutrino Anomaly with the KATRIN Neutrino Experiment*, *1105.1326* (May, 2011).

[5] S. M. Bilenky and C. Giunti, *Neutrinoless double-beta decay. A brief review*, *Modern Physics Letters A* **27** (Apr., 2012) 1230015. arXiv: 1203.5250.

[6] J. Angrik *et al.*, *KATRIN design report 2004*, *Wissenschaftliche Berichte FZKA* **7090** (2005).

[7] B. Monreal and J. A. Formaggio, *Relativistic Cyclotron Radiation Detection of Tritium Decay Electrons as a New Technique for Measuring the Neutrino Mass*, *Phys.Rev.* **D80** (2009) 051301.

[8] A. C. Thompson and D. Vaughan, *X-ray Data Booklet*. Lawrence Berkeley Laboratory, 2001.

[9] R. Davis, D. S. Harmer, and K. C. Hoffman, *Search for Neutrinos from the Sun*, *Physical Review Letters* **20** (May, 1968) 1205–1209.

[10] Q. R. Ahmad *et al.*, *Direct Evidence for Neutrino Flavor Transformation from Neutral-Current Interactions in the Sudbury Neutrino Observatory*, *Physical Review Letters* **89** (June, 2002) 011301.

[11] **SNO** Collaboration, S. N. Ahmed *et al.*, *Measurement of the Total Active ^8B Solar Neutrino Flux at the Sudbury Neutrino Observatory with Enhanced Neutral Current Sensitivity*, *Physical Review Letters* **92** (May, 2004) 181301.

[12] **KamLAND** Collaboration, T. Araki *et al.*, *Measurement of Neutrino Oscillation with KamLAND*, *Physical Review Letters* **94** (Mar., 2005) 081801.

[13] **Super-Kamiokande** Collaboration, Y. Ashie *et al.*, *Measurement of atmospheric neutrino oscillation parameters by Super-Kamiokande I*, *Physical Review D* **71** (June, 2005) 112005.

[14] **Super-Kamiokande** Collaboration, Y. Ashie *et al.*, *Evidence for an Oscillatory Signature in Atmospheric Neutrino Oscillations*, *Physical Review Letters* **93** (Sept., 2004) 101801.

[15] **K2K** Collaboration, M. H. Ahn, *Measurement of Neutrino Oscillation by the K2k Experiment*, *Physical Review D* **74** (Oct., 2006). arXiv: hep-ex/0606032.

[16] **T2K** Collaboration, K. Abe *et al.*, *First muon-neutrino disappearance study with an off-axis beam*, *Physical Review D* **85** (Feb., 2012) 031103.

[17] **MINOS** Collaboration, P. Adamson *et al.*, *Measurement of Neutrino and Antineutrino Oscillations Using Beam and Atmospheric Data in MINOS*, *Physical Review Letters* **110** (June, 2013) 251801.

[18] **Double Chooz** Collaboration, Y. Abe *et al.*, *Indication of Reactor $\overline{\nu}_e$ Disappearance in the Double Chooz Experiment*, *Physical Review Letters* **108** (Mar., 2012) 131801.

[19] F. P. An *et al.*, *Observation of Electron-Antineutrino Disappearance at Daya Bay*, *Physical Review Letters* **108** (Apr., 2012) 171803.

[20] **RENO** Collaboration, J. K. Ahn *et al.*, *Observation of Reactor Electron Antineutrinos Disappearance in the RENO Experiment*, *Physical Review Letters* **108** (May, 2012) 191802.

[21] A. Aguilar *et al.*, *Evidence for Neutrino Oscillations from the Observation of Electron Anti-neutrinos in a Muon Anti-Neutrino Beam*, *Physical Review D* **64** (Nov., 2001). arXiv: hep-ex/0104049.

[22] **MiniBooNE** Collaboration, A. A. Aguilar-Arevalo *et al.*, *Improved Search for $\overline{\nu}_\mu \to \overline{\nu}_e$ Oscillations in the MiniBooNE Experiment*, *arXiv:1303.2588 [hep-ex, physics:hep-ph, physics:nucl-ex, physics:nucl-th]* (Mar., 2013). arXiv: 1303.2588.

[23] T. A. Mueller *et al.*, *Improved Predictions of Reactor Antineutrino Spectra*, *Physical Review C* **83** (May, 2011). arXiv: 1101.2663.

[24] O. Yasuda, *Search for sterile neutrinos at reactors*, *arXiv:1107.4766* (July, 2011).

[25] G. Mention *et al.*, *The Reactor Antineutrino Anomaly*, *Physical Review D* **83** (Apr., 2011). arXiv: 1101.2755.

[26] F. Kaether, W. Hampel, G. Heusser, J. Kiko, and T. Kirsten, *Reanalysis of the GALLEX solar neutrino flux and source experiments*, *Physics Letters B* **685** (Feb., 2010) 47–54. arXiv: 1001.2731.

[27] J. N. Abdurashitov *et al.*, *Measurement of the response of a Ga solar neutrino experiment to neutrinos from an 37ar source*, *Physical Review C* **73** (Apr., 2006). arXiv: nucl-ex/0512041.

[28] **SAGE** Collaboration, J. N. Abdurashitov *et al.*, *Measurement of the solar neutrino capture rate with gallium metal. III: Results for the 2002–2007 data-taking period*, *Physical Review C* **80** (July, 2009). arXiv: 0901.2200.

[29] C. Giunti, *Sterile Neutrino Fits*, *arXiv:1106.4479* (June, 2011).

[30] C. Giunti, *Sterile Neutrino Status*, *arXiv:1311.1335 [astro-ph, physics:hep-ex, physics:hep-ph]* (Nov., 2013). arXiv: 1311.1335.

[31] C. Giunti and M. Laveder, *Towards 3+1 Neutrino Mixing*, *arXiv:1109.4033* (Sept., 2011).

[32] J. Kopp, M. Maltoni, and T. Schwetz, *Are there sterile neutrinos at the eV scale?*, *1103.4570* (Mar., 2011).

[33] E. Bulbul *et al.*, *Detection of An Unidentified Emission Line in the Stacked X-ray spectrum of Galaxy Clusters*, *arXiv:1402.2301 [astro-ph]* (Feb., 2014). arXiv: 1402.2301.

[34] K. N. Abazajian, *Resonantly-Produced 7 keV Sterile Neutrino Dark Matter Models and the Properties of Milky Way Satellites*, *Physical Review Letters* **112** (Apr., 2014). arXiv: 1403.0954.

[35] A. Merle and A. Schneider, *Production of Sterile Neutrino Dark Matter and the 3.5 keV line*, *arXiv:1409.6311 [astro-ph, physics:hep-ph]* (Sept., 2014). arXiv: 1409.6311.

[36] S. Mertens *et al.*, *Sensitivity of Next-Generation Tritium Beta-Decay Experiments for keV-Scale Sterile Neutrinos*, *Journal of Cosmology and Astroparticle Physics* **2015** (Feb., 2015) 020–020. arXiv: 1409.0920.

[37] S. Mertens *et al.*, *Wavelet Approach to Search for Sterile Neutrinos in Tritium β-Decay Spectra*, *Physical Review D* **91** (Feb., 2015). arXiv: 1410.7684.

[38] H. Klapdor-Kleingrothaus, I. Krivosheina, A. Dietz, and O. Chkvorets, *Search for neutrinoless double beta decay with enriched 76ge in Gran Sasso 1990–2003*, *Physics Letters B* **586** (Apr., 2004) 198–212.

[39] **GERDA** Collaboration, C. Macolino, *Results on neutrinoless double beta decay from GERDA Phase I*, *Modern Physics Letters A* **29** (Jan., 2014) 1430001. arXiv: 1312.0562.

[40] **Planck** Collaboration, R. Adam *et al.*, *Planck 2015 results. I. Overview of products and scientific results*, *arXiv:1502.01582 [astro-ph]* (Feb., 2015). arXiv: 1502.01582.

[41] **Planck** Collaboration, P. A. R. Ade *et al.*, *Planck 2015 results. XIII. Cosmological parameters*, *arXiv:1502.01589 [astro-ph]* (Feb., 2015). arXiv: 1502.01589.

[42] G. Mangano *et al.*, *Relic neutrino decoupling including flavour oscillations*, *Nuclear Physics B* **729** (Nov., 2005) 221–234. arXiv: hep-ph/0506164.

[43] K. N. Abazajian *et al.*, *Neutrino Physics from the Cosmic Microwave Background and Large Scale Structure*, *Astroparticle Physics* **63** (Mar., 2015) 66–80. arXiv: 1309.5383.

[44] W. D. Arnett, J. N. Bahcall, R. P. Kirshner, and S. E. Woosley, *Supernova 1987a*, *Annual Review of Astronomy and Astrophysics* **27** (1989), no. 1 629–700.

[45] M. Daum *et al.*, *Precision Measurement of the Muon Momentum in Pion Decay at Rest*, *Phys.Rev.* **D20** (1979) 2692.

[46] A. Pich, *Tau physics*, *Int.J.Mod.Phys.* **A15S1** (2000) 157–173.

[47] G. Drexlin, V. Hannen, S. Mertens, and C. Weinheimer, *Current Direct Neutrino Mass Experiments*, *Advances in High Energy Physics* **2013** (Feb., 2013) e293986.

[48] C. Kraus *et al.*, *Final Results from phase II of the Mainz Neutrino Mass Search in Tritium β Decay*, *The European Physical Journal C* **40** (Apr., 2005) 447–468. arXiv: hep-ex/0412056.

[49] V. N. Aseev *et al.*, *An upper limit on electron antineutrino mass from Troitsk experiment*, *1108.5034* (Aug., 2011).

[50] P. J. Doe *et al.*, *Project 8: Determining neutrino mass from tritium beta decay using a frequency-based method*, .

[51] D. M. Asner *et al.*, *Single electron detection and spectroscopy via relativistic cyclotron radiation*, *Physical Review Letters* **114** (Apr., 2015). arXiv: 1408.5362.

[52] M. Babutzka *et al.*, *Monitoring of the operating parameters of the KATRIN Windowless Gaseous Tritium Source*, *New Journal of Physics* **14** (Oct., 2012) 103046.

[53] M. Röllig *et al.*, *Activity monitoring of a gaseous tritium source by beta induced X-ray spectrometry*, *Fusion Engineering and Design* **88** (Oct., 2013) 1263–1266.

[54] T. M. James *et al.*, *Accurate depolarization ratio measurements for all diatomic hydrogen isotopologues*, *Journal of Raman Spectroscopy* **44** (June, 2013) 857–865.

[55] M. Schlösser *et al.*, *In-Line Calibration of Raman Systems for Analysis of Gas Mixtures of Hydrogen Isotopologues with Sub-Percent Accuracy*, *Analytical Chemistry* **85** (Mar., 2013) 2739–2745.

[56] M. Schlösser *et al.*, *Accurate calibration of the laser Raman system for the Karlsruhe Tritium Neutrino Experiment*, *Journal of Molecular Structure* **1044** (July, 2013) 61–66.

[57] M. Schlösser *et al.*, *Evaluation method for Raman depolarization measurements including geometrical effects and polarization aberrations*, *Journal of Raman Spectroscopy* **44** (Mar., 2013) 453–462.

[58] J. J. Wortman, D. P. Griffis, S. R. Bryan, and W. Kinard, *Capacitor-type micrometeoroid detectors*, pp. 94–96, 1986.

[59] P. C. Kassel, *Characteristics of capacitor-type micrometeoroid flux detectors when impacted with simulated micrometeoroids*, .

[60] W. H. Kinard *et al.*, *micrometeoriod*, Oct., 1990. U.S. Classification 73/170.25 International Classification B64G1/22, G01N1/04 Cooperative Classification G01N1/04, B64G1/22 European Classification B64G1/22, G01N1/04.

[61] M. Vicanek, *Electron transport processes in reflection electron energy loss spectroscopy (REELS) and X-ray photoelectron spectroscopy (XPS)*, *Surface Science* **440** (Oct., 1999) 1–40.

[62] C. M. Kwei, P. Su, Y. F. Chen, and C. J. Tung, *Monte Carlo calculations of the reflection electron energy loss spectra in gold*, *Journal of Physics D: Applied Physics* **30** (Jan., 1997) 13.

[63] F. Salvat-Pujol and W. S. M. Werner, *Oswald-Kasper-Gaukler model for reflection electron energy loss spectroscopy*, *Physical Review B* **83** (May, 2011) 195416.

[64] R. A. Baragiola, C. A. Dukes, and P. Riccardi, *Plasmon excitation in ion–solid interactions*, *Nuclear Instruments and Methods in Physics Research Section B: Beam Interactions with Materials and Atoms* **182** (Aug., 2001) 73–83.

[65] H. Yoshikawa, T. Tsukamoto, R. Shimizu, and V. Crist, *Monte Carlo analysis of XPS and REELS spectra obtained at different take-off angles*, *Surface and Interface Analysis* **18** (Nov., 1992) 757–764.

[66] G. Gergely, *Elastic backscattering of electrons: determination of physical parameters of electron transport processes by elastic peak electron spectroscopy*, *Progress in Surface Science* **71** (Sept., 2002) 31–88.

[67] Z. J. Ding, H. M. Li, K. Goto, Y. Z. Jiang, and R. Shimizu, *Energy spectra of backscattered electrons in Auger electron spectroscopy: comparison of Monte Carlo simulations with experiment*, *Journal of Applied Physics* **96** (Oct., 2004) 4598–4606.

[68] T. E. Gallon, *The estimation of backscattering effects in electron-induced Auger spectra*, *Journal of Physics D: Applied Physics* **5** (Apr., 1972) 822.

[69] E. H. Darlington, *Backscattering of 10-100 keV electrons from thick targets*, *Journal of Physics D: Applied Physics* **8** (Jan., 1975) 85.

[70] E. H. S. Burhop, *The Auger Effect and Other Radiationless Transitions*. Cambridge University Press, June, 2014.

[71] Y. Kumar and M. Kumar, *Inner-shell ionization cross section of Gold by electron and positron impact*, *Journal of Atomic and Molecular Sciences* **5** (Nov., 2014) 352–360.

[72] D. Bote, F. Salvat-Pujol, J. Escuder, C. Powell, and F. Salvat, *Cross Sections for the Ionization of Atoms by Electron Impact. A Numerical Database and an Analytical Formula*, *Microscopy and Microanalysis* **14** (Aug., 2008) 948–949.

[73] U. Werner and W. Jitschin, *L-vacancy decay in heavy elements ($72 \leq z \leq 82$) by the synchrotron photoionization method*, *Physical Review A* **38** (Oct., 1988) 4009–4018.

[74] N. T. A. Spalek, "Golden rear wall backscattering basics." June, 2008.

[75] X. Shi and G. M. Fuller, *A New Dark Matter Candidate: Non-thermal Sterile Neutrinos*, *Physical Review Letters* **82** (Apr., 1999) 2832–2835. arXiv: astro-ph/9810076.

[76] I. Daubechies, *The wavelet transform, time-frequency localization and signal analysis*, *IEEE Transactions on Information Theory* **36** (Sept., 1990) 961–1005.

[77] R. E. March, *An introduction to quadrupole ion trap mass spectrometry*, *Journal of mass spectrometry* **32** (1997), no. 4 351–369.

[78] D. J. Douglas, A. J. Frank, and D. Mao, *Linear ion traps in mass spectrometry*, *Mass Spectrometry Reviews* **24** (Jan., 2005) 1–29.

[79] R. E. March, *Quadrupole ion traps*, *Mass Spectrometry Reviews* **28** (Nov., 2009) 961–989.

[80] S. T. John Raymond Gibson, *Asymmetrical features of mass spectral peaks produced by quadrupole mass filters.*, *Rapid communications in mass spectrometry : RCM* **17** (2003), no. 10 1051–5.

[81] S. T. John Raymond Gibson, *Prediction of quadrupole mass filter performance for hyperbolic and circular cross section electrodes*, *Rapid Communications in Mass Spectrometry* **14** (2000), no. 18 1669 – 1673.

[82] J. C. Schwartz, M. W. Senko, and J. E. P. Syka, *A two-dimensional quadrupole ion trap mass spectrometer*, *Journal of the American Society for Mass Spectrometry* **13** (June, 2002) 659–669.

[83] J. D. Jackson, *Classical Electrodynamics*. John Wiley and Sons, Inc., 1999.

[84] J. R. Gibson and S. Taylor, *Numerical investigation of the effect of electrode size on the behaviour of quadrupole mass filters*, *Rapid Communications in Mass Spectrometry* **15** (Oct., 2001) 1960–1964.

[85] A. H. Azbaid, A. D. Dymnikov, and G. Martinez, *Influence of the rod diameter of electrostatic quadrupole lenses on the axial field and on the minimum spot size in nonlinear microprobes*, vol. 3155, pp. 205–213, 1997.

[86] R. Syms, T. Tate, M. Ahmad, and S. Taylor, *Design of a microengineered electrostatic quadrupole lens*, *IEEE Transactions on Electron Devices* **45** (Nov., 1998) 2304–2311.

[87] G. Gabrielse, L. Haarsma, and S. L. Rolston, *Open-endcap Penning traps for high precision experiments*, *International Journal of Mass Spectrometry and Ion Processes* **88** (Apr., 1989) 319–332.

[88] G. Bollen, R. B. Moore, G. Savard, and H. Stolzenberg, *The accuracy of heavy ion mass measurements using time of flight ion cyclotron resonance in a Penning trap*, *Journal of Applied Physics* **68** (Nov., 1990) 4355–4374.

[89] G. Gabrielse, *Why Is Sideband Mass Spectrometry Possible with Ions in a Penning Trap?*, *Physical review letters* **102** (2009), no. 17 172501.

[90] G. G. Lowell S. Brown, *Geonium theory: Physics of a single electron or ion in a Penning trap*, *Reviews of Modern Physics - REV MOD PHYS* **58** (1986), no. 1 233–311.